MATHEMATICAL MODELS AND NUMERICAL METHODS FOR HUMAN TEAR FILM DYNAMICS

by

Longfei Li

A dissertation submitted to the Faculty of the University of Delaware in partial fulfillment of the requirements for the degree of Doctor of Philosophy in Applied Mathematics

Summer 2014

ProQuest LLC.
789 East Eisenhower Parkway
P.O. Box 1346
Ann Arbor, MI 48106 - 1346

MATHEMATICAL MODELS AND NUMERICAL METHODS FOR HUMAN TEAR FILM DYNAMICS

by

Longfei Li

Approved: _____

John Pelesko, Ph.D.
Chair of the Department of Mathematical Sciences

Approved: _____

George H. Watson, Ph.D.
Dean of the College of Arts and Sciences

Approved: _____

James G. Richards, Ph.D.
Vice Provost for Graduate and Professional Education

I certify that I have read this dissertation and that in my opinion it meets the academic and professional standard required by the University as a dissertation for the degree of Doctor of Philosophy.

Signed: _____

Richard J. Braun, Ph.D.
Professor in charge of dissertation

I certify that I have read this dissertation and that in my opinion it meets the academic and professional standard required by the University as a dissertation for the degree of Doctor of Philosophy.

Signed: _____

Tobin A. Driscoll, Ph.D.
Member of dissertation committee

I certify that I have read this dissertation and that in my opinion it meets the academic and professional standard required by the University as a dissertation for the degree of Doctor of Philosophy.

Signed: _____

L. Pamela Cook, Ph.D.
Member of dissertation committee

I certify that I have read this dissertation and that in my opinion it meets the academic and professional standard required by the University as a dissertation for the degree of Doctor of Philosophy.

Signed: _____

Vladimir Ajaev, Ph.D.
Member of dissertation committee

ACKNOWLEDGEMENTS

I would like to thank my family, especially my wife Xiaohan and my mother Sumei, for their endless support and belief in me. I would like to thank the Department of Mathematical Sciences at University of Delaware for providing me such a great environment to learn and do research. In addition, I would like to specially thank Ms Deborah See for her assistance during the past five years.

I am heartily grateful to my friend Brooks Emerick. I appreciate his countless help all these years. I miss those days that we stayed up late in our office to discuss homework problems and walk to Dunkin Donuts in the middle of night; it was a really fun and fruitful period of time. One of the best thing for me at UD is that Brooks and I share the same office from our day one at Math Department to the day we both become doctors. So I also want to thank whoever assigned this wonderful officemate to me.

I want to thank Dr. Driscoll, Dr. Cook, and Dr Ajaev for reviewing on my dissertation. Most of all, I would like to express my sincerest acknowledgment to my advisor Dr. Richard Braun. I wouldn't have been able to complete this dissertation without his guidance and encouragement. Dr. Braun is the best teacher I have ever met. His knowledge and wisdom will forever guide me in my life.

Finally, I want to thank the National Science Foundation (NSF). This dissertation is based on work supported by the NSF under the Grant No. DMS-1022706. I also gratefully acknowledge the support and hospitality provided by the IMA during my visit which took place from February to March, 2014.

TABLE OF CONTENTS

LIST OF TABLES viii
LIST OF FIGURES ix
ABSTRACT xiii

Chapter

1 INTRODUCTION 1

2 A MODEL FOR THE HUMAN TEAR FILM WITH HEATING FROM WITHIN THE EYE 7

2.1 Introduction 7
2.2 Formulation 10
2.3 Numerical Methods 15

2.3.1 RODE Method 16
2.3.2 DAE/fd Method 16
2.3.3 DAE/sp Method 17

2.4 Test Problem 17

2.4.1 Problem Setup 17
2.4.2 Test Problem Results 18

2.5 Tear Film Results 21
2.6 Conclusion 31

3 MODELING TEAR FILM AND OSMOLARITY DYNAMICS ON AN EYE SHAPED DOMAIN 33

3.1 Introduction 33
3.2 Formulation 35

3.2.1 Model Derivation 36

3.2.2 Permeability of the ocular surface . . . 44
3.2.3 Boundary conditions . . . 44
3.2.4 Initial Condition . . . 46

3.3 Conclusion . . . 49

4 TEAR FILM DYNAMICS WITH EVAPORATION, WETTING AND TIME-DEPENDENT FLUX BOUNDARY CONDITION ON AN EYE-SHAPED DOMAIN . . . 50

4.1 Introduction . . . 50
4.2 Experiment . . . 50
4.3 Numerical Methods . . . 52
4.4 Results . . . 54

4.4.1 Tear Film Dynamics . . . 54
4.4.2 Volume Conservation . . . 62
4.4.3 Recovering the Thinning Rate . . . 63
4.4.4 Compensation of Evaporation Loss . . . 64
4.4.5 Comparison with Experiment . . . 67

4.4.5.1 Evaporation . . . 67
4.4.5.2 Hydraulic Connectivity . . . 67

4.5 Conclusion . . . 69

5 COMPUTED TEAR FILM AND OSMOLARITY DYNAMICS ON AN EYE-SHAPED DOMAIN . . . 71

5.1 Introduction . . . 71
5.2 Numerical Methods . . . 72

5.2.1 Computational Grid . . . 72
5.2.2 A Hybrid Time-Stepping Scheme . . . 73

5.3 Results . . . 74

5.3.1 Constant Nonzero Permeability . . . 74
5.3.2 Zero Permeability . . . 77
5.3.3 Variable Permeability . . . 80

5.3.3.1 Diffusion . . . 82

5.3.3.2 Movement of Fluid and Solutes 83

5.3.4 Increased Evaporation Rate 86
5.3.5 Osmotic Flux 88
5.3.6 Neumann Boundary Condition for the Osmolarity 90

5.4 Conclusion 91

6 NUMERICAL METHODS FOR COMPUTING TEAR FILM AND OSMOLARITY DYNAMICS ON AN EYE-SHAPED DOMAIN 94

6.1 Introduction 94
6.2 Composite Overlapping Grid 95

6.2.1 Discretization on Composite Overlapping Grids 96

6.3 BDF Method 97
6.4 RKC Method 99

6.4.1 RKC Formulas 100
6.4.2 Implementation of RKC Method 102

6.4.2.1 Local Error Estimation 102
6.4.2.2 Time Step Prediction 103
6.4.2.3 Number of RKC Stages 103

6.5 A Hybrid Time-Stepping Method 104
6.6 Test Problems 105
6.7 Conclusion 106

7 CONCLUSION 109

7.1 Future Work 111

BIBLIOGRAPHY 112

Appendix

A PARAMETERS 122
B COPYRIGHT PERMISSIONS 125

LIST OF TABLES

3.1 Parameters appearing in the flux boundary condition. 47

4.1 No flux boundary condition and no evaporation. 63

5.1 Extreme values for various cases. $P_c(x, y)$ denotes the variable permeability case and is given by Equation (3.40). 78

5.2 Conservation of mass with boundary conditions (5.3) & (3.49) . . . 91

6.1 Errors of the test problem on the circular domain at $t = 2$. 106

A.1 Dimensionless Parameters. Values and descriptions of the dimensional parameters appeared are given in Table A.2. 123

A.2 Dimensional Parameters. 124

LIST OF FIGURES

2.1 Coordinate system for tear film model with heat transfer from the cornea (and aqueous humor). 10

2.2 Plot of the exact solution $H(x,t)$ in (2.29) with $h_0 = 25$, $t_0 = 2$, $y_c = -4$ and $m = 4$. 18

2.3 Convergence of three methods 19

2.4 Absolute Error at $t = 7$. Left axis shows the scale for RODE and DAE/fd. Right axis scales the error of DAE/sp. 20

2.5 Maximum Absolute Error vs Time. Left scales RODE and DAE/fd. Right axis scales DAE/sp. 20

2.6 Temperature of the free surface at $x = 0$ for various cases with Bi$= 0.01, G = 0$, $y_c = -4$ and $\tilde{y}_c = -5$. Initially, temperature inside the rectangle is set to be body temperature. 22

2.7 Temperature Profile for $T_c(x, \tilde{y}, 0) = 1$,Bi$= 0$,$G = 0$. 23

2.8 Tear film thickness $h(x,t)$ and evaporative mass flux $J(x,t)$ at several times with Bi$= G = 0$. 24

2.9 $\min(h)$ and $\min(J)$ as a function of time for Bi$= G = 0$. 24

2.10 $h(x,t)$ and $J(x,t)$ for several values of Bi. 25

2.11 Results for the nonuniform temperature initial condition (2.24) with Bi$= 0.0009$ and $G = 0$. 26

2.12 Tear film thickness h and evaporative mass flux J. 27

2.13 $\min h$ and $\min J$. 28

2.14 $h(x,t)$ and $J(x,t)$ for several times with Bi$= 0.0009$ and $G = 0.05$. . 29

2.15 Comparison of Numerical simulation to experiment data. 30

2.16 GCC temperature evolution for various thinning rate assumptions. 31

3.1 The coordinate system and eye-shaped domain. The z' direction points out of the page. 36

3.2 Variable permeability distribution over the ocular surface. 44

3.3 Time sequences of fluid flux boundary condition during one flux cycle. 47

3.4 Smoothed initial conditions for h and p. 48

4.1 Sequence of tear film images of the experiment after a blink. The first image is 5.5s after a blink; the next three images are, respectively, 9.5s, 10.17s and 10.83s after that blink. The final image is after a blink that began less than a second after the sequence shown. Gravity is oriented downward in the panels. 51

4.2 Computational grid on the eye-shaped domain. 53

4.3 Contours of tear film thickness with $E = 0$ and $G = 0$. The maroon band around the boundary shows thickness greater than or equal to 3. 55

4.4 Pressure distribution for $E = G = 0$ with time-dependent flux boundary conditions and a wettable substrate. 56

4.5 Contour plots of the tear film thickness without gravity (left column) and with gravity (right column). The maroon band around the boundary shows thickness greater than or equal to 3. 57

4.6 Pressure distribution for $E \neq 0$ and $G = 0$. 58

4.7 The flux direction field plotted over the contours of the norm of the flux at $t = 4$ with $E \neq 0$ and $G = 0$. (Far fewer arrows than the computational grid points are shown for clarity. All the arrows in this plot start at different locations.) 59

4.8 The flux direction field at the end of first flux cycle. $E \neq 0$ and $G = 0$. (Far fewer arrows than the computational grids are shown for clarity. All the arrows in this plot start at different locations.) . . . 60

4.9 The flux direction field at the end of first flux cycle with $E \neq 0$ and $G = 0.05$. (Far fewer arrows than the computational grids are shown for clarity. All the arrows in this plot start at different locations.) . 61

4.10 Pressure distribution for $E \neq 0$ and $G \neq 0$. 62

4.11 Results for the time-dependent flux boundary condition. 64

4.12 Evaporation rate $\frac{d}{dt}e(t)$ of various cases. 65

4.13 Contours of tear film thickness with flux compensating the evaporation loss and $G = 0$. 66

4.14 Comparison with experiment. 68

5.1 Improved computational grid on the eye-shaped domain. 72

5.2 Contours of tear film thickness (left column) and osmolarity (right column) with constant permeability of $P_c = 0.013$ all over the exposed ocular surface and with Dirichlet boundary condition (3.48) on the osmolarity. The thinning rate is 4μm/min. 75

5.3 Cross-sectional plots through the vertical line $x = 0$ with $P_c = 0.013$ and Dirichlet boundary condition (3.48). The thinning rate is 4μm/min and the upper eyelid is located on the positive side of the y-axis. 77

5.4 Contours of tear film thickness (left) and osmolarity (right) with $P_c = 0$ and Dirichlet boundary condition (3.48). The thinning rate is 4μm/min. 79

5.5 Cross-sectional plots through the vertical line $x = 0$ with $P_c = 0$ and Dirichlet boundary condition (3.48). The thinning rate is 4μm/min and the upper eyelid is on the positive side of y-axis. 79

5.6 Contours of tear film thickness (left column) and osmolarity (right column) with variable permeability (3.40) and Dirichlet boundary condition (3.48). The thinning rate is 4μm/min. 81

5.7 Cross-sectional plots through the horizontal line $y = 0.3$ with variable permeability (3.40) and Dirichlet boundary condition (3.48). Thinning rate is 4μm/min and the temporal canthus is located at the positive side of x-axis. 82

5.8 The contribution of diffusion to osmolarity dynamics. Diffusion is larger (magnitude greater than 10^{-2}) in the lighter areas. 83

5.9 Fluid flux ($\mathbf{Q}$) over contours of its magnitude with variable permeability and thinning rate 4μm/min. (Far fewer arrows than the computational grid points are shown for clarity. All the arrows in this plot start at different locations.) 85

5.10 Contour for $c(x, y, t)h(x, y, t) - c(x, y, 0)h(x, y, 0)$ with variable permeability and thinning rate 4μm/min. 86

5.11 Contours of tear film thickness (left column) and osmolarity (right column) with variable permeability (3.40) and Dirichlet boundary condition (3.48). The thinning rate is 20μm/min. 86

5.12 Cross-sectional plots through the horizontal line $y = 0.3$ with variable permeability (3.40) and Dirichlet boundary condition (3.48). Thinning rate is 20μm/min and the temporal canthus locates at the positive side of x-axis. 87

5.13 Competition between evaporative loss and osmotic flux (volume/time) 88

6.1 Composite overlapping grids on a unit disk. 95

6.2 Stability regions of various RK methods (the regions enclosed by the curves). 100

6.3 Test problem on the eye-shaped domain 107

ABSTRACT

The human tear film is a multilayer thin film that spreads on the ocular surface. It is essential for clear vision and eye health. This thesis studies dynamics of the human tear film using methods of mathematical modeling and scientific computing. The underlying goal of this work is to theoretically explain phenomena that are observed *in vivo*, to provide predictions that are yet to be verified by any experiments, and to develop computational approaches to solve the model equations. In this thesis, we formulate three mathematical models that emphasize various physical aspects of tear film dynamics, as well as the associated thermal and osmolarity (the concentration of ions in the tear film) dynamics. We also conduct preliminary numerical study of a hybrid time stepping scheme that is used for solving a coupled system of tear film and osmolarity.

In Chapter 2, we present a model for tear film dynamics and cooling during the interblink period that includes heat transfer from the interior of the eye. The tear film in this model is on a one dimensional domain that is oriented vertically through the center of the cornea, with stationary ends corresponding to the eyelid margins. Lubrication theory is used to derive an equation for the thickness of the film; the nonlinear partial differential equation for the thickness is solved subject to either a fixed temperature at the substrate or with heat diffusion from within two different model rectangular domains. The model domains are simplified geometries that represent the anterior eye and that may include the cornea and some aqueous humor; one model domain is asymptotically thin (thin substrate) and the other has finite thickness (thick substrate). The thick substrate case captures temperature decreases that are observed *in vivo*, while the thin substrate and fixed temperature models do not. Parameters to reproduce observed temperature decreases are found.

We then focus on studying the dynamics of tear film on a 2D eye-shaped domain. In Chapter 3, we derive a mathematical model that couples osmolarity (treated as a single solute) and fluid dynamics within the tear film on a 2D eye-shaped domain. The model includes the physical effects of evaporation, surface tension, viscosity, ocular surface wettability, osmolarity, osmosis and tear fluid supply and drainage. The mathematical model has a time-dependent flux boundary condition that models the cycles of tear fluid supply and drainage; it mimics blinks on a stationary eye-shaped domain. We present the computed results of our model in the two subsequent chapters.

In Chapter 4, we focus on the tear film dynamics part of our model. The results from the numerical simulations are compared with experiments. This model captures the flow around the meniscus and other dynamic features of human tear film observed *in vivo*. Osmolarity is a key variable in understanding dry eye symptoms and disease. Therefore, we study the interaction between tear film motion and osmolarity dynamics in Chapter 5. The results of the numerical simulations show good agreement with existing 1D models for both tear film and osmolarity dynamics and provide new insight about the osmolarity distribution over the ocular surface during the interblink.

Our numerical results are obtained by solving the nonlinear model PDEs using the Overture computational framework. In Chapter 6, we discuss the numerical methods that are used to solve the 2D models. We also report preliminary numerical studies for the hybrid time-stepping scheme that we choose specifically for the weakly coupled system of the tear film and osmolarity dynamics. We construct test problems with known exact solutions from simplification of the osmolarity equation to study the numerical properties of this method. The test problem is solved on a circular domain with several mesh refinements to study the error convergence, and is also solved on the eye-shaped domain that is used for the model simulation.

Chapter 1

INTRODUCTION

The human eye is an exquisitely sensitive system, but many aspects of the mechanisms of the eye remain a mystery. For example, the structure and function of the tear film, a very thin layer of liquid film that is spread on the ocular surface by blink, are far from being understood [47]. The tear film is essential for clear vision and eye health. It helps to protect the ocular surface with moisture, to transport waste away, and to provide a smooth optical surface [45]. A properly functioning tear film maintains a critical balance between tear secretion and loss within each blink cycle.

Malfunction or deficiency of the tear film causes a collection of problems that are believed to comprise dry eye syndrome (DES) [62]. DES symptoms include, but are not limited to, blurred vision, burning, foreign body sensation, tearing and inflammation of the ocular surface. Studies up to 2007 estimate that there are 4.91 million Americans suffering from DES [7]. The ocular surface community is interested in understanding the function of the tear film [47] as well as the interaction of tear film dynamics and the connection between tear film volume, evaporation and break up with DES [7].

Commonly, the tear film is described as a thin liquid film with multiple layers. At the anterior interface with air is an oily lipid layer that decreases the surface tension and retards evaporation, both of which help retain a smooth well-functioning tear film [93]. The aqueous layer is posterior to the lipid layer and consists mostly of water [46]. At the ocular surface, there is a region with transmembrane mucins protruding from the cells in the corneal or conjunctival epithelia. This forest of glycosolated mucins, called the glycocalyx, has been referred to as the mucus layer in the past. It is generally agreed that the presence of the hydrophilic glycocalyx on the healthy ocular surface prevents the tear film from dewetting [18, 36, 38]. The overall thickness of the tear

film is a few microns [53], while the average thickness of the lipid layer is on the order of 50 to 100nm [93, 55] and the thickness of the glycocalyx is a few tenths of a micron [38]. This structure is rapidly reformed, on the order of one second, after each blink in a properly-functioning tear film.

The tear film is redistributed near the eyelid margins by surface tension. The curvature generated by the meniscus creates a low pressure which draws in fluid from surrounding areas, creating locally thin regions near the meniscus. When fluorescein is used to visualize tear film thickness, this locally thin region near the lids is dark, and has been called the "black line." The black line is typically thought to be a barrier between the meniscus at the lid margins and the rest of the tear film [82, 83]. Finally, though the healthy ocular surface is wettable, the tear film may still rupture; the term "break up" is used in the ocular science community for this phenomenon. The surface tension of the tear/air interface, the wettability of the ocular surface, and the osmolarity are among the effects that we include in this thesis.

The aqueous part of tear fluid is supplied from the lacrimal gland near the temporal canthus, and the excess is drained through the puncta near the nasal canthus. Mishima *et al.* [84] estimated the total tear volume and the rate of influx from the lacrimal gland, as well as the time for the entire volume of tear fluid to be replaced (tear turnover rate); Zhu and Chauhan [126] reviewed experiments on tear drainage and developed a mathematical model for drainage rates of the aqueous component through the puncta. Doane [28] proposed the mechanism of tear drainage *in vivo* whereby tear fluid is drained into the canaliculi through the puncta during the opening interblink phase. The drainage stops when the pressure equalizes in the canaliculi. Water lost from the tear film due to evaporation into air is an important process as well [86, 113, 52].

The supply and drainage of tear fluid affects the distribution and flow of the tear film. A number of methods have been used to visualize and/or measure tear film thickness and flow, including interferometry [29, 53, 54], optical coherence tomography [121] fluorescence imaging [41, 58] and many others. We mention only a small number

here that are relevant for our discussion of tear fluid flow over the exposed ocular surface in Chapters 3 and 4 of this thesis. Maurice [81] inserted lamp black particles (a.k.a., very fine soot) into the tear film and watched their trajectories with a slit lamp. He observed that the particle paths in the upper meniscus near the temporal canthus diverge, with some particles proceeding toward the nasal canthus via the upper meniscus and others going around the outer canthus before proceeding toward the nasal canthus via the lower meniscus. (To our knowledge, no images from this experiment exist.) We use the term "hydraulic connectivity" as shorthand for this splitting of flow connecting the menisci. A similar pattern of the tear film was observed by Harrison *et al.* [41] using fluorescein to visualize the tear film thickness. In this experiment, concentrated sodium fluorescein is instilled in the eye. Shining blue light on the eye causes the fluorescein to glow green; the fluorescence allows one to visualize the tear film [61]. The concentration in their experiments was such that, if evaporation occurs, the concentration of fluorescein increases and the intensity of the fluorescence decreases; if fresh tear fluid enters the tear film, the concentration decreases and fluorescent intensity increases [123, 91, 13]. Harrison *et al.* [41] visualized the entry of fresh tear fluid into the meniscus near the outer canthus, where the tear film was observed to brighten. Subsequently, this bright region split and fluid moved toward the nasal canthus along both the upper and lower lids via the menisci. The fluorescence could thus visualize hydraulic connectivity in the flow of tears. Similar experiments in King-Smith *et al.* [58] and Li *et al.* [67] visualized flow by using fluorescein instilled by drops in the tear film, and the mathematical model developed by Li *et al.* [67] exhibited hydraulic connectivity in a very similar way to the experimental results.

A variety of mathematical models have incorporated various important effects of tear film dynamics, as recently reviewed by Braun [11]. The most common assumptions for these models are a Newtonian tear fluid and a flat cornea [10, 16]. Tear film models are often formulated on a one-dimensional (1D) domain oriented vertically through the center of the cornea with stationary ends corresponding to the eyelid margins. We refer to models on this kind of domain as 1D models. Surface tension, viscosity, gravity and

evaporation are often incorporated into 1D models [125, 104, 83, 12]. Winter *et al.* [124] improved previous evaporation models by including a conjoining pressure from van der Waals forces that approximated the wettable corneal surface. Incorporating heat transfer from the underlying eye, Li and Braun [66] resolved a discrepancy of the tear film surface temperature between predictions of existing evaporation models and *in vivo* measurements. This study forms Chapter 2 of this thesis.

Recently, studies of 1D models that bring together the interblink period and a moving end that represents the upper lid have appeared. Jones *et al.* [49, 48] developed models for tear film formation and relaxation that were unified in this way; one end of the domain moved to model the upper lid motion during the opening phase of the blink, then remained stationary for the subsequent relaxation during the interblink. Braun and King-Smith [14] modeled eyelid motion for blink cycles by moving one end of the domain sinusoidally and they computed solutions for multiple complete blink cycles. Heryudono *et al.* [43] followed their study with a more realistic lid motion and specified a flux boundary condition; good agreement on tear film thickness between experiments and simulations was found [43]. Deng *et al.* [27, 26] extended the model of Li and Braun [66] to include upper lid motion (blink) and heat transfer from the underlying eye to explain observed ocular surface temperature measurements and to give new transient temperature results inside the eye. Bruna and Breward [20] studied a model that added a dynamic lipid layer to an underlying aqueous layer with an insoluble surfactant at the lipid/aqueous interface (representing polar lipids). They computed dynamic results for the model and found various useful limits for it.

In recent years, several authors have incorporated osmolarity dynamics into tear film models. Braun [11] gave a model for a spatially uniform film that was very similar to the one first suggested by King-Smith *et al.* [57]. The original model was a single ordinary differential equation for the tear film thickness that included evaporation from the tear/air interface at a constant rate and osmotic flow from the tear/cornea interface that was proportional to the osmolarity increase above the isotonic value. The latter assumption simplifies the tear/cornea interface to a semi-permeable boundary that

allows water but not solutes to pass. Braun [11] found that the model predicted equilibration of the tear film thickness at values greater than the height of the glycocalyx for sufficiently large permeability of the tear/cornea interface. Braun also found that the osmolarity could become quite large as the tear film thinned for small permeability values, as much as 10 times the isotonic value under some conditions. The model given in Braun [11] included van der Waals forces that stopped thinning at the purported height of the glycocalix which allowed the model to be used at zero permeability at the tear/cornea interface. Similar conclusions about the osmolarity during thinning were found there.

These models were extended to include a specified evaporation profile that varied in space by King-Smith and coworkers [59]. The evaporation profile was Gaussian with a peak value that could be specified larger than the surrounding constant rate. The local thinning caused by locally increased evaporation led to increased osmolarity in the break up region, which could be several times larger than the isotonic value. A modified evaporation distribution was created by Peng *et al.* [96] that had two parts. One part used an immobile lipid layer with specified thickness and fixed resistance to diffusion through it by water. The other part was a resistance to transport in the air outside the tear film; this second resistance included convective and diffusive transport in the air. They also found that the osmolarity was elevated in this model for tear film break up.

Zubkov *et al.* [127] developed a model describing the spatial distribution of tear film osmolarity that incorporates both fluid and solute (osmolarity) dynamics, evaporation, blinking and vertical saccadic eyelid motion. They found that both osmolarity was increased in the black line region and that measurements of the solute concentrations within the lower meniscus need not reflect those elsewhere in the tear film. This model gave results over a line oriented vertically through the center of the cornea, and thus gave information about the osmolarity over more of the ocular surface than the models mentioned above.

In Chapter 3, 4 and 5, we study dynamics of the fluid motion and osmolarity on

an eye-shaped domain. To our knowledge, Maki *et al.* [72, 73] were the first to extend models of fluid dynamics in the tear film to a geometry that approximated the exposed ocular surface. They formulated a relaxation model on a stationary 2D eye-shaped domain that was approximated from a digital photo of an eye. They specified tear film thickness and pressure boundary conditions [72] or flux boundary conditions [73]. Their simulations recovered features seen in 1D models such as formation of the black line, and captured some experimental observations of the tear film dynamics around the lid margins. Maki *et al.* [73] simplified the *in vivo* mechanisms and imposed a flux boundary condition having only spatial dependence (specifying the location of the lacrimal gland and the puncta holes) in the tear film relaxation model. Under some conditions, they were able to recover hydraulic connectivity as seen experimentally and described above. Li *et al.* [67] improved the model, by adding evaporation and a wettable ocular surface, as well as a time-dependent boundary condition that approximated the in- and out-flow of the aqueous layer of the tear film. This study forms Chapter 4 of this thesis.

The outline of this dissertation is as follows. In Chapter 2, we present a new tear film model that incorporates cooling from within the eye. After that, we shift our interests to tear film models on a 2D eye-shaped domain. We present the assumption and derivation of a tear film model that couples the osmolarity dynamics in Chapter 3. To our knowledge, this is the first such model that includes the osmolarity in a two-dimensional tear film model. In the following two chapters, we focus on the results predicted by the model. In Chapter 4, we present the tear fluid results and compare them with experimental data. In Chapter 5, we focus on osmolarity, and its interaction with fluid flow in the tear film. Detailed description of the numerical methods, together with a preliminary test problem that demonstrates the numerical accuracy, is given in Chapter 6. Finally, we conclude our study in Chapter 7.

Chapter 2

A MODEL FOR THE HUMAN TEAR FILM WITH HEATING FROM WITHIN THE EYE

2.1 Introduction

Models of tear film that fix the temperature of the substrate predict that the temperature of the tear film surface increases slightly after a blink [12, 124]; however, ocular surface temperature (OST) measurements show that cooling occurs, typically about 1 or 2 °C (discussed below). In this Chapter, we focus on the fluid dynamics of the tear film during the interblink and how it is affected by heat transfer beneath the tear film. We aim to determine a minimal amount of modeling of heat transfer from beneath the tear film that will recover the observed cooling of the surface of the tear film. We examine three different models for the heat distribution beneath the tear film and compare the results from the different models with each other and with experimental data. The heat transfer beneath the tear film is treated by either fixing the temperature at the corneal surface or by diffusion of heat into the cornea and aqueous humor. In all cases, convection inside the eye is neglected. The treatments of heat transfer used here are inspired by the models of Ajaev and Homsy [3, 2, 1, 106]. We find that incorporating heat transfer in a sufficiently thick region under the tear film causes the tear film surface to cool a comparable amount to that observed *in vivo*.

Measurement of the OST has been reviewed recently [98]; a brief description follows. Contact measurement techniques have a long history, but they have inherent sources of error [31, 101, 32]. Non-contact temperature measurement of OST using infrared thermometry was pioneered by Mapstone [75, 74, 76]; this approach appears to be the most successful method for determining the temperature of the anterior surface

of the tear film. This method has been used to measure anterior surface temperatures for both precorneal [30, 24, 50] and prelens [99] tear films.

Of particular interest are the results of Efron *et al.* [30] because of the quantitative reporting and interpretation of their results. They found that the average minimum temperature of the cornea, based on 21 subjects, was slightly inferior to the geometric center of the cornea (GCC). They speculated that this was because the lid margins heat the eye and the GCC is superior to the geometric center of the palpebral fissure. The temperature of the GCC after a blink was found to be 34.3 ± 0.7°C on average. The temperature contours were elliptical, and Efron *et al.* speculated that this was due to the shape of the lid margins. The horizontal temperature variation was fit well with a parabola. The temperature increased as the location moved toward the periphery of the cornea, and toward the lid margins; the temperature of the limbus was 0.45°C higher than at the GCC. An earlier study [4] found that this temperature difference was 0.6°C.

Efron *et al.* [30] also measured the rate of cooling of the ocular surface; they found a rate of 0.033 ± 0.024°C/s of the first 15s after a blink. They also found that if a subject had a slower rate of cooling and that if the OST stabilized then a subject was more likely to be able to refrain from blinking for an extended period. The data from their experiments suggested that the corneal temperature could vary by 0.78°C on average for each subject, and we will find that including this temperature variation is necessary for understanding ocular surface temperature variation for thin film modeling. Kamao *et al.* [50] found less cooling for controls and similar cooling for dry eyes.

Craig *et al.* [24] used ocular thermography, a variety of tear physiology tests and measurement of evaporation rates in both control and dry eye subjects in order to correlate physiological factors in dry eye with OST and evaporation from the tear film. They found that there was an increased rate of evaporation in dry eye, as found in a number of previous studies [100, 77, 79]. They found an average evaporation rate of 1.9×10^{-9}g/cm^2/s in controls (healthy eyes) and 4.1×10^{-8}g/cm^2/s in dry eyes; this

factor of 20 increase in evaporation rate is a relatively large factor over the controls, and smaller than typical measurements [78]. Dry eye subjects were found to have significantly lower GCC temperatures than the controls, and this could be attributed to increased evaporation. Also, the rate of cooling in the cornea was significantly higher in dry eyes, which may be caused by increased evaporation as well. Notably, Craig *et al.* [24] did not find any correlation between reduced non-invasive break up time (time to first rupture) and evaporation. Two studies have found that evaporation can be reduced in dry eye [34, 87], but these authors point out that their subjects are aqueous deficient dry eyes, and Craig *et al.* [24] speculate that this may be responsible for the reduced evaporation rate.

Scott [103, 102] developed finite element (FE) models of heat transfer in the eye that were intended to help decide whether radiative heating lead to cataracts in glass blowers. In the first paper, a detailed axisymmetric FE model of heat transfer within the eye and to the external environment beyond the anterior of the eye was studied. Scott found that the results were sensitive to the variability in three parameters: the evaporation rate from the anterior of the eye, the heat lost due to convection from the anterior of the eye, and the blood temperature in the eye. Scott [102] then incorporated radiative heating from the extreme environment of furnaces used in glass-blowing to the effects within the eye. Other finite element models of heat transfer in the eye have been developed [89, 90]; they computed steady state temperature distributions and found OST values within experimental ranges.

Steady-state finite element models with conductive and convective heat transfer in the aqueous humor have been developed in two [44, 94] and three [51] dimensions with similar conclusions. The coolest temperature on the anterior surface was located below the GCC, as in experiment [30] and the overall heat transfer through the anterior chamber is not significantly affected by the distorted temperature field. Approximate analytical models have been developed as well [21, 33]. Siggers and Ethier [105] review flow in the aqueous humor.

In this Chapter we study three domains for heat transfer beneath the tear film

during the interblink: no substrate, a thin substrate or a thick substrate. Our objective is to evaluate which case can capture the experimentally determined temperature drops on the ocular surface. The last two cases simplify the geometry of the eye to a rectangle, but this simplification seems to be sufficient to capture the desired dynamics. The models are developed in the next section. We then discuss numerical approaches and show results for test cases in Section 2.3. Tear film results are given in Section 2.5; discussion and conclusions follow.

2.2 Formulation

A sketch illustrating the model is shown in Figure 2.1; primes indicate dimensional variables. The acceleration due to gravity g is in the positive x' direction and

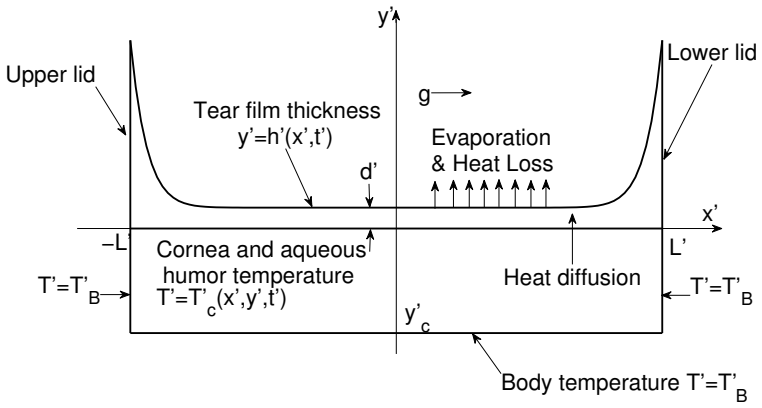

Figure 2.1: Coordinate system for tear film model with heat transfer from the cornea (and aqueous humor).

the velocity components of tear film are denoted by (u', v'). Only the dynamics of a post-blink tear film are studied here, so both ends of the film, representing the eyelid margins, are fixed at the positions corresponding to a fully open eye. The upper lid is fixed at $x' = -L'$ and lower lid is at $x' = L'$. Since the characteristic tear film thickness is much smaller than the radius of curvature of the cornea, there is no noticeable effect on the fluid motion due to the corneal curvature. Our model neglects

the curvature of the ocular surface, following many other studies; this assumption is justified in Braun *et al.* [16].

The tear film is located along the $y' = 0$ edge of a rectangle that models the cornea and aqueous humor. The rectangle occupies $-L' < x' < L'$ and $y'_c < y' < 0$, where y'_c is a location within the aqueous humor. The model is studied for the cases in which the rectangular substrate is either thick or thin, as well as the case with no substrate (fixed temperature) underneath the tear film [124]. We present the derivation for the thick substrate case here and simplify it to the other two cases.

The tear film is modeled as an incompressible Newtonian fluid with constant density ρ, dynamic viscosity μ, specific heat c_p and thermal conductivity k. In addition, energy conservation governs the temperature distribution in the tear film. In the rectangular region underneath the tear film, we consider only heat diffusion; the small effect of fluid motion on heat transport [44] justifies this assumption. Applying continuity of temperature and heat flux at the boundary between the tear film and the cornea connects these two domains. The other three edges of the rectangle are prescribed to be body temperature $T'_B = 37°\text{C}$.

We scale lengths with the half width of an open eye, $L' = 5 \times 10^{-3}\text{m}$, in the x' direction, and the characteristic tear film thickness $d' = 5 \times 10^{-6}\text{m}$ in the positive y' direction. A different length scale is applied in the negative y' direction, since the corneal thickness is $L'_c = 500 \times 10^{-6}\text{m}$ and a typical tear film thickness is 2.5–$5{\times}10^{-6}\text{m}$. The aqueous humor thickness is about 3 or $4 \times 10^{-3}\text{m}$. This suggests L'_c as the length scale in the negative y' direction for the thick substrate case, and $\tilde{y}$ denotes the dimensionless variable in the substrate to distinguish the scale difference. To nondimensionalize the model, the following dimensionless variables are introduced:

$$x' = L'x,\ h' = d'h,\ u' = U_0 u,\ v' = \frac{d'U_0}{L'}v,\ t' = \frac{L'}{U_0}t,$$

$$p' = \frac{\mu U_0}{L'\epsilon^2}p,\ T = \frac{T' - T'_s}{T'_B - T'_s},\ J' = \frac{k}{d'\mathcal{L}_m}(T'_B - T'_s)J,$$

$$y' = d'y \text{ (if } y' \geq 0),\ y' = L'_c\tilde{y} \text{ (if } y' < 0).$$

Here U_0 scales the velocity, T_s' is the saturation temperature and $\mathcal{L}_m$ represents the latent heat of vaporization per unit mass. The small parameter $\epsilon = d'/L' \ll 1$ arises indicating the separation of scales in the thin tear film. Applying lubrication theory gives the following leading order approximation. Unless otherwise noted, parameters appear in the formulations of all the models presented in the thesis are defined and given values in Appendix A. The nondimensional parameters are listed in Table A.1 with the dimensional parameters used in those expression given in Table A.2.

In the tear film, the flow on $0 \leq y \leq h(x,t)$ is governed by mass conservation:

$$\partial_x u + \partial_y v = 0, \tag{2.1}$$

and momentum conservation in each direction:

$$-\partial_x p + \partial_y^2 u + G = 0, \quad \text{and} \quad \partial_y p = 0. \tag{2.2}$$

The Stokes number G is the ratio of gravitational to viscous forces and is defined in Table A.1 as are all subsequent nondimensional parameters. Energy conservation is given by

$$\partial_y^2 T = 0. \tag{2.3}$$

At the free surface, $y = h(x,t)$, the mass balance and normal stress balance conditions hold:

$$EJ = v - u\partial_x h - \partial_t h, \tag{2.4}$$

and

$$p - p_v = -S\partial_x^2 h - A/h^3. \tag{2.5}$$

Here E represents the size of the evaporative contribution to the surface motion, S is the ratio of surface tension to viscous forces, p_v is the scaled vapor pressure, and A represents the nondimensional Hamaker constant in the standard van der Waals force

given nondimensionally by $\Pi = A/h^3$. In addition, the dimensionless energy balance is given by

$$J + \partial_y T + \mathrm{Bi}(T - T_\infty) = 0. \tag{2.6}$$

Bi is the Biot number indicating the ratio of convection from the surface of the tear film over conduction inside the film. T_∞ is the nondimensional far field temperature; we choose $T_\infty = 0$ meaning it is the same as the saturation temperature $T_s' = 27°\mathrm{C}$ dimensionally. We assume that the free surface is occupied by a strong surfactant (polar lipids in the eye) that renders the surface tangentially immobile [125, 104, 12]. The nondimensional form of the tangential immobility condition is

$$u = 0. \tag{2.7}$$

The thermal Marangoni effect is neglected in the model under the assumption that lipid layer solutal Marangoni effect plays a dominant part. This is reasonable because observations [95] show that tears move rapidly upward over the cornea after a blink because of surfactant concentration gradients and while temperature change is small. The constitutive relation for the evaporative mass flux J gives another boundary condition at the free surface, namely

$$\bar{K} J = \delta(p - p_v) + T, \tag{2.8}$$

with $\bar{K}$ the nonequilibrium parameter that sets the evaporative mass flux and δ relates the pressure difference at the free surface to the evaporation rate.

At the interface between the tear film and the cornea, $y = 0$, we require no slip as well as continuity of temperature and heat flux. These have the dimensionless forms

$$u = v = 0, \ T = T_c, \ \text{and} \ \tilde{k}(L_c'/d')\partial_y T = \partial_{\tilde{y}} T_c. \tag{2.9}$$

A model region representing the cornea and aqueous humor is the rectangular region $\tilde{y}_c \le \tilde{y} \le 0, -1 \le x \le 1$. In this region, heat only diffuses and is governed by:

$$\partial_t T_c = P_T \left[\left(\frac{L_c'}{L'} \right)^2 \partial_x^2 T_c + \partial_{\tilde{y}}^2 T_c \right], \tag{2.10}$$

$$T_c(x, \tilde{y}_c, t) = T_c(\pm 1, \tilde{y}, t) = 1. \tag{2.11}$$

Here T_c denotes the temperature inside the rectangle and $\tilde{k} = k/k_c$ is the ratio of thermal conductivities (tear film over cornea).

A PDE for the tear film thickness, coupled with a heat diffusion equation, is derived by solving for the temperature fields in both the tear film and the cornea; the system to be solved in the thick substrate case is then

$$\partial_t h + EJ + \partial_x q = 0, \quad -1 < x < 1, \ t > 0 \tag{2.12}$$

$$q = \tfrac{h^3}{12}\left[\partial_x\left(S\partial_x^2 h + Ah^{-3}\right) + G\right], \tag{2.13}$$

$$J = \frac{\frac{T_0 + \mathrm{Bi} T_\infty h}{1+\mathrm{Bi} h} - \delta(S\partial_x^2 h + Ah^{-3})}{\bar{K} + \frac{h}{1+\mathrm{Bi} h}}, \tag{2.14}$$

where $T_0 = T(x, 0, t)$, and in the rectangle beneath the film,

$$\partial_t T_c = P_T\left[\left(\tfrac{L_c'}{L'}\right)^2 \partial_x^2 T_c + \partial_{\tilde{y}}^2 T_c\right], \ |x| < 1, \tilde{y}_c < \tilde{y} < 0 \tag{2.15}$$

$$T_c(-1, \tilde{y}, t) = T_c(1, \tilde{y}, t) = T_c(x, \tilde{y}_c, t) = 1, \tag{2.16}$$

$$\tfrac{d'}{L_c'}\partial_{\tilde{y}} T_c(x, 0, t) + \tilde{k}\tfrac{J + \mathrm{Bi}(T_0 - T_\infty)}{1+\mathrm{Bi} h} = 0. \tag{2.17}$$

If we assume $y_c' \ll 1$, i.e. we have the thin substrate case, and apply d' as the length scale for the negative y' direction as well, the PDE system (2.12)–(2.17) is reduced to a single PDE for the tear film thickness, namely,

$$\partial_t h + EJ + \partial_x q = 0, \quad -1 < x < 1, \ t > 0 \tag{2.18}$$

with q being exactly the same as (2.13) and the mass flux term J showing as below.

$$J = \frac{1 - \delta(S\partial_x^2 h + Ah^{-3}) - \frac{\mathrm{Bi}(1-T_\infty)(h-\tilde{k}y_c)}{1+\mathrm{Bi}(h-\tilde{k}y_c)}}{\bar{K} + \frac{h-\tilde{k}y_c}{1+\mathrm{Bi}(h-\tilde{k}y_c)}} \tag{2.19}$$

Furthermore, we may set $y_c' = 0$ in (2.19) and recover the PDE for the case with no substrate as in Winter *et al.* [124] (when Bi= 0).

A feature of this model is that evaporation shuts off when the tear film thickness thins to an equilibrium value denoted by h_{eq}. Approximation of h_{eq} is found from equations (2.18) and (2.19) by seting $J = 0$ and neglecting the spacial derivatives. $\partial_t h = 0$ then follows. With Bi$= 0$, $J = 0$ implies $1 - \delta A h^{-3} = 0$. Thus,

$$h_{eq} = (\delta A)^{1/3}. \tag{2.20}$$

For all these three cases, we assume the tear film thickness is fixed at the ends and there is no flux coming from the boundaries. Hence, we impose the following boundary conditions:

$$h(\pm 1, t) = h_0, \quad q(\pm 1, t) = 0 \tag{2.21}$$

The initial condition that approximates the post-blink geometry of a tear film is specified as

$$h(x, 0) = 1 + (h_0 - 1)x^{2m}. \tag{2.22}$$

We assume an even function for a symmetric initial tear film distribution. Larger values of m specify tear distributions with less fluid in the menisci. Two assumed initial profiles of the temperature field in the rectangle are studied for the thick substrate case. We begin with the uniformly distributed initial temperature profile assumption,

$$T_c(x, \tilde{y}, 0) = 1, \tag{2.23}$$

and then turn to the non-uniformly temperature assumption which gives better agreement with the experimental data,

$$T_c(x, \tilde{y}, 0) = 1 + \frac{1 - T_{\min}}{\tilde{y}_c^2}(\tilde{y} - \tilde{y}_c)^2(x^2 - 1), \tag{2.24}$$

where $T_{\min}$ is the initial temperature at the GCC, to simulate the experimental observation by Efron *et al.* [30].

2.3 Numerical Methods

We investigated three different methods to compute solutions to the problems [71]; they are: (i) the reformulated ordinary differential equation approach (RODE);

(ii) the finite-difference-based differential algebraic equation approach (DAE/fd); and (iii) the spectral-method-based DAE method (DAE/sp) to solve the model numerically. All three methods use a method of lines with discretized spatial derivatives, with the resulting ODEs or DAEs for the dependent variables on the grid points solved using `ode15s` in Matlab (The MathWorks, Inc, Natick, MA). The methods were tested on a model problem; the results and a comparison are given in Section 2.4. Results for the tear film models in Section 2.5 are obtained from both the DAE/fd and DAE/sp methods.

2.3.1 RODE Method

Similar to the ODE method, centered finite difference scheme is used to approximate the spatial derivatives. The RODE method computes the flux q as an intermediate step and then it is differentiated to update h rather than compute $\partial_{xxxx}h$ directly [71]. Therefore, unlike the direct ODE method, which requires the introduction of fictitious points and applying a finite difference approximation of $\partial_x q$ to enforce the flux boundary condition $q(\pm 1, t) = 0$, RODE method uses the exact value of the flux at both ends thus provides more accuracy from the boundaries.

2.3.2 DAE/fd Method

In the DAE method, we reduce the order of derivatives to be evaluated numerically by rewriting the PDE as a semi-explicit DAE of index-1 with the pressure p as a new dependent variable [73],

$$p(x,t) \equiv -(S\partial_x^2 h + Ah^{-3}). \tag{2.25}$$

The thin film equations in the thick substrate case then become (2.12) along with

$$q = \tfrac{h^3}{12}\left(-\partial_x p + G\right), \tag{2.26}$$

$$J = \frac{\frac{T_0 + \mathrm{Bi} T_\infty h}{1+\mathrm{Bi}h} + \delta p}{\bar{K} + \frac{h}{1+\mathrm{Bi}h}}. \tag{2.27}$$

The DAE system now has $\partial_x^2 h$ and $\partial_x^2 p$ being the highest order derivatives, but it has an additional unknown. When we use centered finite difference to approximate all spatial derivatives in the DAE system and use a DAE solver on the resulting system, we call that the DAE/fd method.

2.3.3 DAE/sp Method

In this approach, rather than implement second order finite difference approximation, the DAE/sp method uses a Chebyshev spectral collocation method to discretize all spatial derivatives [22, 115]. The grid points are the second-kind Chebyshev points defined as

$$x_i = \cos\left(\frac{\pi j}{N}\right), \quad j = 0, 1, \ldots, N.$$

This method has better convergence rates for smooth functions and thus requires fewer grid points than finite-difference-based methods to achieve comparable or better accuracy.

2.4 Test Problem

To test and compare the accuracy of these methods, we formulated a test problem similar to the thin substrate tear film PDE with all the tear film parameter values shown in Table A.1. For simplicity, Bi$= G = 0$ in this appendix.

2.4.1 Problem Setup

In the test problem, we create a PDE of the form

$$\partial_t h + EJ + \partial_x q = g(x,t) \tag{2.28}$$

with a space and time dependent forcing term $g(x,t)$ such that it has the exact solution

$$H(x,t) = \frac{1}{1+(t/t_0)^2} + \left[h_0 - \frac{1}{1+(t/t_0)^2}\right] x^{2m}, \tag{2.29}$$

where q and J are the same as equations (2.13) and (2.19) but with Bi$= 0$ and $G = 0$. Initial and boundary conditions are specified as

$$h(x, 0) = 1 + (h_0 - 1)x^{2m}$$

$$h(\pm 1, t) = h_0$$

$$q(\pm 1, t) = \pm \frac{h_0^3}{12}\Big[(2m-1)(2m-2)S - 3Ah_0^{-4}\Big]2m(h_0 - 1)$$

The exact solution (2.29) is chosen to mimic the meniscus and center parts of the tear film. A plot of the exact solution is given in Figure 2.2.

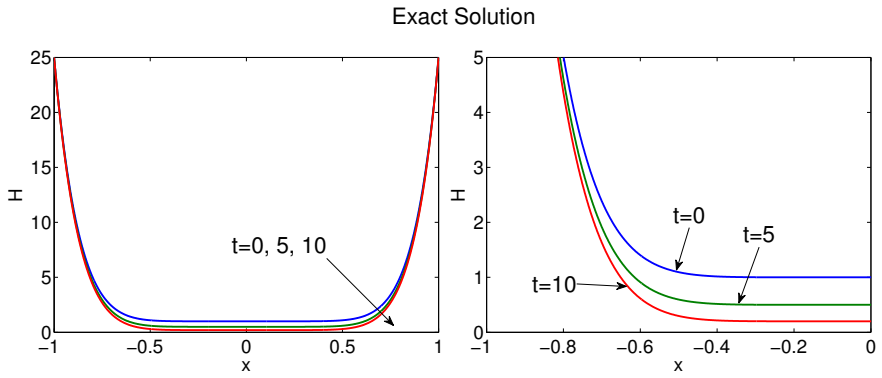

Figure 2.2: Plot of the exact solution $H(x, t)$ in (2.29) with $h_0 = 25$, $t_0 = 2$, $y_c = -4$ and $m = 4$.

2.4.2 Test Problem Results

As shown in Figure 2.2, parameters used in the test problem are $h_0 = 25$, $t_0 = 2$, $y_c = -4$ and $m = 4$, along with the values of E, S, δ, $\bar{K}$ and $\tilde{k}$ being given by TABLE A.1. The number of grid points for the two finite difference based methods varied from 1024 to 4096. Demonstration of second order convergence for these two methods can be seen from the first plot of Figure 2.3. The DAE/fd method performs better than the RODE method. The DAE/sp method shows much better error as shown in the

second plot of Figure 2.3; that plot is for a relative and absolute tolerances of 10^{-10} in the DAE solver. As the number of grid points in the computation is increased, the maximum absolute error decreases; the linear decrease on a semilog plot is comparable to the error derivatives of exponential functions (e.g., Section 6 of Trefethen [115]). The spectral method requires significantly fewer grid points to achieve good accuracy, so the solution is fast even though the Chebyshev differentiation matrices we use are dense.

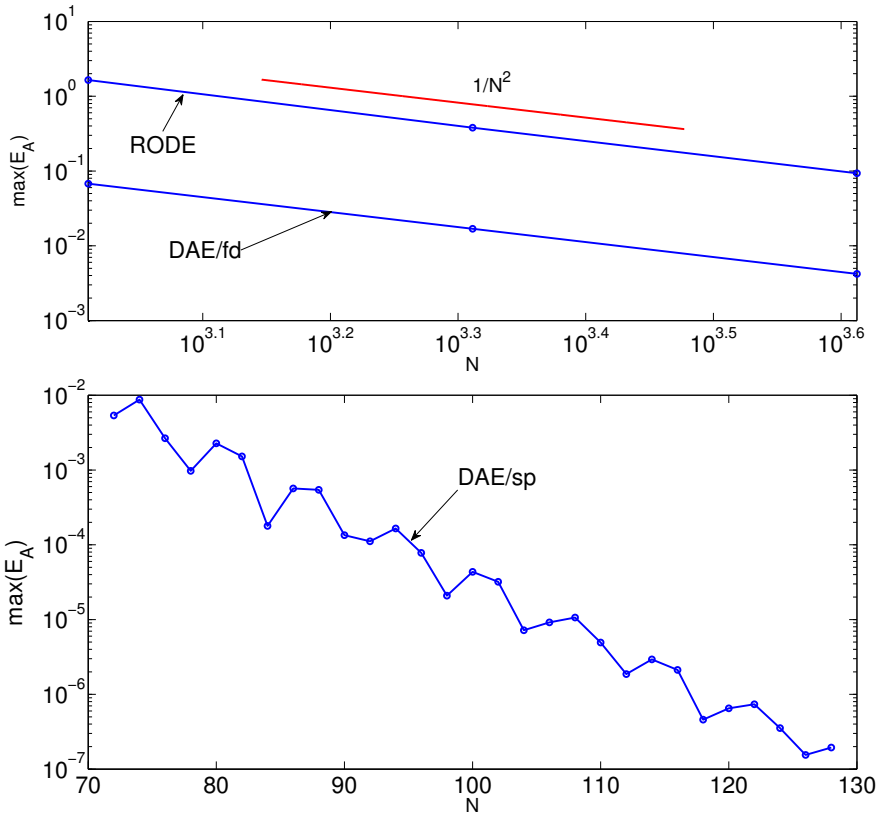

Figure 2.3: Convergence of three methods

To better understand how the error is distributed along the $x-$axis, we plotted the absolute error of various methods at time $t = 7$ in Figure 2.4. We used two scales to present the results because the accuracy of DEA/sp method is better than that of the other two methods. Due to the menisci at both ends, all the three methods have

their maximum error near the ends of the domain in the menisci. The DAE/fd method is about 10 times more accurate than the RODE method.

In addition, as is seen in Figure 2.5, the error of all the methods is accumulating as time increases. 4096 grid points for RODE & DAE/fd methods and 128 grid points for the DAE/sp method were used in the computation to generate Figure 2.4 and 2.5.

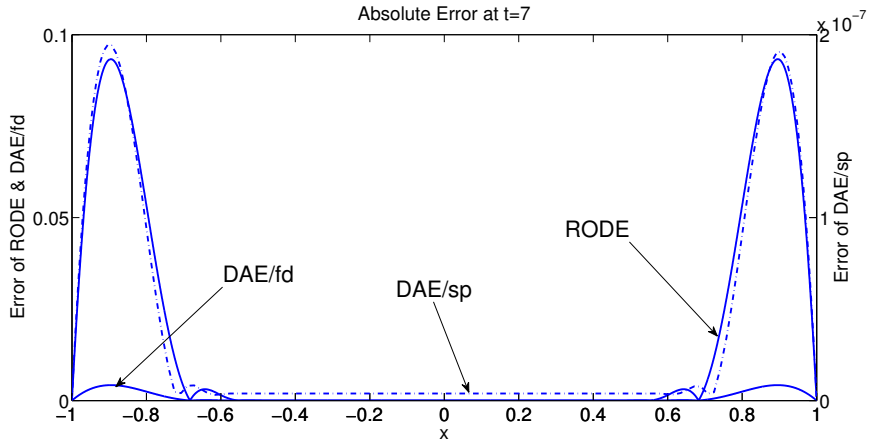

Figure 2.4: Absolute Error at $t = 7$. Left axis shows the scale for RODE and DAE/fd. Right axis scales the error of DAE/sp.

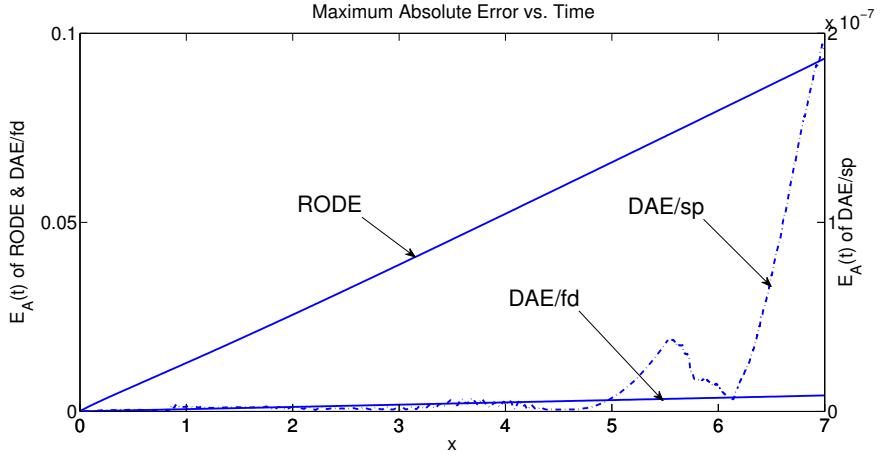

Figure 2.5: Maximum Absolute Error vs Time. Left scales RODE and DAE/fd. Right axis scales DAE/sp.

According to the results from the test problem, DAE/sp is the most accurate method among the three and it also suitable for larger values of h_0, i.e steeper menisci.

However, the code for the DAE/fd methods fails if we raise h_0 to be greater than 35 and the error of RODE fails for $h_0 = 30$.

2.5 Tear Film Results

We now turn to solving the tear film problem. We set $h_0 = 25$ at the boundary and $m = 8$ for the initial condition. All the other parameters are specified as Table A.1 unless otherwise noted.

To begin, we let Bi= 0.01 and $G = 0$ for all three substrate cases to compare results for the tear film surface temperature at the center of the domain ($x = 0$) with experimental GCC temperature measurements. When used to refer to the computed results, GCC will denote the temperature at $x = 0$. Let T_h denote the dimensionless temperature at the surface of the tear film and $\Delta T_h(0,t)$ is the relative GCC temperature change during the computation, which is defined as

$$\Delta T_h(0,t) = \frac{T_h(0,t) - T_h(0,0)}{T_{\text{eq}} - T_h(0,0)}.$$

Here T_{eq} denotes the steady-state GCC temperature at the tear film surface that occurs when $h = h_{eq}$ (equation (2.20)); it was derived by neglecting the x derivatives in the equations. The approximation works well at $x = 0$ and it is given by

$$T_{\text{eq}} = -\frac{\text{Bi}(1 - T_\infty)}{1 + \text{Bi}(h_{\text{eq}} - \tilde{k}y_c)} h_{\text{eq}} + 1 + \frac{\text{Bi}(1 - T_\infty)\tilde{k}y_c}{1 + \text{Bi}(h_{\text{eq}} - \tilde{k}y_c)}$$

with $y_c = 0$ for the no substrate case and $y_c = -4$ for the thin one. Figure 2.6 shows computed GCC temperature for the various cases. From Figure 2.6(a), we observe an increase for the GCC temperature if the no substrate or thin substrate model was used. The relative temperature change shows this, though the magnitude of the change is small, on the order of 10^{-4} to 10^{-3}. We use $\Delta T_h(0,t)$ instead of $T_h(0,t)$ for the no substrate and thin substrate cases to make the changes visible in the plot. The depth of the rectangular substrate for the thin substrate case here is $y_c = -4$, which is 20×10^{-6}m dimensionally. If we consider the thick substrate case, we allow cooling to happen through the cornea and part of aqueous humor; for the figure we used $\tilde{y}_c = -5$,

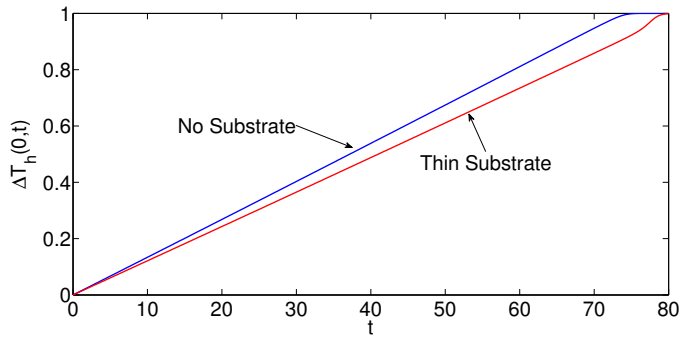

(a) No substrate and thin substrate

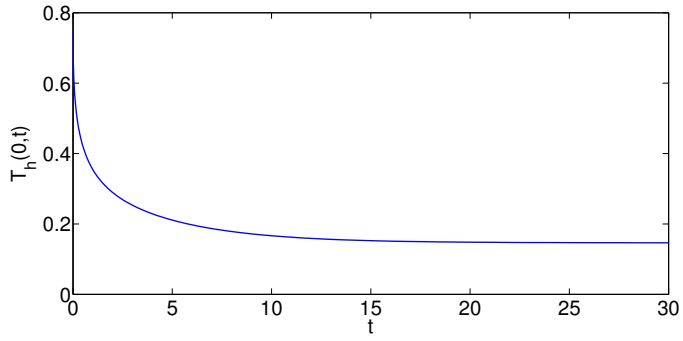

(b) Thick substrate

Figure 2.6: Temperature of the free surface at $x = 0$ for various cases with Bi$=0.01, G = 0$, $y_c = -4$ and $\tilde{y}_c = -5$. Initially, temperature inside the rectangle is set to be body temperature.

which is 2.5×10^{-3}m dimensionally. For the thick substrate case, Figure 2.6(b) shows a decreasing GCC temperature as a function of time. We found that the thick substrate model would generally show a decreasing temperature at GCC, while the other two models did not.

Efron *et al.* [30] measured the rate of cooling at GCC and found that a representative cooling rate was $0.033 \pm 0.024°Cs^{-1}$ for the first $15s$ after a blink. If we fix the cornea at body temperature or allow heat diffusion within only a thin part of the cornea (i.e., the no substrate and the thin substrate cases), then the models actually predict a slight increase of the GCC temperature. Unless the heat diffusion is allowed deeply enough into the aqueous humor, the model cannot predict a noticeable decrease for the film surface temperature at GCC.

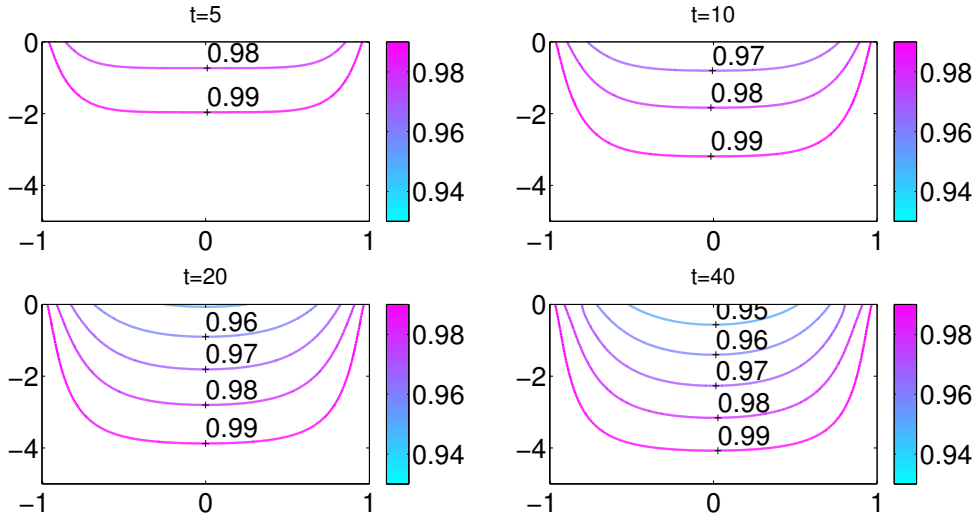

Figure 2.7: Temperature Profile for $T_c(x, \tilde{y}, 0) = 1$,Bi= 0,$G = 0$.

Because the cooling at GCC can be captured only by the thick substrate model, we focused on that case with $\tilde{y}_c = -5$ and then varied the Biot number Bi to study its effects on the temperature distribution and tear film evaporation. Figure 2.7 shows the temperature distribution at several times in the first $t = 40$ (seconds) with Bi= $G = 0$. The temperature decreases along $y = 0$ (the base of the tear film) and into the rectangle as time increases; the other edges of the domain stay at $T = 1$, supplying heat which is then lost through the tear film. Significant cooling into the substrate beneath the tear film occurs, and the minimum temperature is at the origin. The tear film surface temperature is very close to the temperature at $y = 0$ away from the ends of the domain. After 40s, the temperature has decreased well into the rectangle.

The dynamics of the tear film thickness and the corresponding evaporative flux J are shown in Figure 2.8. Since $G = 0$, both h and J are symmetric; only half of the domain is shown here. The formation of the black line [82] near $x = 0.8$ is clearly seen in Figure 2.8(a). The black line refers to localized thin region of the film near the menisci. The film thickness reaches h_{eq} after about $t = 30$, which we interpret to mean that the film has ruptured ("break up" in the eye literature). The corresponding evaporative mass flux is given in Figure 2.8(b). At h_{eq}, the evaporation rate is zero

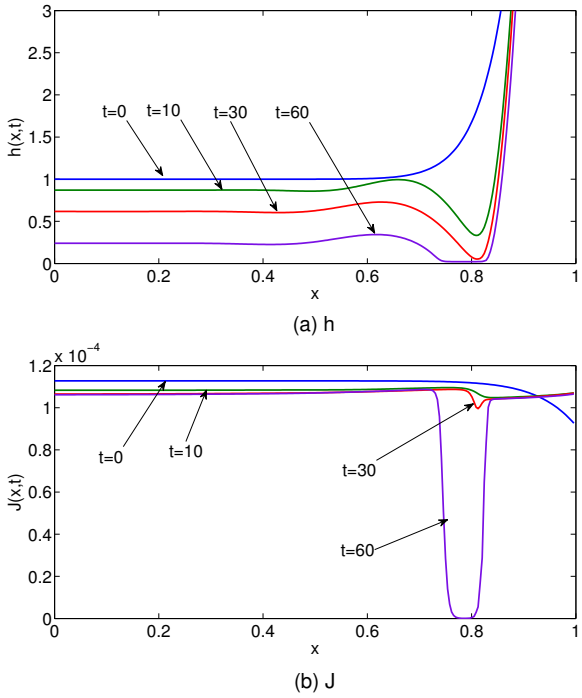

Figure 2.8: Tear film thickness $h(x,t)$ and evaporative mass flux $J(x,t)$ at several times with Bi$= G = 0$.

because of the balance between van der Waals conjoining pressure and tendency to evaporate water from heating of the film [1]; evaporation decreases rapidly as the film thickness approaches h_{eq}. The minimum values of h and J are shown in Figure 2.9. The correlation between the approach to h_{eq} and evaporation shutting off is clearly seen. As is seen in Figure 2.9, after 30 seconds, when the tear film reaches the equilibrium thickness $h_{\text{eq}} = (\delta A)^{1/3}$, the evaporative mass flux vanishes.

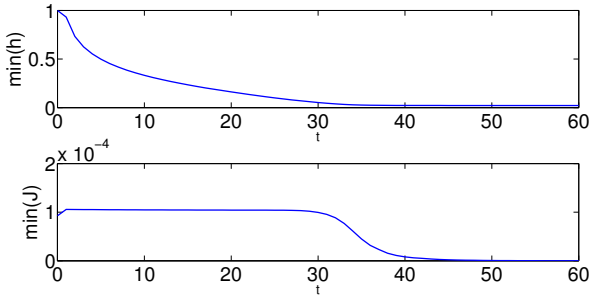

Figure 2.9: min(h) and min(J) as a function of time for Bi$= G = 0$.

The Biot number characterizes relative sizes of the resistance of heat transfer inside and outside the surface of the tear film in air. It has a strong influence on film evaporation and hence has a significant effect on tear film temperature. The tear film thickness and the corresponding evaporative mass flux at the GCC with Bi varying from 0 to 0.1 are plotted in Figure 2.10. The GCC tear film thickness decreases fastest and has the largest evaporative mass flux with Bi= 0. Figure 2.10 clearly shows that increasing the value of Biot number reduces the evaporation rate.

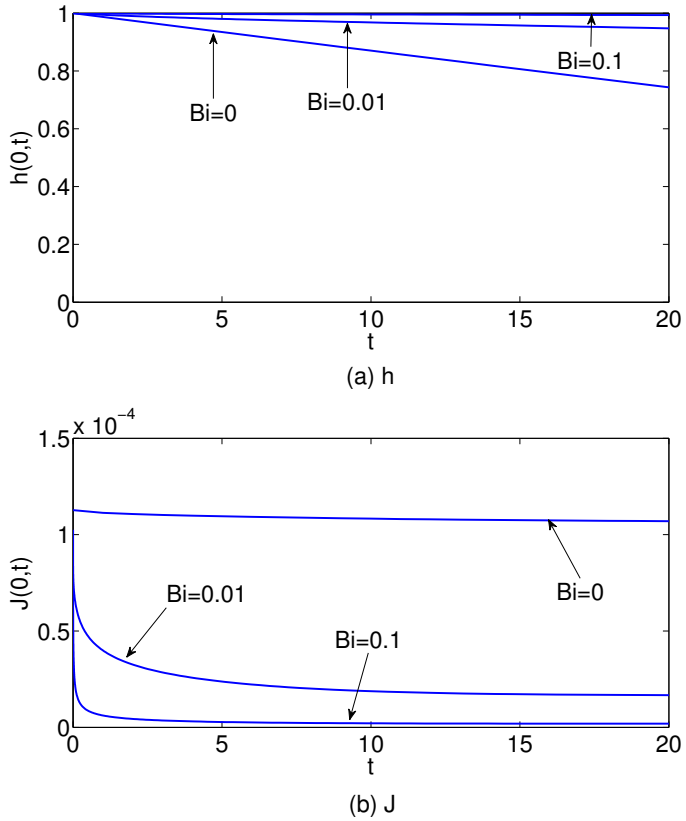

Figure 2.10: $h(x,t)$ and $J(x,t)$ for several values of Bi.

We took advantage of this Biot number dependence to find that Bi=0.0009 best simulates experimental results [30]. In addition, to further improve agreement with the experimental data from Efron *et al.* [30], we used the nonuniform initial condition for T_c given by equation (2.24). This was motivated by the observation that temperatures of the GCC were not at body temperature, but were lower. The initial condition

(2.24) mimics that experimental fact as well as the tendency for the temperature to increase from the GCC towards the periphery of the eye. Figure 2.11 shows how the distribution of the temperature in the rectangular region evolves for the first 40 seconds after a blink. Significant cooling occurs in the substrate beneath the tear film once again, and the minimum temperature is at the origin. $T_{\min} = 0.75$ corresponds to the initial corneal temperature 34.5°C; here $G = 0$. However, we can see from Figure 2.11 that the temperature profile remains unchanged after 20 seconds for this initial condition. Similar observations were made by Efron *et al.* [30], "Inspection suggests a decrease in temperature during the inital 15 to 20s after the blink for all subjects followed by stabilization of temperature in those subjects who were able to maintain eye opening for longer periods."

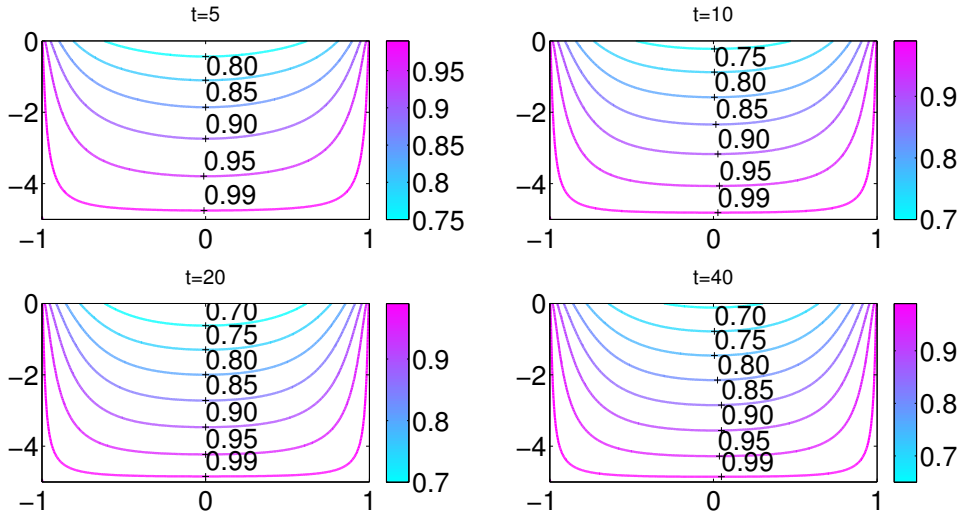

Figure 2.11: Results for the nonuniform temperature initial condition (2.24) with Bi= 0.0009 and $G = 0$.

Our model predicts tear film thickness and its evaporative mass flux with Bi = 0.0009 and initial condition (2.24) for the first 60s after a blink as shown in Figure 2.12. Evidence of the black line formation and subsequent film rupture at around $x = 0.8$ can be clearly seen. Furthermore, the minimum value of h at each time is tracked to produce Figure 2.13.

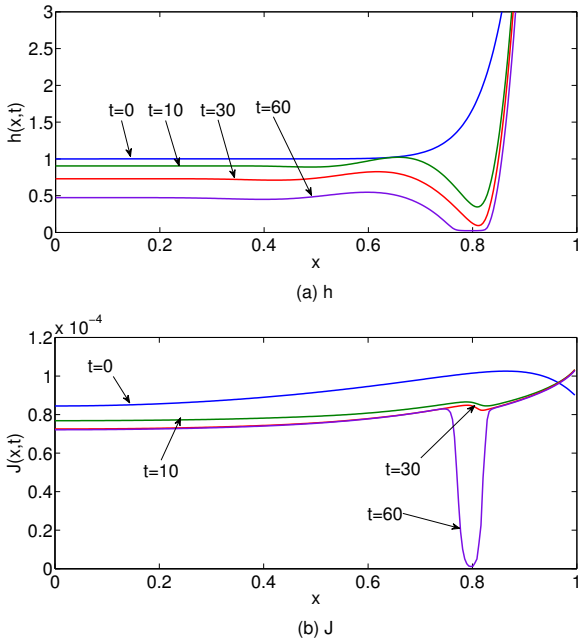

Figure 2.12: Tear film thickness h and evaporative mass flux J.

We now consider $G = 0.05$ as listed in Table A.1. Gravity drives tear film flow in the positive $x-$direction in the model; this effect is shown in Figure 2.14(a). A black line in this case forms more readily at the upper part of the tear film, and break up only occurs near $x = -0.8$ which corresponds to being near the upper lid when gravity is active. Downward flow toward $x = 1$ prevents the lower black line from thinning to h_{eq} as it does at the upper end. In addition, since evaporation shuts off where tear film thickness reaches equilibrium level h_{eq}, $J \to 0$ only near $x = -0.8$ where break up occurs; this is shown in Figure 2.14(b). The shut off of evaporation in the upper black line occurs after about $t = 60$ (one minute dimensionally) in this case.

The thick substrate model has captured several aspects of tear film dynamics; a direct comparison of the model with experiment is given by Figure 2.15. Selected experimental data from Figure 3 in Reference [30] was estimated graphically and plotted in Figure 2.15(a). Computed results for the GCC temperature for Bi= 0.0009 and $G = 0.04$ are also shown. Efron *et al.* [30] concluded, from the right eyes of 21 subjects, that GCC temperature starts at $34.3 \pm 0.7°$C on average with a mean cooling rate of

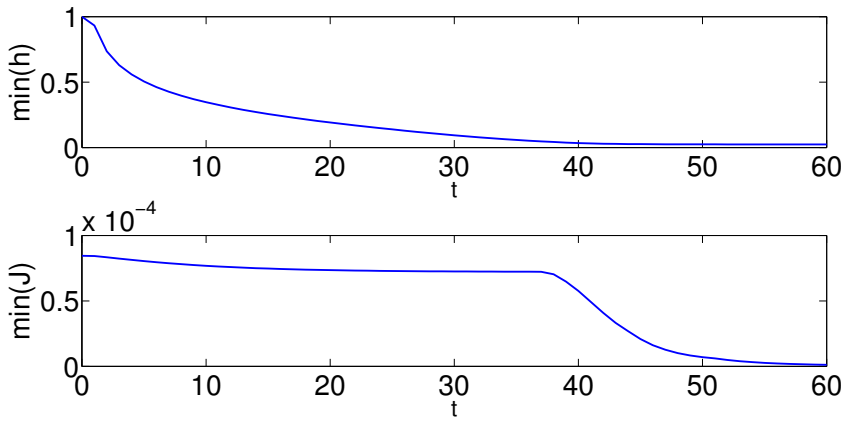

Figure 2.13: $\min h$ and $\min J$.

0.033 ± 0.024°C over the initial 15s. Calculating results from the model predicts the average cooling rate to be 0.058°Cs^{-1} for the first 15s if the initial GCC temperature is set to 34.5°C.

The model is promising for simulating the tear film thinning rate. Nichols *et al.* [92] found the mean rate of thinning of the tear film *in vivo* to $(6.32 \pm 7.00) \times 10^{-8}$ms^{-1} (or $3.79 \pm 4.20\mu$m/min). The average initial thickness in their work was 3.98μm with standard deviation 1.06μm. Our computed results for the GCC tear film thickness are shown in Figure 2.15(b). The model gives a thinning rate of 4.42×10^{-8}ms^{-1} (2.65μm/min) for the initial 15s. This value is well within the experimental range.

Some outlying cases were observed in the experiments [30], however, showing that GCC temperature drops faster than the average and abruptly stopped due to blinking. The GCC temperature doesn't seem to equilibrate in these cases. In addition, observations from King-Smith [92] indicate the rates of tear film thinning ranged from 2 μm/min to 20μm/min with some relatively rare cases far from the average. All the aforementioned results are based on the parameters listed in Table A.1. There, the non-equilibrium coefficient K and the corresponding dimensionless parameter $\bar{K}$ were derived to recover the average thinning rate 4μm/min. To see what the model predicts for the rare cases, we changed the assumptions to determine the values for K and $\bar{K}$. The results are plotted in Figure 2.16, where the GCC temperature dynamics

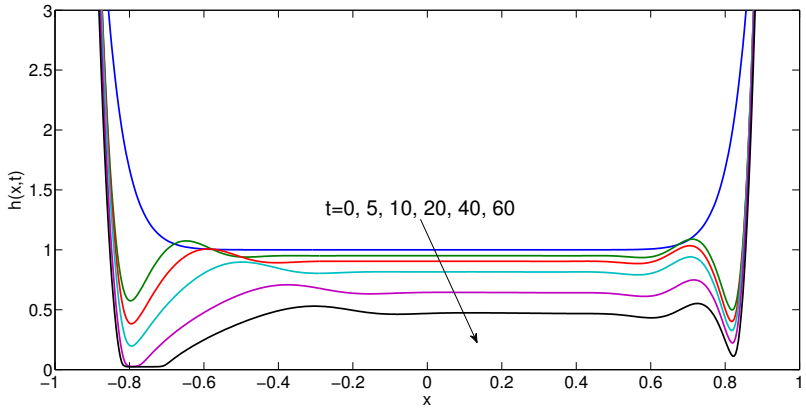

(a) h

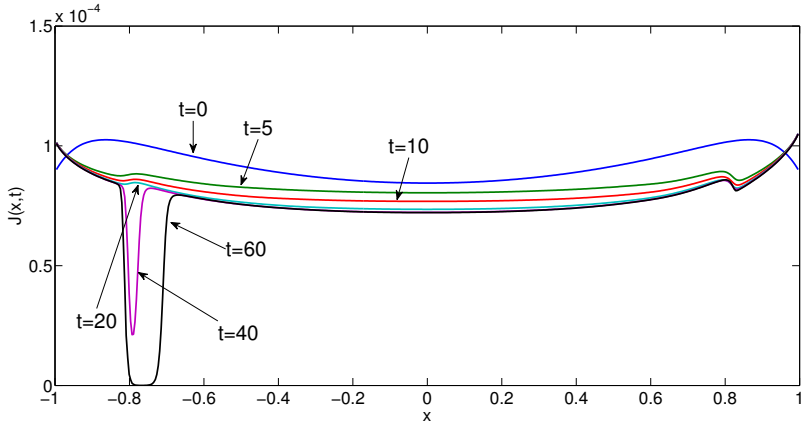

(b) J

Figure 2.14: $h(x,t)$ and $J(x,t)$ for several times with Bi= 0.0009 and $G = 0.05$.

for thinning rates of 4, 12 and 20μm/min are shown. Temperature drops significantly faster during the initial 20s for the larger thinning rates, but it bounces back to reach a steady state value once $h_{\rm eq}$ is reached and evaporation stops. If x derivatives are neglected, the steady-state temperature at the film surface is found to be

$$T_h(0,t) \to \frac{\frac{1}{\tilde{y}_c} - \tilde{k}\frac{L_c' \mathrm{Bi}}{d'(1+\mathrm{Bi}h_{\rm eq})}T_\infty}{\frac{1}{\tilde{y}_c} - \tilde{k}\frac{L_c' \mathrm{Bi}}{d'(1+\mathrm{Bi}h_{\rm eq})}} \approx 0.655. \tag{2.30}$$

The numerical values is that for Bi=0.0009, $G = 0$ and apart from $\bar{K}$ all other values are as given in Table A.1; note that this equilibrium temperature is independent of

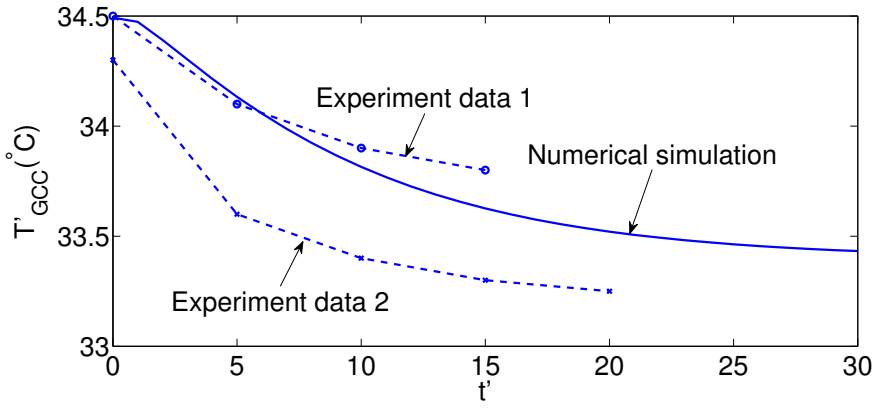

(a) GCC temperature

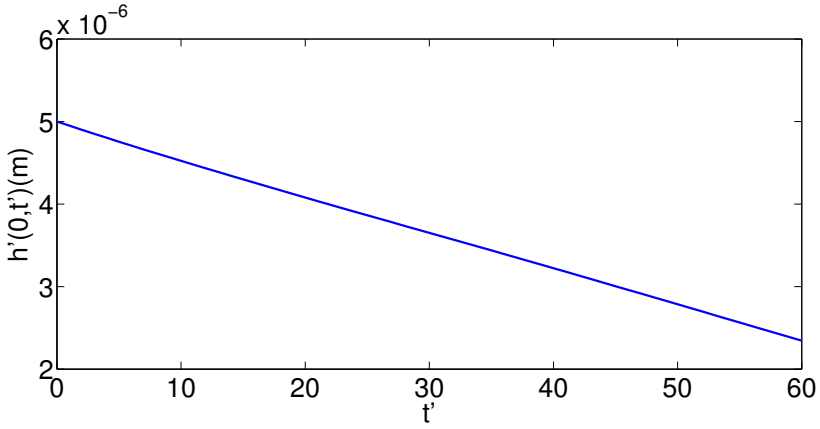

(b) Tear film thickness at GCC

Figure 2.15: Comparison of Numerical simulation to experiment data.

$\bar{K}$ however. The numerical results agree well with the approximate equilibrium temperature. In experiment, blinks interrupted the temperature dynamics, so we don't know what would happen if these subjects were to keep their eyes open long enough. Experiments with subjects that are determined to keep their eyes open may be able to verify or disprove the predicted equilibrium temperature.

Scott's axisymmetric FE model [103] of heat transfer in the eye yielded an equilibrium temperature of 33.25°C using her control parameters. Ng and Ooi's 2D [89] and 3D [90] FE models found mean values of maximum surface temperature of the cornea to be 33.64 and 34.48°C , respectively. The model in this paper predicts the GCC temperature equilibrate to 33.55°C. Our results are comparable to 2D FE

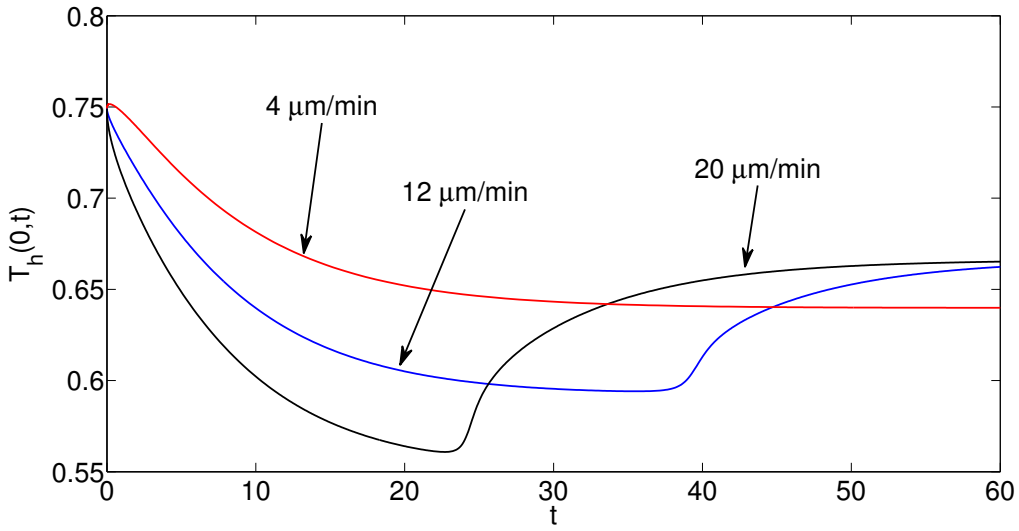

Figure 2.16: GCC temperature evolution for various thinning rate assumptions.

models.

2.6 Conclusion

The model we present in this Chapter includes a rectangular domain underneath the tear film that simulates the cornea and part of the aqueous humor. We allow heat diffusion inside this model rectangle to improve the existing models on predicting the thermal dynamics of the tear film. By varying the depth of the rectangle from 0 to 2.5×10^{-3}m, we found that cooling for deep enough into the eye, the model could recover the experimental data for temperature at the tear film and the ocular surface cooling with evaporation and heat loss; without a thick substrate, the tear film temperature actually increases slightly.

Varying the Biot number in the model reveals the important role it plays in tear film evaporation. Large Bi implies heat has another route to leave the tear film besides evaporation, and so evaporation slows down with increasing Bi (pictured in Figure 2.10). Hence, we could adjust the value of Bi number to control the evaporation rate and we chose Bi= 0.0009 to match experimental data.

To summarize, we present a tear film dynamics model that has improved dynamics for the temperature at its surface in this Chapter. This improvement comes from including heat diffusion in both the tear film and the eye beneath it. Allowing cooling to penetrate deep enough into the eye eventually captures the right thermal behavior as well as thinning rates in the experimentally measured range.

Chapter 3

MODELING TEAR FILM AND OSMOLARITY DYNAMICS ON AN EYE SHAPED DOMAIN

3.1 Introduction

The purpose of the model we develop in this Chapter is to compute the dynamics of fluid motion and osmolarity of the tear film on an eye-shaped domain. Osmolarity is the concentration of ions in solution. Given a 1M concentration of NaCl solution, each molecule of salt dissociates into two ions, and the osmolarity is then 2M. (Here M denotes molar concentration, which is moles per liter of solvent.) For a brief introduction to the mathematical models for the osmolarity and tear film dynamics, see the review by Braun [11] or the paper by Zubkov *et al.* [127].

The osmolarity is an important variable to include in tear film modeling because it is thought to be critical in the onset and subsequent development of dry eye syndrome (DES). We summarize a discussion of the role of osmolarity on the ocular surface from Baudouin *et al.* [8] here. According to Tietz [111], in healthy blood the osmolarity is in the range 285-295 Osm/m^3 (also denoted mOsm/L or mOsM). In the healthy tear film, there is homeostasis with the blood in the range 296-302 Osm/m^3 [63, 114, 117]. In DES, the lacrimal system is unable to maintain this homeostasis and osmolarity values in the meniscus rise to 316-360 Osm/m^3 [114, 35, 109], and may rise to even higher values over the cornea. Using *in vivo* experiment and sensory feedback, Liu *et al.* [69] estimated peak values of 800-900 Osm/m^3. Similar or higher values were computed from mathematical models of tear film break up in King-Smith *et al.* [59] and Peng *et al.* [96]. These estimated osmolarity in break up are easily enough to cause discomfort [69]. Though we don't include localized evaporation to induce break up, we find thinning induces localized increases in osmolarity that are also significant.

We use a mathematical model to compute osmolarity over the entire exposed ocular surface subject to the assumptions stated in the Formulation section §3.2.

The method of tear sample collection and measurement is important. To our knowledge, osmolarity measurements in humans have been from samples in the inferior meniscus or the lower fornix. The lower fornix has a lower osmolarity than the meniscus [85], and samples from the meniscus are most commonly used today. Gilbard *et al.* [35] summarized the use of prior measurement techniques that used pipettes or capillary tubes to collect tear samples. Older methods may have used pipettes that took too large a sample compared to the tear film total volume, and could induce reflex tearing. In the exquisitely sensitive eye, this is a significant concern that could dilute or otherwise change the chemistry of the tear sample. Some capillary techniques are difficult to use, and the method of Gilbard *et al.* [35] appeared to be easier to use; we note that the paper does not indicate where in the inferior meniscus the measurement was taken. Subsequent to sample collection, older techniques relied on freezing point depression to determine the osmolarity of the sample to about 1% error. More recently, a calibrated resistance measurement using the TearLab device allows rapid determination of osmolarity with an error for *in vitro* samples of about 1-2% error [63, 110]. In the approach, a sensor is touch to the meniscus at the temporal canthus, and the result is returned in less than a minute after the sample is taken. The latter approach is much more convenient for clinical use.

The level of effectiveness of osmolarity measurement to diagnose dry eye and to measure progression of the disease is still a matter of debate; for recent viewpoints, see for example, Lemp *et al.* [63]; Amparo *et al.* [6, 5]; Pepose *et al.* [97]; Sullivan [108]. We found the summary by Baudouin *et al.* [8] in their sections III and IV to be informative. We do not aim to settle the debate here, but to supply context for the measurements in the form of a quantitative prediction of the osmolarity over the entire exposed ocular surface to aid interpretation.

In this Chapter, we formulate a tear film dynamics model on a 2D eye-shaped domain that incorporates osmolarity transport and osmosis from the tear/eye interface.

In an effort to mimic some effects of blinks on a stationary boundary, we specify the normal component of the flux at the boundary with both time and space dependence (flux cycle). The time-dependent flux boundary condition is formulated according to Doane's mechanism for tear drainage [28] and the tear drainage model of Zhu and Chauhan [126], but with simplification regarding blinking: there is no lid motion. The permeability of the ocular surface will be either constant over the whole surface, or a space-dependent function with lower permeability over the cornea and higher permeability over the conjunctiva. The model will lose water via evaporation to the air, gain water from the ocular surface, and, via the flux boundary condition, will have water supplied as from the lacrimal gland and removed as from the puncta.

3.2 Formulation

In this section, we present a mathematical model that incorporates osmolarity and fluid dynamics into a tear film model on a 2D eye shaped domain as shown in Figure 3.1. In Figure 3.1, (u', v', w') are the velocity components in the coordinate directions (x', y', z'); z' is directed out of the page and primed variables are dimensional. g' is gravity which is specified in the negative y' direction.

The boundary curves of the eye-shaped domain are approximated from a digital photo by four polynomials. Two are parabolas in x' and two are ninth-degree polynomials in y', and C_4 continuity is imposed where they join (indicated by dots) [72, 73, 67]. s' is the arc length of the boundary starting at the joint of the nasal canthus and upper lid, and is traversed in the counterclockwise direction as s' increases. The unit vectors tangential and normal to the boundary curves are given by $\mathbf{t}'_b$ and $\mathbf{n}'_b$, respectively. $z' = h'(x', y', t')$ denotes the free surface of tear film and t' is the time.

We assume that the tear fluid is incompressible and Newtonian with constant density ρ, viscosity μ, specific heat c_p, and thermal conductivity k. We also assume the ocular surface is flat due to the fact that the characteristic thickness of the human tear film is much less than the radius of curvature of the ocular globe [10, 16]. The governing equations for the tear film thickness h' and the osmolarity c' are derived from

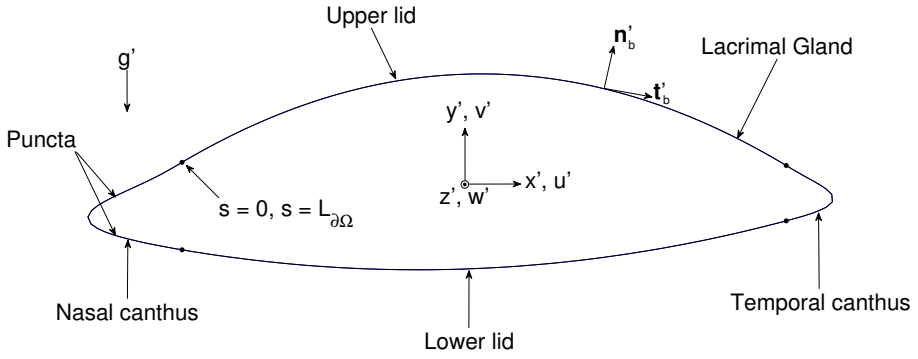

Figure 3.1: The coordinate system and eye-shaped domain. The z' direction points out of the page.

the incompressible Navier-Stokes and convection-diffusion equations, respectively. The two equations are coupled by the osmotic flux, that is, the fluid that flows from the ocular surface at $z' = 0$ into the tear film driven by the osmolarity difference between the tear film and the cornea [65]. In the model, water is lost to the air, treated as a passive gas outside the tear film ($z' > h'$), and water is supplied due to the subsequent increased osmolarity via this osmotic flux.

To be specific, we show detailed derivation of the model system below. The nondimensional parameters that arise are defined and given values in Appendix A and in Table A.1. The dimensional parameters are given in Table A.2.

3.2.1 Model Derivation

Inside the tear fluid, we model the tear film fluid with the incompressible Navier-Stokes equations and energy conservation equation, and model the osmolarity dynamics

with convection-diffusion equation. Namely, in $0 < z' < h'(x', y', t')$:

$$\rho\left(\partial_{t'}\mathbf{u}' + \mathbf{u}' \cdot \nabla \mathbf{u}'\right) = -\nabla p' + \mu \Delta \mathbf{u}' - \rho g \mathbf{j}, \tag{3.1}$$

$$\rho c_p(\partial_{t'} T' + \mathbf{u}' \cdot \nabla T') = k \Delta T', \tag{3.2}$$

$$\nabla \cdot \mathbf{u}' = 0, \tag{3.3}$$

$$\partial_t c' + \nabla \cdot (c' \mathbf{u}') = D_c \Delta c'. \tag{3.4}$$

Here c' is the volumetric concentration of osmotically active physiological salts in the aqueous layer. Typically, it is the ion concentration from these salts that contribute to osmosis and we interpret c' this way. It is measured in units of $\mathrm{Osm/m^3}$. D_c is the diffusion coefficient of osmolarity. $(\mathbf{i}, \mathbf{j}, \mathbf{k})$ are the standard basis vectors.

At the free surface, $z' = h'$, we have the equations to balance fluid mass and energy:

$$J' = \rho(\mathbf{u}' - \mathbf{u}_I') \cdot \mathbf{n}', \tag{3.5}$$

$$L_m J' + k \mathbf{n}' \cdot \nabla T' = 0. \tag{3.6}$$

Here $\mathbf{u}_I' = \partial_t' h' \mathbf{k}$ is the interfacial velocity and $\mathbf{n}'$ is the normal vector to the tear film surface. The difference between $\partial_t' h'$ and w' at the free surface is due to evaporation. We also assume tangential immobility and we balance normal stress with the conjoining pressure under consideration:

$$\mathbf{u}' \cdot \mathbf{t}_1' = \mathbf{u}' \cdot \mathbf{t}_2' = 0, \tag{3.7}$$

$$-p_v' - \mathbf{n}' \cdot \mathbf{T}' \cdot \mathbf{n}' = \sigma \nabla \cdot \mathbf{n}' - \Pi'. \tag{3.8}$$

Here $\mathbf{t}_1'$ and $\mathbf{t}_2'$ are a pair of orthogonal tangential vectors of the tear film surface, $\mathbf{T}' = -p'\mathbf{I} + \mu(\nabla \mathbf{u}' + \nabla \mathbf{u}'^T)$ is the Newtonian stress tensor, and $\Pi' = A^*/h'^3$ is the conjoining pressure. Finally, we relate the interfacial temperature to the mass flux and pressure jump by the nonequilibrium condition, and we impose a no-flux condition for the osmolarity,

$$KJ' = \alpha(p' - p_v') + T' - T_s', \tag{3.9}$$

$$(\mathbf{u}' - \mathbf{u}_I')c' \cdot \mathbf{n}' = D_c \nabla c' \cdot \mathbf{n}'. \tag{3.10}$$

Since we model the evaporative mass flux J' as

$$J' = \rho(\mathbf{u}' - \mathbf{u}'_I) \cdot \mathbf{n}',$$

the no-flux condition for osmolarity at the free surface becomes

$$D_c \nabla c' \cdot \mathbf{n}' = \frac{c' J'}{\rho}.$$

At the cornea-tear film interface, $z' = 0'$, in addition to the specification of no-slip conditions and the prescription of body temperature, we allow water to go through the ocular surface by osmosis, but keep the ions in the tear film from penetrating the ocular surface, thus we have

$$u' = v' = 0, \tag{3.11}$$

$$T' = T'_B, \tag{3.12}$$

$$w' = P'_c(c' - c'_0), \tag{3.13}$$

$$w'c' = D_c \partial'_z c'. \tag{3.14}$$

Here $c'_0 = 302$ Osm/m^3 is the isotonic concentration, which is used to scale c'.

The following scales are used to non-dimensionalize the equations:

$$x' = L'x,\ y' = L'y,\ z' = d'z,\ h' = d'h,\ c' = c'_0\bar{c},\ u' = U_0 u,\ v' = U_0 v,\ t' = \frac{L'}{U_0}t,$$
$$w' = \frac{d'U_0}{L'}w,\ p' = \frac{\mu U_0}{L'\epsilon^2}p,\ T = \frac{T' - T'_s}{T'_B - T'_s},\ J' = \frac{k}{d'\mathcal{L}_m}(T'_B - T'_s)J.$$

Here $\epsilon = d'/L' \ll 1$ indicates the separation of length scales. After non-dimensionalization, we have,

in $0 < z < h(x, y, t)$,

$$\epsilon^2 \mathrm{Re}\left(\partial_t u + u\partial_x u + v\partial_y u + w\partial_z u\right) = -\partial_x p + \left(\epsilon^2\partial_x^2 u + \epsilon^2\partial_y^2 u + \partial_z^2 u\right),$$

$$\epsilon^2 \mathrm{Re}\left(\partial_t v + u\partial_x v + v\partial_y v + w\partial_z v\right) = -\partial_y p + \left(\epsilon^2\partial_x^2 v + \epsilon^2\partial_y^2 v + \partial_z^2 v\right) - G,$$

$$\epsilon^4 \mathrm{Re}\left(\partial_t w + u\partial_x w + v\partial_y w + w\partial_z w\right) = -\partial_z p + \epsilon^2\left(\epsilon^2\partial_x^2 w + \epsilon^2\partial_y^2 w + \partial_z^2 w\right),$$

$$\epsilon^2 \mathrm{RePr}\left(\partial_t T + u\partial_x T + v\partial_y T + w\partial_z T\right) = \epsilon^2\left(\partial_x^2 T + \partial_y^2 T\right) + \partial_z^2 T,$$

$$\partial_x u + \partial_y v + \partial_z w = 0,$$

$$\epsilon^2 \mathrm{Pe}_c\left(\partial_t \bar{c} + u\partial_x \bar{c} + v\partial_y \bar{c} + w\partial_z \bar{c}\right) = \epsilon^2\partial_x^2\bar{c} + \epsilon^2\partial_y^2\bar{c} + \partial_z^2\bar{c},$$

at $z = h(x, y, t)$,

$$EJ = \frac{-u\partial_x h - v\partial_y h + w - \partial_t h}{\sqrt{1 + \epsilon^2 \left(\partial_x h\right)^2 + \epsilon^2 \left(\partial_y h\right)^2}},$$

$$J + \frac{-\epsilon^2 \partial_x h \partial_x T - \epsilon^2 \partial_y h \partial_y T + \partial_z T}{\sqrt{1 + \epsilon^2 \left(\partial_x h\right)^2 + \epsilon^2 \left(\partial_y h\right)^2}} = 0,$$

$$\frac{v + \epsilon^2 w \partial_y h}{\sqrt{1 + \epsilon^2 \left(\partial_y h\right)^2}} = \frac{u + \epsilon^2 w \partial_x h}{\sqrt{1 + \epsilon^2 \left(\partial_x h\right)^2}} = 0,$$

$$p - p_v - \frac{2\epsilon^2 \left[\epsilon^2 \left(\partial_x^2 h \partial_x u + \partial_y^2 h \partial_y v + \partial_x h \partial_y h (\partial_y u + \partial_x v) - \partial_x h \partial_x w - \partial_y h \partial_y w\right) + \partial_z w - \partial_x h \partial_z u - \partial_y h \partial_z v\right]}{\sqrt{1 + \epsilon^2 \left(\partial_x h\right)^2 + \epsilon^2 \left(\partial_y h\right)^2}}$$

$$= -S \left[\partial_x \left(\frac{\partial_x h}{\sqrt{1 + \epsilon^2 \left(\partial_x h\right)^2 + \epsilon^2 \left(\partial_y h\right)^2}}\right) + \partial_y \left(\frac{\partial_y h}{\sqrt{1 + \epsilon^2 \left(\partial_x h\right)^2 + \epsilon^2 \left(\partial_y h\right)^2}}\right)\right] - \frac{A}{h^3},$$

$$\bar{K} J = \delta \left(p - p_v\right) + T,$$

$$-\epsilon^2 \partial_x h \partial_x \bar{c} - \epsilon^2 \partial_y h \partial_y \bar{c} + \partial_z \bar{c} = E \mathrm{Pe}_c \epsilon^2 \bar{c} J \sqrt{1 + \epsilon^2 \left(\partial_x h\right)^2 + \epsilon^2 \left(\partial_y h\right)^2},$$

at $z = 0$,

$$u = v = 0, \quad T = 1,$$

$$w = P_c(\bar{c} - 1),$$

$$\epsilon^2 \mathrm{Pe}_c w \bar{c} = \partial_z \bar{c}.$$

Lubrication theory exploits the small value of ϵ, which is the ratio of the tear film thickness to the length scale along the tear film. E characterizes the evaporative contribution to the surface motion, δ measures the pressure influence to evaporation, S is the ratio of surface tension to viscous forces, A is the Hamaker constant in nondimensional form related to the unretarded van der Waals force, G is the ratio of gravity to the viscous force, $\bar{K}$ represents the non-equilibrium parameter that sets the evaporative mass flux, Pe_c is the Péclet number for the osmolarity describing the competition between convection and diffusion, and $P_c = P^{\mathrm{tiss}} v_w c_0' / (\epsilon U_0)$ is the nondimensional permeability of the ocular surface. The tissue permeability P^{tiss} will take on different values as described in Section 3.2.2.

We estimate the size of the non-dimensional parameters:

$$\epsilon = \frac{d'}{L'} = 1 \times 10^{-3}, \quad \mathrm{Re} = \frac{U_0 L'}{\mu/\rho} \approx 19.23, \quad \mathrm{Pr} = \frac{c_p \mu}{k} \approx 8.01,$$

where Re is the Reynolds number and Pr is the Prandtl number. Terms involving the following parameters are regarded as small:

$$\epsilon^2 = 1 \times 10^{-6}, \quad \epsilon^2 \mathrm{Re} \approx 1.92 \times 10^{-5}, \quad \epsilon^2 \mathrm{RePr} \approx 1.54 \times 10^{-4}.$$

Applying lubrication theory by neglecting all the small terms for the fluid equations, we then have the following leading order approximations.

In $0 < z < h(x, y, t)$:

$$0 = -\partial_x p + \partial_z^2 u, \tag{3.15}$$
$$0 = -\partial_y p + \partial_z^2 v - G, \tag{3.16}$$
$$0 = -\partial_z p, \tag{3.17}$$
$$0 = \partial_z^2 T, \tag{3.18}$$
$$\partial_x u + \partial_y v + \partial_z w = 0. \tag{3.19}$$

For the osmolarity, we expand $\bar{c}(x, y, z, t)$ as

$$\bar{c} = \bar{c}_0 + \epsilon^2 \bar{c}_1 + O(\epsilon^4).$$

So the leading order equation is

$$\partial_z \bar{c}_0 = 0, \tag{3.20}$$

which implies $\bar{c}_0$ is independent of z, i.e. $\bar{c}_0 = \bar{c}_0(x, y, t)$. We proceed to the next order so as to find an equation for $\bar{c}_0$, and we obtain

$$\partial_z^2 \bar{c}_1 = \mathrm{Pe}_c \left[\partial_t \bar{c}_0 + (u \partial_x \bar{c}_0 + v \partial_y \bar{c}_0)\right] - \partial_x^2 \bar{c}_0 - \partial_y^2 \bar{c}_0. \tag{3.21}$$

At $z = h(x, y, t)$:

$$EJ = -u \partial_x h - v \partial_y h + w - \partial_t h, \tag{3.22}$$
$$J + \partial_z T = 0, \tag{3.23}$$
$$u = v = 0, \tag{3.24}$$
$$p - p_v = -S \left(\partial_x^2 h + \partial_y^2 h\right) - \frac{A}{h^3}, \tag{3.25}$$
$$\bar{K} J = \delta \left(p - p_v\right) + T, \tag{3.26}$$
$$\partial_z \bar{c}_1 = E \mathrm{Pe}_c \bar{c}_0 J + \nabla h \cdot \nabla \bar{c}_0. \tag{3.27}$$

For convenience, we use $\nabla = (\partial_x, \partial_y)$ and $\Delta = (\partial_x^2 + \partial_y^2)$ to represent the differential operators applied on h and $\bar{c}_0$ since both are independent on z.

At $z = 0$:

$$u = v = 0, \tag{3.28}$$
$$T = 1, \tag{3.29}$$
$$w = P_c(\bar{c}_0 - 1), \tag{3.30}$$
$$\partial_z \bar{c}_1 = \mathrm{Pe}_c P_c(\bar{c}_0 - 1)\bar{c}_0. \tag{3.31}$$

For the tear film, we first integrate Equation (3.19) with respect to z from 0 to h and obtain

$$w(x, y, h, t) = w(x, y, 0, t) - \int_0^h \left(\partial_x u(x, y, z, t) + \partial_y v(x, y, z, t)\right) dz. \tag{3.32}$$

After substituting Equation (3.32) into boundary condition (3.22), we have

$$\text{at } z = h: \; EJ = -u\partial_x h - v\partial_y h + w(x, y, 0, t) - \int_0^h \left(\partial_x u + \partial_y v\right) dz - \partial_t h. \tag{3.33}$$

Utilizing the Leibniz integral rule, we can simplify Equation (3.33) as

$$\partial_t h + EJ + \left(\partial_x \int_0^h u\, dz + \partial_y \int_0^h v\, dz\right) - w(x, y, 0, t) = 0. \tag{3.34}$$

Further manipulation together with boundary condition (3.30) yield

$$\partial_t h + EJ + \nabla \cdot \left(\int_0^h u\, dz, \int_0^h v\, dz\right) - P_c(\bar{c}_0 - 1) = 0.$$

Here $\nabla = (\partial_x, \partial_y)$ is the gradient operator. If we denote the fluid flux at any cross section as

$$\mathbf{Q} = \left(\int_0^h u\, dz, \int_0^h v\, dz\right),$$

we then get

$$\partial_t h + EJ + \nabla \cdot \mathbf{Q} - P_c(\bar{c}_0 - 1) = 0.$$

We now turn to solve for $\mathbf{Q}$ and J in terms of h so as to find a PDE for $h(x, y, t)$. From Equation (3.17), we know that p is independent of z, i.e., $p = p(x, y, t)$. So we integrate Equations (3.15) and (3.16) with respect to z twice and obtain

$$u = \frac{1}{2}\partial_x p z^2 + b_1 z + b_2, \quad v = \frac{1}{2}\left(\partial_y p + G\right) z^2 + c_1 z + c_2.$$

From boundary conditions (3.24) and (3.28), we solve for b_1, b_2, c_1 and c_2, and therefore, we have

$$u = \frac{1}{2}\partial_x p z^2 - \frac{1}{2}\partial_x p h z, \quad v = \frac{1}{2}\left(\partial_y p + G\right) z^2 - \frac{1}{2}\left(\partial_y p + G\right) h z.$$

Furthermore,

$$\mathbf{Q} = \left(\int_0^h u\, dz, \int_0^h v\, dz\right) = \left(-\frac{1}{12}\partial_x p h^3, -\frac{1}{12}\left(\partial_y p + G\right) h^3\right) = -\frac{1}{12} h^3 \nabla(p + Gy).$$

In addition, from Equation (3.25), we know

$$\nabla(p + Gy) = -\nabla(S\Delta h + \frac{A}{h^3} - Gy),$$

hence, we have derived the equation for $\mathbf{Q}$ in terms of h:

$$\mathbf{Q} = \frac{h^3}{12}\nabla\left(S\Delta h + Ah^{-3} - Gy\right).$$

In order to solve for J, we integrate Equation (3.19), and then we obtain

$$T(x, y, z, t) = a_1(x, y, t)z + a_2(x, y, t).$$

Boundary conditions (3.23) & (3.29) imply

$$T(x, y, z, t) = -Jz + 1.$$

According to boundary conditions (3.25) & (3.26), we have

$$\bar{K}J = \delta\left(-S\Delta h - \frac{A}{h^3}\right) - Jh + 1.$$

Solving for J, we then obtain

$$J = \frac{1 - \delta\left(S\Delta h + Ah^{-3}\right)}{\bar{K} + h}.$$

Thus, after solving for the velocity and temperature fields, integrate the mass conservation equation and use the kinematic condition, we arrive at a PDE for $h(x, y, t)$:

$$\partial_t h + EJ + \nabla \cdot \mathbf{Q} - P_c(\bar{c}_0 - 1) = 0,$$

with

$$J = \frac{1 - \delta\left(S\Delta h + Ah^{-3}\right)}{\bar{K} + h} \quad \text{and} \quad \mathbf{Q} = \frac{h^3}{12}\nabla\left(S\Delta h + Ah^{-3} - Gy\right).$$

For the osmolarity, we integrate Equation (3.21) with respect to z from 0 to h. Noting that $\bar{c}_0 = \bar{c}_0(x, y, t)$, we then have

$$\partial_z \bar{c}_1(x, y, h, t) - \partial_z \bar{c}_1(x, y, 0, t) = \mathrm{Pe}_c\left[h\partial_t \bar{c}_0 + \nabla \bar{c}_0 \cdot \mathbf{Q}\right] - h\Delta \bar{c}_0.$$

According to the boundary conditions (3.27) and (3.31), we derive a PDE for $\bar{c}_0(x, y, t)$:

$$\mathrm{Pe}_c\left[h\partial_t \bar{c}_0 + \nabla \bar{c}_0 \cdot \mathbf{Q}\right] - h\Delta \bar{c}_0 = E\mathrm{Pe}_c \bar{c}_0 J + \nabla h \cdot \nabla \bar{c}_0 - \mathrm{Pe}_c P_c(\bar{c}_0 - 1)\bar{c}_0.$$

For convenience, we use c in the equations instead of $\bar{c}_0$. Therefore, we have derived a system of PDEs for the dimensionless variables $h(x, y, t)$ and $c(x, y, t)$:

$$\partial_t h + EJ + \nabla \cdot \mathbf{Q} - P_c(c - 1) = 0, \tag{3.35}$$

$$h\partial_t c + \nabla c \cdot \mathbf{Q} = EcJ + \frac{1}{\mathrm{Pe}_c}\nabla \cdot (h\nabla c) - P_c(c - 1)c. \tag{3.36}$$

The evaporative mass flux J is given by

$$J = \frac{1 - \delta\left(S\Delta h + Ah^{-3}\right)}{\bar{K} + h},$$

and the fluid flux $\mathbf{Q}$ across any cross-section of the film is given by

$$\mathbf{Q} = \frac{h^3}{12}\nabla\left(S\Delta h + Ah^{-3} - Gy\right).$$

The nondimensional parameters that arise are defined and given values in the following section and in Table A.1. The dimensional parameters used in those expression are given in Table A.2.

For numerical purposes, we rewrite the model equations (3.35) & (3.36) by introducing the pressure $p(x, y, t)$ as a new dependent variable:

$$\partial_t h + E\frac{1 + \delta p}{\bar{K} + h} + \nabla \cdot \left[-\frac{h^3}{12}\nabla\left(p + Gy\right)\right] - P_c(c - 1) = 0, \tag{3.37}$$

$$p + S\Delta h + Ah^{-3} = 0, \tag{3.38}$$

$$h\partial_t c + \nabla c \cdot \left[-\frac{h^3}{12}\nabla\left(p + Gy\right)\right] = Ec\frac{1 + \delta p}{\bar{K} + h} + \frac{1}{\mathrm{Pe}_c}\nabla \cdot (h\nabla c) - P_c(c - 1)c. \tag{3.39}$$

3.2.2 Permeability of the ocular surface

The ocular surface is believed to be permeable, and the induced osmotic flow helps to arrest tear film thinning and hence ameliorate osmolarity elevation [11]. In addition, the tissue permeability for water is not a constant over the ocular surface; the conjunctiva is normally more permeable than the cornea [25]. King-Smith and coworkers proposed values for the tissue permeability of the ocular surface, that is, 12.0μm/s for the cornea and 55.4μm/s for the conjunctiva [59, 19]. We use these values to determine the dimensionless permeability P_c in the model as follows: we first define the corneal region as a unit circle with the center $\mathbf{X_c} = (0.05, 0.225)$ in the domain shown in Figure 3.1, and the variable permeability at any position $\mathbf{X} = (x, y)$ is then defined as

$$P_c(x, y) = \frac{P_{\text{conj}} - P_{\text{corn}}}{2} \tanh\left(\frac{|\mathbf{X} - \mathbf{X_c}| - 1}{0.05}\right) + \frac{P_{\text{conj}} + P_{\text{corn}}}{2}. \tag{3.40}$$

Here $P_{\text{conj}} = 0.06$ is the dimensionless permeability of conjunctiva , $P_{\text{corn}} = 0.013$ is the dimensionless permeability of cornea, and $|\mathbf{X} - \mathbf{X_c}|$ is the distance between points $\mathbf{X}$ and $\mathbf{X_c}$. Figure 3.2 plots the distribution of the variable permeability on the eye-shaped domain.

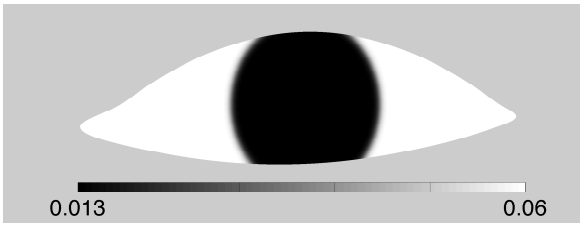

Figure 3.2: Variable permeability distribution over the ocular surface.

3.2.3 Boundary conditions

Along the boundary of the eye-shaped domain (denoted as $\partial\Omega$), we prescribe the constant tear film thickness

$$h|_{\partial\Omega} = h_0. \tag{3.41}$$

We set $h_0 = 13$ in the computation because this choice is in the range of experimental measurement (48 – 66μm or 9.6 – 13.2 nondimensionally) from [37]. In addition, we specify the normal component of the fluid flux,

$$\mathbf{Q} \cdot \mathbf{n}_b = Q_{lg}(s,t) + Q_p(s,t), \tag{3.42}$$

according to the mechanism of [28] for tear supply and drainage, and the tear drainage model of [126], but with simplification regarding blinking. This fluid flux boundary condition mimics some effects of blinking by providing a time-dependent influx through the lacrimal gland and efflux through the puncta. Specifically, the lacrimal gland supply is specified as on at the beginning of a flux cycle, and the punctal drainage follows one time unit later. Both the supply and drainage start to shut off at t = 5. The duration of a complete flux cycle in the model is $\Delta t_{bc} = 10$. In Figure 3.3, we show a sequence of images of the fluid flux boundary condition (3.42) within a flux cycle. At $t = 0$ (Figure 3.3a), there is zero fluid flux on the boundary. At $t = 0.5$, we see the lacrimal gland supply is fully on while the drainage does not yet start in Figure 3.3b; the drainage begins at $t = 1$. In Figure 3.3c, both supply at the lacrimal gland and drainage at the two puncta holes remain fully on. Then, the fluid flux turns off at $t = 5$ and remains zero until the end of a flux cycle (t=10) as shown in Figure 3.3d. The influx and efflux are balanced in each flux cycle. To be specific, we define

$$Q_{lg}(s,t) = f_{lg}(t)\hat{Q}_{ls}(s), \quad Q_p(s,t) = f_p(t)\hat{Q}_p(s) \tag{3.43}$$

in the time-dependent fluid flux BC (3.42). The formulations of $f_{lg}(t), f_p(t), \hat{Q}_{lg}(s)$, and $\hat{Q}_p(s)$ are listed below:

$$f_{lg}(t) = \begin{cases} \frac{1}{2}\left[\cos\left(\frac{\pi}{2}\frac{t-t_{lg,on}}{\Delta t_{lg}} - \frac{\pi}{2}\right) + 1\right], & \text{if } |t - t_{lg,on}| \le \Delta t_{lg}; \\ 1, & \text{if } t_{lg,on} + \Delta t_{lg} \le t \le t_{lg,off} - \Delta t_{lg}; \\ \frac{1}{2}\left[\cos\left(\frac{\pi}{2}\frac{t-t_{lg,off}}{\Delta t_{lg}} + \frac{\pi}{2}\right) + 1\right], & \text{if } |t - t_{lg,off}| \le \Delta t_{lg}; \\ 0, & \text{otherwise.} \end{cases} \tag{3.44}$$

$$f_p(t) = \begin{cases} \frac{1}{2}\left[\cos\left(\frac{\pi}{2}\frac{t-t_{p,on}}{\Delta t_p} - \frac{\pi}{2}\right) + 1\right], & \text{if } |t - t_{p,on}| \le \Delta t_p; \\ 1, & \text{if } t_{p,on} + \Delta t_p \le t \le t_{p,off} - \Delta t_p; \\ \frac{1}{2}\left[\cos\left(\frac{\pi}{2}\frac{t-t_{p,off}}{\Delta t_p} + \frac{\pi}{2}\right) + 1\right], & \text{if } |t - t_{p,off}| \le \Delta t_p; \\ 0, & \text{otherwise.} \end{cases} \tag{3.45}$$

$$\hat{Q}_{lg}(s) = \begin{cases} 0, & \text{if } s < s_{lg,on} - \Delta s_{lg}; \\ -\frac{1}{2}\hat{Q}_{0lg}\left[\cos\left(\frac{\pi}{2}\frac{s-s_{lg,on}}{\Delta s_{lg}} - \frac{\pi}{2}\right) + 1\right], & \text{if } |s - s_{lg,on}| \le \Delta s_{lg}; \\ -\hat{Q}_{0lg}, & \text{if } s_{lg,on} + \Delta s_{lg} \le s \le s_{lg,off} - \Delta s_{lg}; \\ -\frac{1}{2}\hat{Q}_{0lg}\left[\cos\left(\frac{\pi}{2}\frac{s-s_{lg,off}}{\Delta s_{lg}} + \frac{\pi}{2}\right) + 1\right], & \text{if } |s - s_{lg,off}| \le \Delta s_{lg}; \\ 0, & \text{otherwise.} \end{cases} \tag{3.46}$$

$$\hat{Q}_p(s) = \begin{cases} 0, & \text{if } s < s_{p,lo} - \Delta s_p; \\ -\frac{\hat{Q}_{0p}}{2}(1 - p_{out})\left[\cos\left(\pi\frac{s-s_{p,lo}}{\Delta s_p} - \pi\right) - 1\right], & \text{if } |s - s_{p,lo}| \le \Delta s_p; \\ 0, & \text{if } s_{p,lo} + \Delta s_p \le s \le s_{p,up} - \Delta s_p; \\ -\frac{\hat{Q}_{0p}}{2}(p_{out})\left[\cos\left(\pi\frac{s-s_{p,up}}{\Delta s_p} - \pi\right) - 1\right], & \text{if } |s - s_{p,up}| \le \Delta s_p; \\ 0, & \text{otherwise.} \end{cases} \tag{3.47}$$

For the osmolarity $c(x, y, t)$, we consider two boundary conditions in this paper. Case (i) is the Dirichlet boundary condition

$$c|_{\partial\Omega} = 1; \tag{3.48}$$

case (ii) is the homogeneous Neumann boundary condition

$$\nabla c \cdot \mathbf{n}_b|_{\partial\Omega} = 0. \tag{3.49}$$

3.2.4 Initial Condition

The initial condition $h(x, y, 0)$ is specified based on a numerically smoothed version of the function

$$h(x, y, 0) = 1 + (h_0 - 1)e^{-\min(\text{dist}((x,y),\partial\Omega))/x_0}, \tag{3.50}$$

Table 3.1: Parameters appearing in the flux boundary condition.

Parameter	Description	Value
$t_{lg,on}$	On time for lacrimal gland supply	0.2
$t_{lg,off}$	Off time for lacrimal gland supply	5.2
Δt_{lg}	Transition time of lacrimal gland supply	0.2
$t_{p,on}$	On time for punctal drainage	1.05
$t_{p,off}$	Off time for punctal drainage	5.05
Δt_p	Transition time of punctal drainage	0.05
Q_{mT}	Estimated steady supply from lacrimal gland	0.08
$\hat{Q}_{0lg}$	Height of lacrimal gland peak	0.4
$\hat{Q}_{0p}$	Height of punctal drainage peak	4
Δt_{bc}	Flux cycle time	10
$s_{lg,on}$	On-ramp location for lacrimal gland peak	4.2
$s_{lg,off}$	Off-ramp location for lacrimal gland peak	4.6
Δs_{lg}	On-ramp and off-ramp width of lacrimal peak	0.2
p_{out}	Fraction of drainage from upper punctum	0.5
$s_{p,lo}$	Lower punctal drainage peak location	11.16
$s_{p,up}$	Upper punctal drainage peak location	11.76
Δs_p	Punctal drainage peak width	0.05

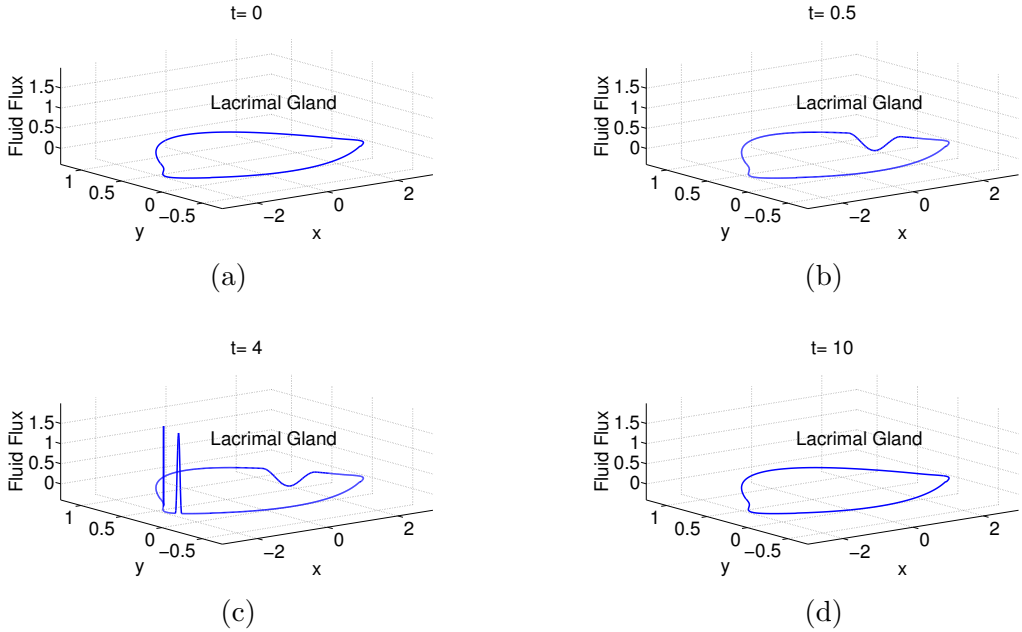

Figure 3.3: Time sequences of fluid flux boundary condition during one flux cycle.

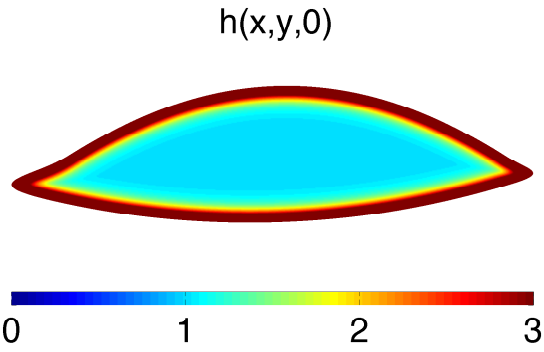

(a) Initial tear film thickness. The upper end of the maroon color indicates tear film thickness $h \geq 3$.

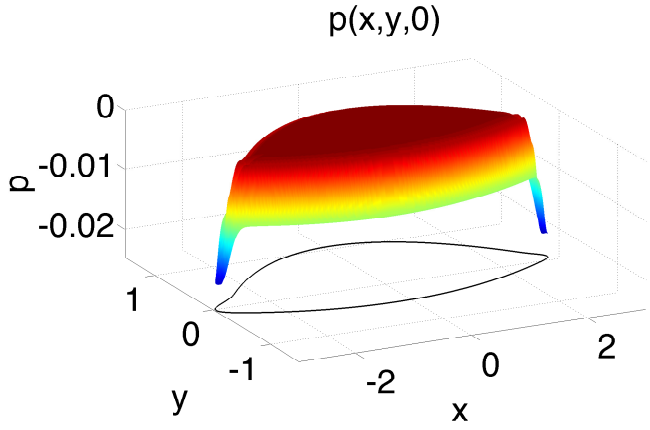

(b) Initial pressure distribution.

Figure 3.4: Smoothed initial conditions for h and p.

where $x_0 = 0.06$ and dist $(\mathbf{X}, \partial\Omega)$ is the distance between a point with position vector $\mathbf{X}$ and a point on the boundary $\partial\Omega$ [72, 73]. It specifies a dimensional initial volume of about 1.805μl. This value is well within the experimental measurements by [80], who found the volume of exposed tear fluid to be $2.23 \pm 2.5\mu$l. The initial pressure $p(x, y, 0)$ is calculated from equation (3.38) accordingly [67]. Figure 3.4 shows the initial thickness h and pressure p that are implemented in the numerical simulations. For the initial osmolarity, we assume the salt-ions are well mixed and of the isosmotic physiological salt concentration (302 Osm/m^3, or 1 dimensionlessly) at the beginning, thereby specifying

$$c(x, y, 0) = 1. \tag{3.51}$$

3.3 Conclusion

In this Chapter, we show detailed formulation of a mathematical model that couples osmolarity dynamics within human tear film on an eye-shaped domain. This model includes the physical effects of evaporation, surface tension, viscosity, ocular surface wettability, osmolarity, osmosis and tear fluid supply and drainage. Results of the model are given in the following chapters. In Chapter 4, we focus on studying the fluid dynamics of tear film; we hope to capture the tear fluid flow over the entire exposed ocular surface . In Chapter 5, the interaction between tear fluid and osmolarity dynamics is investigated by solving the complete model introduced in this Chapter.

Chapter 4

TEAR FILM DYNAMICS WITH EVAPORATION, WETTING AND TIME-DEPENDENT FLUX BOUNDARY CONDITION ON AN EYE-SHAPED DOMAIN

4.1 Introduction

In this chapter, we focus on the tear film part of the model derived in Chapter 3 by ignoring the osmolarity component. That is, we solve for $h(x, y, t)$ and $p(x, y, t)$ from the following model equations:

$$\partial_t h + E\frac{1+\delta p}{\bar{K}+h} + \nabla \cdot \left[-\frac{h^3}{12}\nabla\left(p + Gy\right)\right] = 0, \tag{4.1}$$

$$p + S\Delta h + Ah^{-3} = 0, \tag{4.2}$$

subject to boundary conditions (3.41) & (3.42) and initial conditions shown in Figure 3.4. We investigate how much of the observed *in vivo* tear film dynamics can be recovered using only a flux cycle and by compensating for evaporative water losses with extra influx but no actual blinks. The tear film results show that our model captures the fluid flow around the meniscus and other dynamic features of human tear film that is in agreement with previous models and *in vivo* observations.

We begin by describing the experiment in Section 4.2 and present a brief description of the numerical methods used for the simulation in Section 4.3. Detailed results of simulations and comparison with experiments are discussed in Section 4.4. Conclusion is followed in Section 4.5.

4.2 Experiment

We briefly describe the fluorescence imaging method used for visualizing tear film dynamics [91, 58, 13] here. This established method was used to produce original

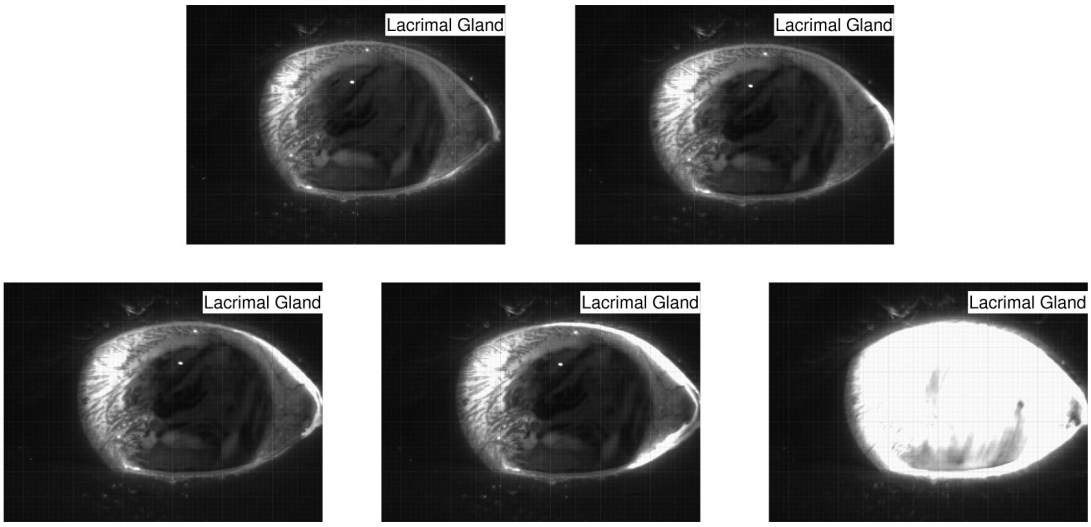

Figure 4.1: Sequence of tear film images of the experiment after a blink. The first image is 5.5s after a blink; the next three images are, respectively, 9.5s, 10.17s and 10.83s after that blink. The final image is after a blink that began less than a second after the sequence shown. Gravity is oriented downward in the panels.

images in this work. Video recordings were made from subjects, including normal and dry eyes, for a 60 second period after instillation of 1μl of 5% (sodium) fluorescein. Subjects were instructed to blink about 1 second after the start of the recording and try to hold their eyes open for the remainder of the recording. The subjects' eyes were illuminated with blue light and a blocking interference filter was used to reduce the response to reflected illumination light. This allowed a better detection of the fluorescence of the tear film. The horizontal illumination width was 15 mm, thus including the cornea and part of the conjunctiva. The research protocol was approved by an Institutional Review Board in accordance with the Declaration of Helsinki. Informed consent was obtained from each subject at study enrollment.

In Figure 4.1, we show some images from the video recording of one subject. The first frame shows the tear film at 5.5 seconds after a blink; this image is representative of the first 9 s after the blink. There is a region of slightly brighter tear film around the lid margins; this is the meniscus. At 5.5 seconds after the blink, within the meniscus and just above the outer canthus (right side), part of the meniscus is slighlty brighter;

it is labeled "lacrimal gland" to indicate the location of input of tear fluid to the tear film from the lacrimal gland. This part of the tear fluid brightens because fresh tear, comprising primarily water, is entering the exposed tear film due to reflex tearing. At 9.5s (right panel, top row), the bright region has grown, showing where fresh tears have penetrated the tear film. The next two panels (10.17s and 10.83s) show the bright region growing around the outer canthus and along both the upper and lower menisci. The bright region is indicating where fresh tear fluid has entered the tear film and lowered the concentration of fluorescein [123, 91, 13]. In the final panel, the subject had blinked in less than 1 s after the last panel, and fresh tear fluid has mixed with the existing tear fluid, diluted it, and made the entire exposed tear film glow. This supply of fluid without blinking is often called reflex tearing (e.g., [60, 71]). Li *et al.* [67] includes a movie in the supplementary material showing the complete observation.

There is some variation in the experimental results. For example, in [41], tear fluid traveled faster along the lower eyelid while our experiment shows the opposite. Maurice [81] didn't report the fluid velocity in the menisci. The relative amount of flow along the upper or lower meniscus under general conditions remains an open question.

In the Results section 4.4, we will compare our thin film model with the visualization of tear fluid entering the tear film.

4.3 Numerical Methods

We briefly describe the numerical methods used to solve the model system (Eq. (4.1) & (4.2)) here. The detailed discussion about the numerical methods is found in Chapter 6 and in Maki's dissertation [70]. The domain is discretized using a composite overlapping grid, which is a collection of logically rectangular curvilinear component grids that overlap where they meet, and cover the whole domain. We use four boundary-fitting components grids to approximate the boundary, and a background Cartesian grid to cover the rest of the domain. We produce the boundary-fitting grids by extending the normals to the boundary. However, owing to the large curvature at the two canthi, the distance we can extend in the normal direction is limited, otherwise the

normal lines would intersect inside the boundary-fitting grids. In order to offer enough resolution for the meniscus, we increase the number of grids for the background Cartesian grid. Solutions on the different grids are coupled by interpolation. The domain and the associated grids [72, 73, 67] are created with the grid generation capabilities of the OVERTURE computational framework [23, 42] (http://www.overtureframework.org. Primary developer and contact: W. D. Henshaw, henshw@rpi.edu). The computational grid used to generate tear film results in Section 4.4 is shown in Figure 4.2.

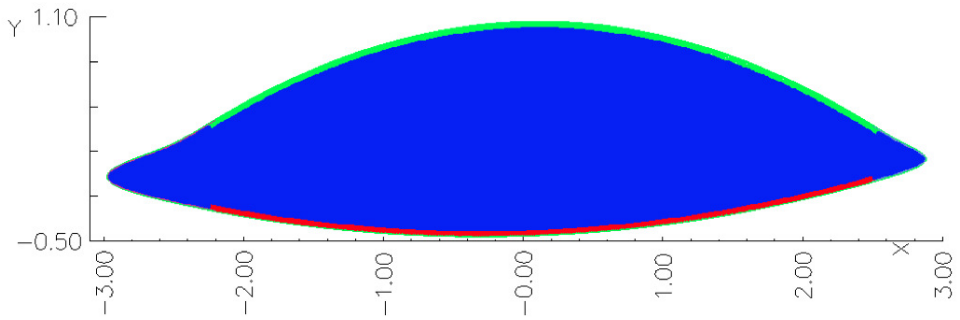

Figure 4.2: Computational grid on the eye-shaped domain.

We solve the system (4.1) & (4.2) by the method of lines. The spatial derivatives are approximated using the second-order accurate finite difference methods for curvilinear and Cartesian grids from OVERTURE, which leads to a system of index-1 differential algebraic equations (DAE). The DAE system is advanced using a variable step size backward differentiation formula (BDF) with fixed leading coefficient that was added to Overture [17, 72, 73]. Finally, we solve the resulting nonlinear system using Newton's method.

The method achieves good accuracy on test problems with exact solutions using this domain and gridding approach [70, 73]. We provide additional numerical evidence in Section 4.4 verifying that the method also performs well on the current problem.

4.4 Results

4.4.1 Tear Film Dynamics

In this section, we present and compare computed results of Equations (4.1) & (4.2) for various parameter settings: (i) $E = 0$ & $G = 0$, (ii) $E \neq 0$ & $G = 0$, and (iii) $E \neq 0$ & $G \neq 0$. Recall that E helps characterize the evaporation rate and G characterizes the effect of gravity. We switch these effects on and off in order to study the individual effects of time-dependent flux boundary condition (3.42), evaporation and their combined effects on tear film dynamics. We shall later modify the lacrimal gland supply function $Q_{lg}(s,t)$ so that the net amount of fluid provided by the flux boundary condition compensates for the evaporative loss during a flux cycle.

We first show results for $E = G = 0$. This case was studied by Maki *et al.* [73] for a *time-independent* flux BC and with no van der Waals forces. Here the flux BCs (3.42) are time dependent and the substrate under the film is wettable. Computed thickness contours are shown in Figure 4.3. As observed previously in many tear film papers, the relatively thick film at the boundary induces positive curvature, which lowers the pressure and sucks fluid into the meniscus; near the meniscus a local minimum forms that is called the "black line" in the eye literature. The name comes from the dark band that appears near the bright meniscus when using fluorescence imaging. (In our figures, it is colored dark blue from the low end of the color bar.) The mechanism was illustrated by McDonald and Brubaker [82] using milk and a paper clip, and has been recovered by all of the papers that have the ends modeling the lids. In the two-dimensional domain, the additional features that appear are the canthi, which induce a second direction of curvature, creating an even lower pressure that attracts fluid toward themselves. The especially thin black line creates a boundary that separates the interior of the tear film from the meniscus; this occurs because h is small and the flux $\mathbf{Q}$ is proportional to h^3. The interior is sometimes referred to a "perched" tear film [83]. The redistribution of fluid due to surface tension also causes a small ridge to form on the interior side of the black line. The thickness of the film in the interior is roughly constant. In the meniscus, the tear film thickens near the region of influx

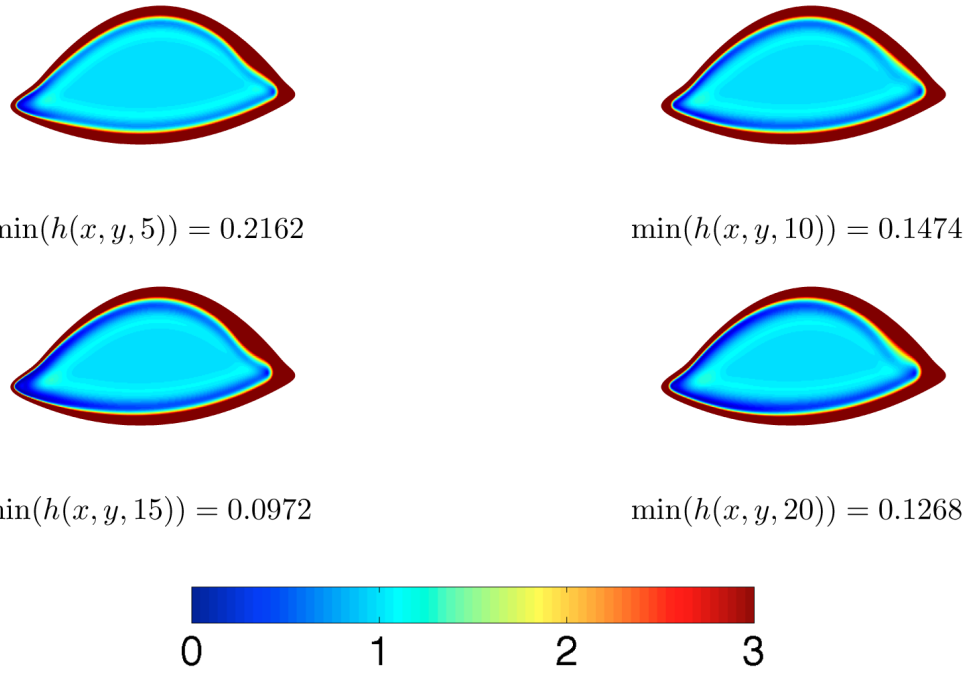

Figure 4.3: Contours of tear film thickness with $E = 0$ and $G = 0$. The maroon band around the boundary shows thickness greater than or equal to 3.

from lacrimal gland (right side, above temporal canthus), and narrows in the region of efflux by the puncta (left side, nasal canthus). The new fluid is unable to penetrate into the interior under these conditions. More extreme influx conditions [126], such as the reflex tearing that arises when cutting an onion or from crying, may overcome the barrier created by the black line and cause fluid to reach the interior without blinking [71].

Contour plots for the pressure corresponding to $E = G = 0$ are shown in Figure 4.4 at two different times. The highest pressures occur in the interior, particularly under the ridge near the black line, and near the input from the lacrimal gland. The meniscus pressure is always lower than the interior in this computation, and this lower pressure pulls fluid into the meniscus. But within the meniscus, there is a pressure gradient that drives flow away from the input region of the lacrimal gland and ultimately toward the lowest-pressure region by the puncta and nasal canthus. The plots in Figure 4.4 illustrate the mechanisms for the flow that forms the black line, and for

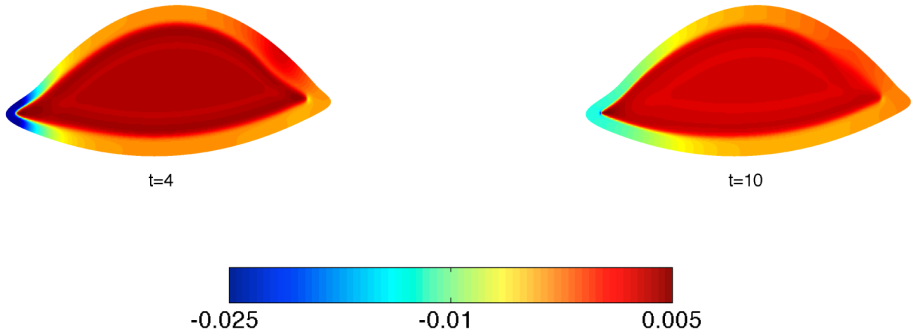

Figure 4.4: Pressure distribution for $E = G = 0$ with time-dependent flux boundary conditions and a wettable substrate.

the flow around the meniscus that we refer to as hydraulic connectivity. We show the pressure at $t = 4$ to illustrate how the time-dependent flux BC influences the pressure distribution when both lacrimal gland influx and puncta efflux are fully functioning; the latter contributes to the very low pressure seen in the neighborhood of the nasal canthus. Then we plot p at the end of the first flux cycle ($t = 10$) when the flux BC is zero all around the boundary. The pressures near the temporal and nasal canthi are less extreme at this time because of the surface tension driven relaxation that occurs in the meniscus when the boundary fluxes are zero. We can also plot the direction and magnitude of the volumetric flux inside the film; representation results are shown in the next case. We discuss the flux in general in the cases with evaporation, which we turn to next.

Figure 4.5 shows the evolution of the tear film thickness with evaporation. The first column shows results for the case $E \neq 0$ & $G = 0$, and the second column for $E \neq 0$ & $G \neq 0$. We first focus on $G = 0$. The presence of the meniscus again creates a pressure difference between the interior and the meniscus, which drives the tear fluid from the interior towards the boundary, resulting in the black line separating the two. The lower pressure in the meniscus can be clearly seen in the pressure distribution plots; the plots for this case are quite similar to those in Figure 4.4, but the specific plots for these parameters are shown in Figure 4.6. We find the global minimum in the

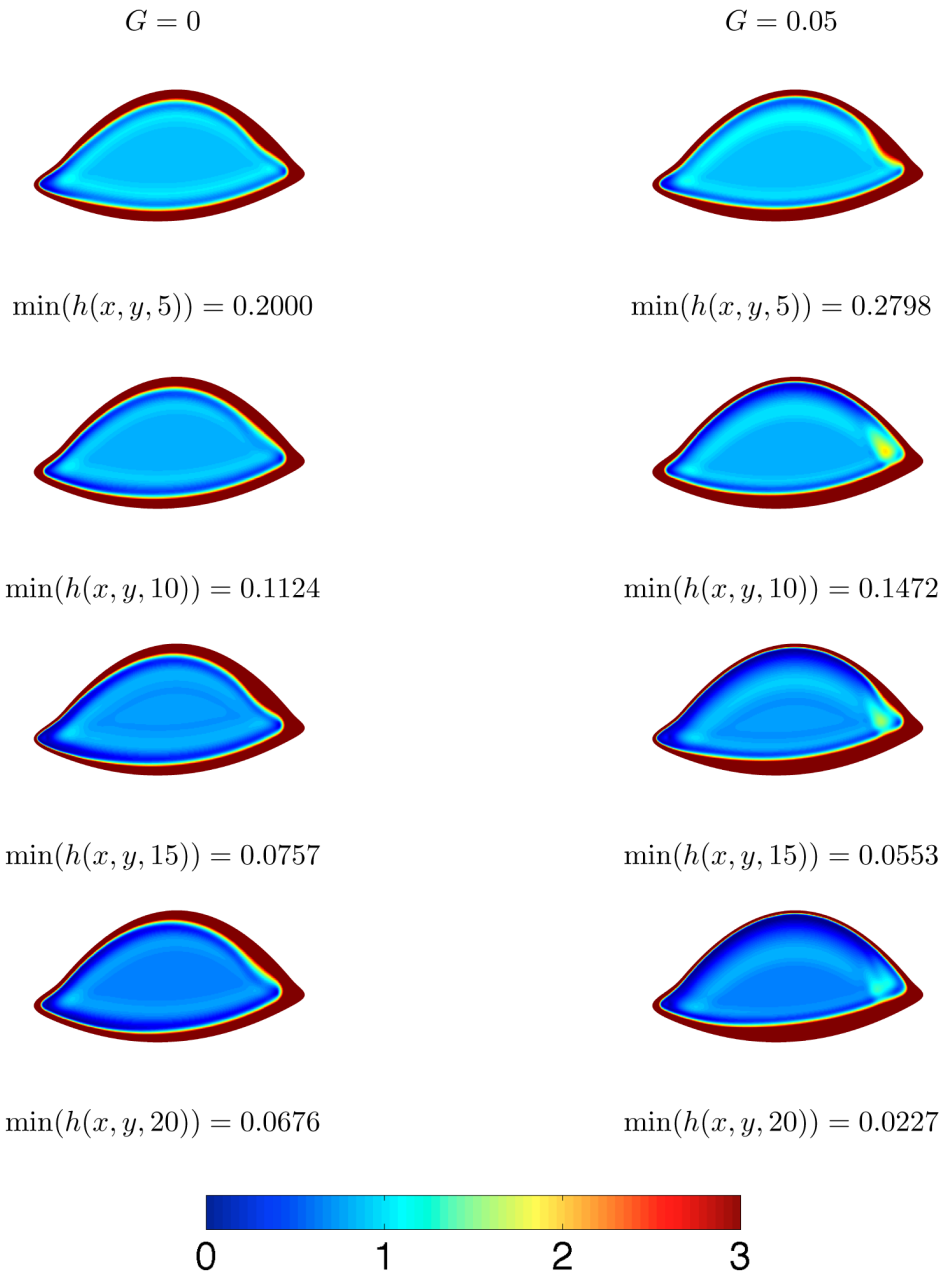

Figure 4.5: Contour plots of the tear film thickness without gravity (left column) and with gravity (right column). The maroon band around the boundary shows thickness greater than or equal to 3.

thickness occurring near the nasal canthus, in a manner similar to the last case. With evaporation, however, the tear film thins in the interior throughout the computation which is visualized by the continual darkening of the interior. As seen in Figure 4.5, the

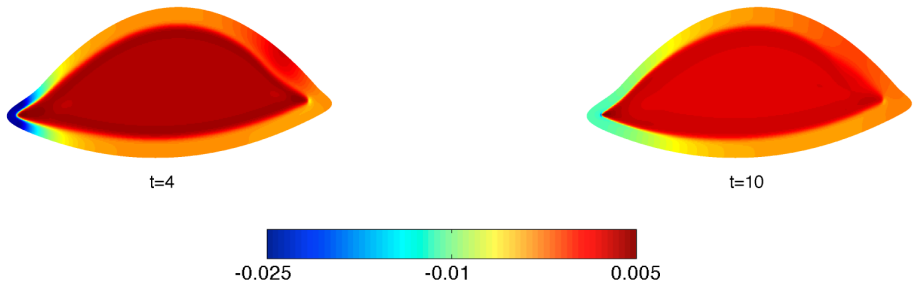

Figure 4.6: Pressure distribution for $E \neq 0$ and $G = 0$.

minimum thickness is smaller than that in Figure 4.3. Our model is consistent with the expected contribution of evaporation to tear film thinning of the interior region between blinks and with the experimental studies of Kimball *et al.* [52], Nichols *et al.* [91] and others. The capillary-driven tangential flow only explains the thinning of tear film near the meniscus, i.e., the formation of black line; it has little to do with the thinning of tear film in the interior region [83, 56].

The flux boundary condition (3.42) imposed on our model enforces time-dependent influx from the lacrimal gland and efflux though the two punctal holes on the nasal side. The influx pumps fluid into the meniscus above the the temporal canthus, while the efflux drains fluid out near the nasal canthus. We plot the direction field of the flux $\mathbf{Q}$ over contours of its magnitude in Figure 4.7. The lengths of the arrows are normalized to unity, thus showing the directions only, and we use the shading to indicate the magnitude of the flux vector: the darker the background, the smaller the flux. In particular white indicates a flux greater than 10^{-2}; dark gray is less than 10^{-3}. Finally, there are far fewer arrows than the computational grids for clarity. The arrows in Figure 4.7 illustrate the effect of the boundary flux at $t = 4$. The computed flux is consistent with the maroon band becoming wider near the lacrimal gland with increasing time and narrower near the nasal canthus in Figure 4.5. Additionally, the flux boundary condition changes the curvature of the meniscus causing the pressure gradient that drives the fluid flow in the meniscus (Figure 4.6).

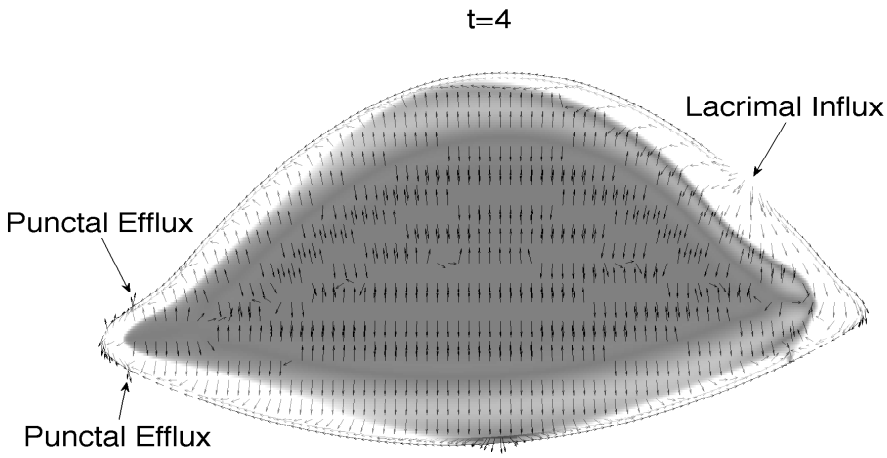

Figure 4.7: The flux direction field plotted over the contours of the norm of the flux at $t = 4$ with $E \neq 0$ and $G = 0$. (Far fewer arrows than the computational grid points are shown for clarity. All the arrows in this plot start at different locations.)

The second plot of Figure 4.6 is the pressure at the end of the first flux cycle ($t = 10$). For most of the interior region, the pressure gradient is approximately zero, and there is little motion there; correspondingly, Figure 4.8 for the flux at $t = 10$ is basically dark in the interior, i.e., with $||\mathbf{Q}|| < 10^{-2}$. Relatively fast ($||\mathbf{Q}|| \geq 10^{-2}$) fluid movement occurs near the boundary in the meniscus, splitting at the lacrimal gland input and traveling around the menisci toward the puncta and nasal canthus. Thus, Figure 4.8 illustrates the hydraulic connectivity observed by Maurice [81], Harrison *et al.* [41] and our experiment described in Section 4.2, and as computed in some cases by Maki *et al.* [73]

When the flux through the boundary is off (no flux anywhere), hydraulic connectivity makes the fluid move towards the nasal canthus, makes the meniscus wider, and lowers the pressure difference between the canthi. However, when the punctal drainage is on for the next flux cycle, the meniscus near the nasal canthus gets narrower again. In the model, we assume a flux cycle to be 10 time units. The time-dependent flux boundary condition (3.42) is specified as non-zero for the first 5 time units of each flux

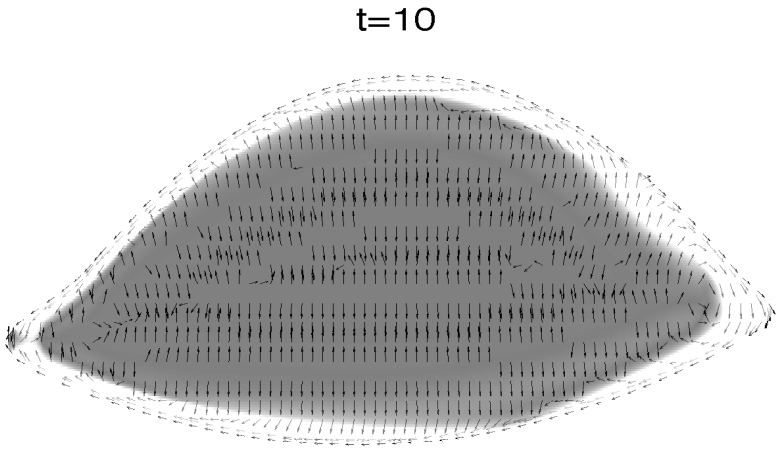

Figure 4.8: The flux direction field at the end of first flux cycle. $E \neq 0$ and $G = 0$. (Far fewer arrows than the computational grids are shown for clarity. All the arrows in this plot start at different locations.)

cycle and zero for $5 < t < 10$. The on-off transition time is very short (c.f. Table 3.1). Once the boundary flux turns off, tear fluid starts to collect at the nasal canthus due to the low pressure caused by the relatively large curvature of the film surface there. Thus, we see the maroon band near the nasal canthus is wider at the end of each flux cycle in Figure 4.5 ($t = 10$ and $t = 20$). The pressure at the nasal canthus starts to increase and this prevents a steep pressure gradient that would eventually cause the simulation with time independent, nonzero boundary fluxes to stop [73]. In general, as Maki *et al.* [73] speculated in their paper, the time-dependent boundary condition helps avoid large interior pressure gradients by having the punctal drainage active for a short time.

We now turn to the the case with gravity active, $E \neq 0$ and $G \neq 0$. Gravity redistributes the tear film from the top to the bottom of the domain and may be another important effect on tear film dynamics, e.g., if the tear film is thick enough [12, 71]. The right column of Figure 4.5 illustrates the tear film thickness with $G = 0.05$. Similar to prior results, the black line develops rapidly and is persistent. However, due to the gravitational effect, the maroon band representing the lower meniscus widens

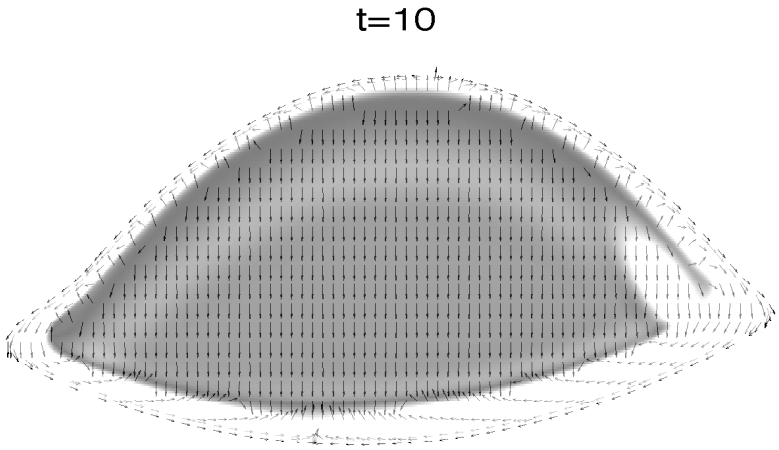

Figure 4.9: The flux direction field at the end of first flux cycle with $E \neq 0$ and $G = 0.05$. (Far fewer arrows than the computational grids are shown for clarity. All the arrows in this plot start at different locations.)

significantly in this computation; this means more tear fluid is collected at the bottom. Tracking the same time sequence of plots with or without gravity, we see that a bulge of new tear fluid supplied by the lacrimal gland is being driven downwards. It penetrates through the black line and then exits the interior to the lower meniscus, but only near the temporal canthus. The direction of the fluid motion at the end of first cycle ($t = 10$) can be seen in Figure 4.9. All the arrows in the inner dark region are pointing toward the lower eyelid for that slow flow. The light area intruding inside the dark region shows the relatively fast movement of the bulge of fluid. The pressure plots at $t = 4$ and 10 are shown as Figure 4.10. Other than a slight pressure gradient from top to bottom in these figures, the plots are similar to the other pressure plots shown.

The existence of black line once formed is persistent for all the cases in Figure 4.3 and Figure 4.5. Even though, with the presence of gravity, the influx bulge breaks through the black line near the lacrimal gland and temporal canthus, it does not move into the interior and does not help to ameliorate the thinning process of the interior region.

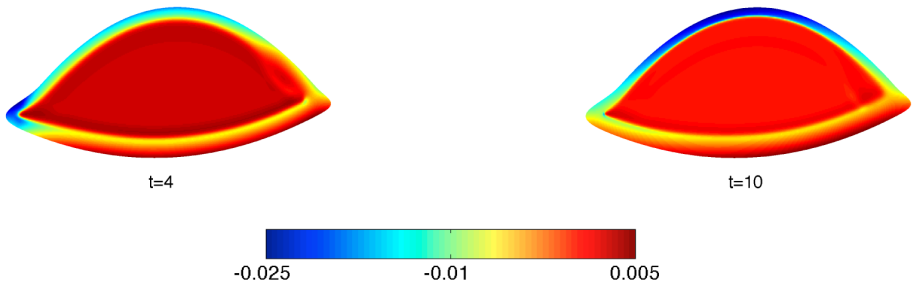

Figure 4.10: Pressure distribution for $E \neq 0$ and $G \neq 0$.

4.4.2 Volume Conservation

Now that we have visualized some results for the model, we now turn to some integrated (global) quantities to illustrate that the method is working consistently. The accuracy of the numerical method has been tested by Maki *et al.* [73] by formulating a test problem with known exact solution on a domain comprising a rectangle with a circular hole cut out. Refinement of the grids yielded convincing numerical evidence of a second order convergence rate in the space variables, consistent with theoretical expectation. In addition, they conducted tests on the eye-shaped domain and achieved good accuracy as well. In both cases, mass conservation was a reasonably good indicator of the error. To give an indication that the numerics also work well for this problem, we verify conservation of mass, or in our case volume since the density is constant. The volume of the tear film at all time equals the initial volume minus the amount of evaporation loss and the amount of the net flux from the boundary condition:

$$V(t) = V(0) - e(t) - F(t), \tag{4.3}$$

where $e(t)$ and $F(t)$ are the volume of tear film that evaporates away and the net flux through the boundary, respectively. Expressions for these can be found by integrating (4.1) with respect to space and time:

$$V(t) - V(0) + \underbrace{E \int_0^t \int_\Omega J dA d\tau}_{e(t)} + \underbrace{\int_0^t \int_{\partial\Omega} \mathbf{Q} \cdot \mathbf{n}_b ds d\tau}_{F(t)} = 0. \tag{4.4}$$

Here Ω is the (eye-shaped) domain of the computation, and the integration in space is over this domain. To verify if the numerical results conserve the fluid volume as stated in equation (4.3), we plot $V(t)$ and $V(0) - e(t) - F(t)$ for various cases.

Time	$Err(t)$	Percentage of $V(0)$
1	0.0181	0.1253%
5	0.0353	0.2442%
10	0.0456	0.3159%
20	0.0582	0.4030%

Table 4.1: No flux boundary condition and no evaporation.

First, we neglect evaporation and use a no-flux boundary condition, i.e., $e(t) = F(t) = 0$. In this case, the difference between $V(t)$ and $V(0)$ increase with time, but remains small. The error in volume conservation is defined as $Err(t) = |V(0) - V(t)|$ and is listed in Table 4.1. The error in volume conservation remains well below 1% for all the times considered.

Second, we check volume conservation for those cases for which we imposed the time-dependent flux boundary condition (3.42) with or without evaporation. The results are plotted in Figure 4.11. The error in the volume conservation at the end of the first flux cycle ($t = 10$) is 0.0585 for $E = 0$, and 0.0574 for $E \neq 0$. These represent an error in volume conservation of less than 1%. Overall, the method appears to work well for the model with evaporation and time-dependent flux boundary condition.

4.4.3 Recovering the Thinning Rate

We obtain the non-dimensional evaporation rate theoretically by differentiating $e(t)$, the volume of tear film that evaporates. Equation (4.4) yields

$$\frac{d}{dt}e(t) = E \int_{\Omega} J(x, y, t) dA.$$

Figure 4.12 shows the evaporation rates vs. time for various cases. The evaporation rate is nearly constant for the first 20 time units. We denote the constant as $Q_e \approx 0.078$

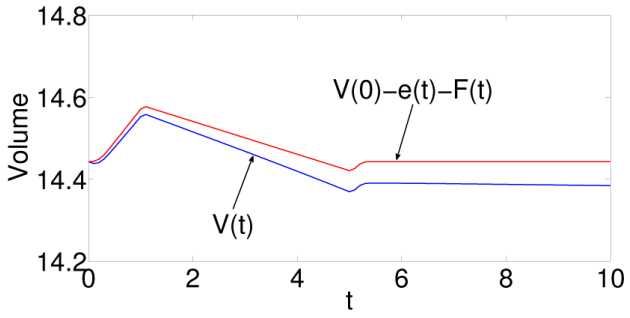

(a) without evaporation

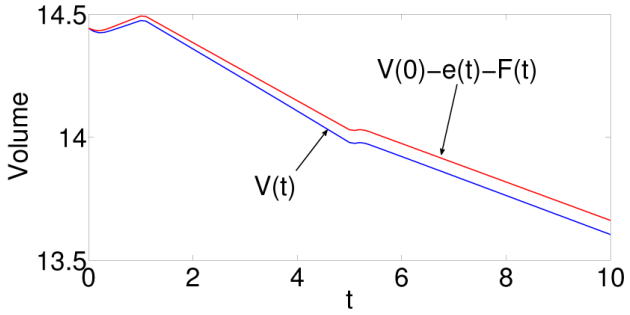

(b) with evaporation

Figure 4.11: Results for the time-dependent flux boundary condition.

(notice that the scale of the coordinate of Figure 4.12 ranges from only 0.077 to 0.0784). Dimensionally, our model predicts the evaporation rate to be 0.58μl/min.

The model recovers the tear film thinning rate that we used to set the evaporation parameters, providing a consistency check on the computations. Nichols *et al.* [92] have found that the mean rate of thinning of the pre-corneal tear film is $3.79 \pm 4.20\mu$m/min. In our model, the area of the eye-shaped domain is about 5.934, i.e. 148.34mm^2 dimensionally. If the calculated evaporation rate is divided by area of the domain, we obtain an average thinning rate of the tear film of 3.91μm/min. That matches our assumed average thinning rate, 4μm/min.

4.4.4 Compensation of Evaporation Loss

For the previous results, the influx and efflux from the time-dependent flux boundary condition (3.42) are balanced over a flux cycle. However, this may not be

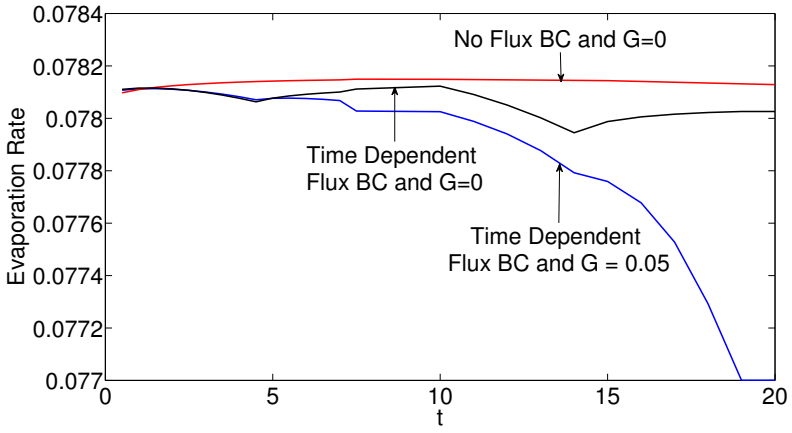

Figure 4.12: Evaporation rate $\frac{d}{dt}e(t)$ of various cases.

what happens in the eye. New tear fluid is supplied from the lacrimal gland to offset tear film loss, and then tear film is recovered to its initial state from evaporation and any redistribution due to surface tension and gravity after each blink. Hence, we attempt to modify the flux boundary condition to compensate for the evaporation loss. To the original balanced flux boundary condition, we add $\tilde{Q}_{lg}(s)$ to provide additional time-independent tear supply through the lacrimal gland at a rate of Q_e, the same as the model predicted evaporation rate, as formulated in Equation (4.5):

$$\mathbf{Q} \cdot \mathbf{n}_b = Q_{lg}(s,t) + Q_p(s,t) + \tilde{Q}_{lg}(s). \tag{4.5}$$

Here $Q_{lg}(s,t)$ and $Q_p(s,t)$ are given by Equation (3.43)–(3.47), and $\tilde{Q}_{lg}(s)$ is formulated as

$$\tilde{Q}_{lg}(s) = \begin{cases} 0, & \text{if } s < s_{lg,on} - \Delta s_{lg}; \\ -\frac{1}{2}\tilde{Q}_{0lg}\left[\cos\left(\frac{\pi}{2}\frac{s-s_{lg,on}}{\Delta s_{lg}} - \frac{\pi}{2}\right) + 1\right], & \text{if } |s - s_{lg,on}| \le \Delta s_{lg}; \\ -\tilde{Q}_{0lg}, & \text{if } s_{lg,on} + \Delta s_{lg} \le s \le s_{lg,off} - \Delta s_{lg}; \\ -\frac{1}{2}\tilde{Q}_{0lg}\left[\cos\left(\frac{\pi}{2}\frac{s-s_{lg,off}}{\Delta s_{lg}} + \frac{\pi}{2}\right) + 1\right], & \text{if } |s - s_{lg,off}| \le \Delta s_{lg}; \\ 0, & \text{otherwise}, \end{cases} \tag{4.6}$$

with

$$\tilde{Q}_{0lg} = \frac{Q_e}{s_{lg,off} - s_{lg,on}}.$$

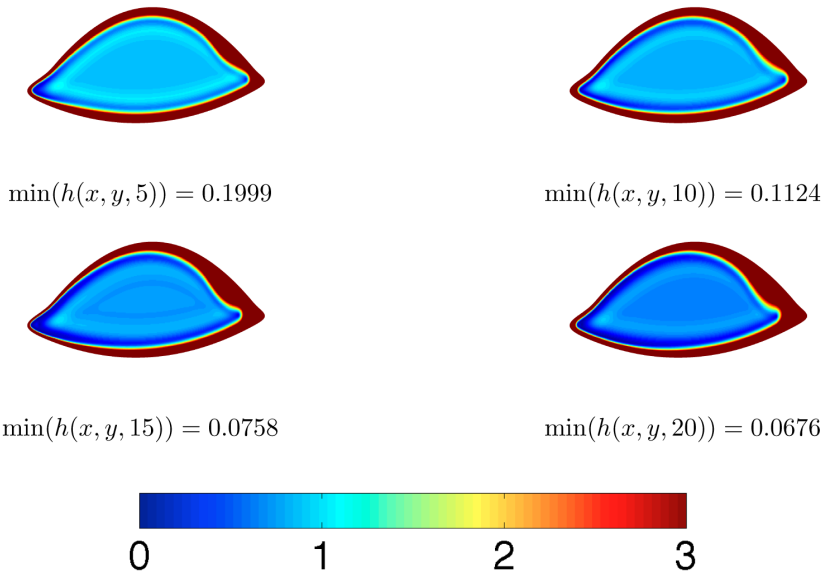

Figure 4.13: Contours of tear film thickness with flux compensating the evaporation loss and $G = 0$.

The simulation with flux boundary condition specified as Equation (4.5) is useful for understanding tear film dynamics. We make an attempt to understand the natural tear film dynamics by adjusting the conditions in the computations. In Figure 4.13 (cf. Video 3), similar patterns to the cases with a balanced flux boundary condition are observed in the tear film thickness. A black line emerges early in time near the meniscus and persists throughout the flux cycles. The tear film in the interior keeps thinning as a result of evaporation. More fluid is collected in the meniscus, especially near the lacrimal gland, because of the influx. However, the larger amount of fluid there still can not penetrate past the black line into the interior [83]. We can not fully restore the tear film to close to its initial uniformly thick distribution in the interior by merely providing more fluid through the lacrimal gland. The blink, with its attendant lid motion, is indispensable to evenly spread the new tear fluid collected in the meniscus into the inner region separated by the black line.

4.4.5 Comparison with Experiment

4.4.5.1 Evaporation

It is important to put our computed evaporation rate in context with measured values over the last few decades for comparison. A number of researchers, as reviewed by Tomlinson *et al.* [113], have measured the evaporation rate with both direct fluid-capture techniques (that measures the fluid loss from the ocular surface) and indirect interferometric technique (that measures the tear film thinning). Results of the direct mass measurements were reported in different units, such as $g/\text{cm}^2/\text{sec}$ and μl/min. In order to compare all these results, Tomlinson *et al.* [113] converted the different units by assuming the density of tear fluid to be that of water (10^3kg/m^3) and the area of the ocular surface to be 167mm^2. The evaporation rates reported by Nichols et al. [92] and Tomlinson et al. [113] have a discrepancy when they are converted to the same units. Kimball et al. [52] speculate that the origin of the difference is that most of the measurements reviewed by Tomlinson et al. [113] were conducted using a preocular chambers. The air flow over the tear film surface is restricted by the chambers, which retards evaporation. The evaporative parameter of the model is estimated based on the assumption of room temperature and free air conditions. The evaporation rate (0.58μl/min) predicted by our model agrees well with that measured by Nichols *et al.* [92] using interferometric technique in a free air condition, and close to the results of Liu *et al.* [68] ($0.40 \pm 0.14\mu$l/min), which was measured using the ventilated-chamber method, even though it is about 4 times larger than the average evaporation rate of those reported from direct measures of fluid mass loss [113].

4.4.5.2 Hydraulic Connectivity

In Figure 4.1, we showed experimental results from an interblink where reflex tearing caused new tear fluid to enter the exposed tear film and flow along the menisci. From that same sequence we show a different time, and compare it with our computed results. Figure 4.14 (cf. the supplementary videos in Li *et al.* [67]) shows this comparison at one time, and reveals that our model captures some of the details of the

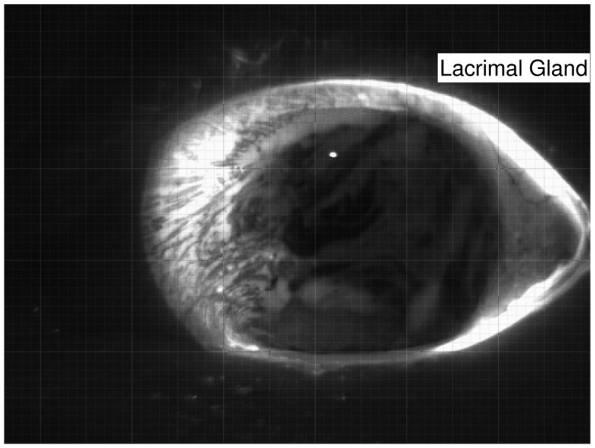

(a) An image from the experiment at 10.6s post blink.

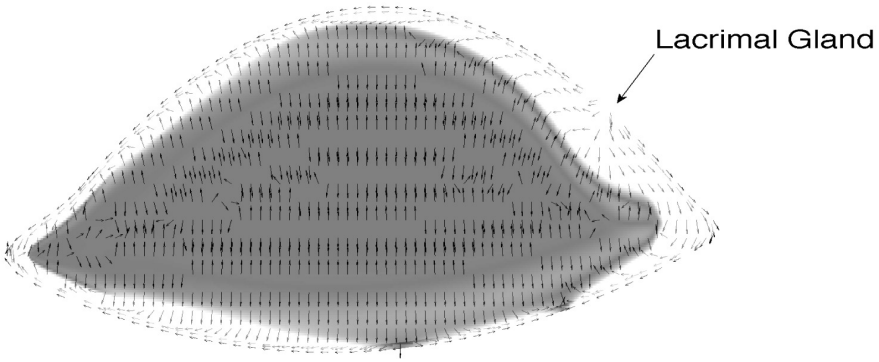

(b) The flux field at $t = 6$ with flux boundary condition compensating the evaporation loss and $G = 0$. (Far fewer arrows than the computational grids are shown for clarity.)

Figure 4.14: Comparison with experiment.

development of hydraulic connectivity correctly. In Figure 4.14b, the arrows indicate the direction of the fluid flow and shading represents the magnitude of the flux as before. Along the upper eyelid, all the arrows are pointing towards the nasal side, and the fluid moves relatively fast. Along the lower eyelid, near the lacrimal gland, the arrows in the light background push the dark region towards the nasal side, which

means the new tear provided by the boundary condition is pushing its way towards the nasal canthus. These trends agree with the frame shown in Figure 4.14a. More detailed comparison can be problematic, however; the volume of the exposed tear film and the volume flux of fluid into it are unknown and difficult to measure.

Our model provides a global prediction about the fluid motion in the eye-shaped domain: all the fluid in the meniscus is traveling towards the nasal canthus. The motion of the dimmed part of the fluid in the experimental image is yet to be measured by any experiments to our knowledge.

4.5 Conclusion

We present a tear film dynamics model on an eye-shaped domain that includes capillarity, gravity, evaporation, ocular surface wettability and time-dependent flux boundary conditions. We significantly extended existing tear film models, providing new insights about tear film dynamics. The inclusion of ocular surface wettability in the model prevents the tear film from reaching zero thickness in the computations, but includes break up as reaching a small nonzero equilibrium thickness, which enables us to conduct numerical simulations for longer times. Our model also captures new details about tear flows in the meniscus, which is beyond the reach of one-dimensional models. We also described experiments using fluorescein that visualized tear film thickness changes, and indirectly, the supply of fresh tear fluid and where the more diluted fluid moves.

The time-dependent flux boundary condition that captures some effects of blinks is formulated based on eye researchers' descriptions [28] and other studies about the tear supply and drainage mechanisms [81, 41]. We began by balancing the influx and efflux through the lacrimal gland and puncta in the boundary condition. The model captures some key physics of the tear film dynamics observed by ocular scientists, such as the emergence of black line, evaporation, and hydraulic connectivity. Then, we modified the lacrimal supply to compensate the evaporation loss in an attempt to restore the tear film structure to its initial thick state in the interior. In the model, tear

fluid supplied from the the lacrimal gland is unable to relieve the evaporation thinning in the interior region with the presence of black line. A blink is well necessary to evenly spread the new tear fluid.

Evaporation is well captured by our model for comparison with well-controlled laboratory experiments. The result yielded by the model is comparable to the measurements conducted with the ventilated-chamber method or in the free air [68, 52], though that rate is larger than the average evaporation rate measured using preocular chambers [113].

Our results also reveal that the hydraulic connectivity is largely controlled by the pressure gradient created by the flux though the lacrimal gland and puncta. The hydraulic connectivity is also aided by the shape of the lid margin, which causes low pressure regions to form and draw fluid toward the canthi. The model correctly captures the overall trend that tear fluid flows towards the nasal canthus along the upper and lower eyelids from the temporal canthus as observed *in vivo* by various researchers. However, due to the lack of experimental information about the flux through the lacrimal gland and flow in the meniscus, we are unable to make quantitative comparisons about the hydraulic connectivity with experimental results.

Chapter 5

COMPUTED TEAR FILM AND OSMOLARITY DYNAMICS ON AN EYE-SHAPED DOMAIN

5.1 Introduction

Incorporating osmolarity dynamics into the existing tear film model is of interest. Osmolarity is essentially the salt ion concentration in the tear film. It is hypothesized to cause the dry eye symptoms such as irritation and redness [7]. However, the measurement of osmolarity is nearly always limited to the temporal canthus (e.g., Lemp *et al.* [63]). Measurements of the osmolarity in the meniscus provide little direct information for the interior regions, though the variation measured near the outer canthus is thought to be helpful in diagnosing dry eye. Therefore, theoretical studies of the osmolarity in an eye-shaped domain may provide insight about the osmolarity distribution over the ocular surface.

In this chapter, we compute the complete model equations (3.37) – (3.39) that combine tear film flow, evaporation, osmolarity and osmosis on a 2D eye-shaped domain. To our knowledge, this is the first such model that incorporates the osmolarity dynamics in a 2D tear film model. Our computational results predict the tear film thickness and osmolarity dynamics simultaneously, revealing the interaction and correlation between tear fluid and osmolarity. Most of all, our model adds significant new results about the distribution of osmolarity over the exposed ocular surface. We believe that these results will impact the understanding of osmolarity dynamics in the tear film as well as the measurement of this important quantity.

We present results for the tear film thickness $h(x, y, t)$ and the osmolarity $c(x, y, t)$ on the 2D eye-shaped domain (Figure 3.1) from numerically solving the model system Eq. (3.37)–(3.39) formulated in Chapter 3. We vary the water permeability

P_c and the thinning rate (evaporation) that sets the non-equilibrium parameter $\bar{K}$ in order to study their influence on the dynamics of tear film fluid and osmolarity. We also explore two types of boundary condition for the osmolarity $c(x, y, t)$: (i) Dirichlet, given by (3.48), and (ii) homogeneous Neumann, given by (3.49).

5.2 Numerical Methods

We solve the equations (3.37)–(3.39) on the eye-shaped geometry (Figure 3.1) using the Overture computational framework (http://www.overtureframework.org. Primary developer and contact: W. D. Henshaw, henshw@rpi.edu), which is a collection of C++ libraries for solving PDEs on complex domains [23, 42]. The corresponding boundary conditions must be applied: (3.41), (3.42) and one of (3.48) or (3.49). Note that the flux condition (3.42) is readily converted into a Neumann condition on p [43]. The initial conditions must be applied as well, using smoothed versions of (3.50) and (3.38), as well as (3.51).

5.2.1 Computational Grid

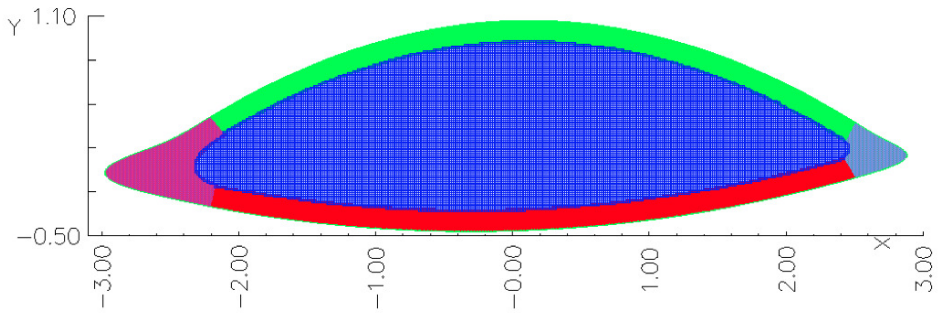

Figure 5.1: Improved computational grid on the eye-shaped domain.

The tear film is relatively thin and flat in most of the interior of the exposed ocular surface; the thickness increases rapidly near the eyelids, forming relatively steep

menisci around the boundary of the corresponding computational domain. In order to solve the tear film model efficiently, we use five component grids whose union is the computational grid. The component grids consist of one Cartesian background grid that has grid lines aligned with the coordinate axes, and four boundary-fitted grids near the boundary. The solution values are interpolated between grids where they overlap. We generated a computational grid using the built-in capabilities of the Overture computational framework. We extend the boundary fitting grids from the boundary using transfinite interpolation (TFI), which is a generalized shearing transformation that maps the unit square onto the region bounded by four curves [23, 42]. Unlike grids based on extending normals from the boundary (Figure 4.2) [72, 73, 67], we can extend the boundary-fitting grids as much as we want without worrying about intersecting normal lines. This provides us with boundary-fitting grids that are wide enough to cover the menisci of the tear film. In addition, we double the grid spacing for the background Cartesian grid to reduce the number of grid points compared to previous work [72, 73, 67]. The new grid, plotted in Figure 5.1, reduces the total number of grid points by about 14% while achieving better overall accuracy for test problems (the new grid has a total number of 235,018 grid points). Unless otherwise noted, all the simulation results presented in this Chapter are computed using the computational grid in Figure 5.1.

5.2.2 A Hybrid Time-Stepping Scheme

To solve the equations (3.37)–(3.39), we first discretize the spatial derivatives using the second-order accurate finite difference method for curvilinear and Cartesian grids from Overture. Since the model equations (3.37)–(3.39) are weakly coupled by osmosis (terms involving P_c), we developed a hybrid time stepping scheme to solve the coupled system: we first solve the equation (3.39) for c using a dynamic explicit Runge-Kutta-Chebyshev (RKC) method [107]. Then we update the h and p equations (3.37) and (3.38), and solve them using a variable step size BDF method with fixed leading coefficient based on [17, 72, 73]. The resulting nonlinear system of the BDF method

is solved using Newton's iteration method. Solutions on different component grids are coupled by interpolation. The RKC method is suitable for this problem because it has an extended stability region with a stability bound that is quadratic in the number of stages, and as an explicit method it is fast and easy to implement. We exploit the nonlinear power method for an estimation of the largest eigenvalue of the spatially discretized system from (3.39) for c, and we use the quadratic relation to determine the number of stages needed for the RKC method. We have empirical criteria to determine whether an approximation is accepted or not. The number of stages is updated at every successful time step. More detailed description and preliminary tests of this method appear in Chapter 6.

5.3 Results

5.3.1 Constant Nonzero Permeability

We begin by presenting results for the model with the same constant water permeability over the whole ocular surface; we use the corneal permeability corresponding to $P_c = 0.013$ measured by [59, 19]. Figure 5.2 shows the contours of the simulation results. The left column represents the tear film thickness, and the right column represents the osmolarity. We see the dark band (blue online) set inside of the boundary, representing the so-called black line, emerges rapidly near to and inside of the menisci in the left column. The black line develops due to capillary action resulting from the positive curvature of the menisci generating a low pressure that sucks fluid into the meniscus. A local minimum thus forms near the meniscus, and is referred to as the black line. In addition, the canthi in the 2D eye-shaped domain induce a second direction of curvature, creating an even lower pressure that attracts fluid. Therefore, the tear film near the two canthi is often thinner than at other parts of the black line. In this case, the global minimum is located near the nasal canthus, which is sharper (more curved) than the temporal canthus. The formation of the global minimum is also promoted by the efflux of fluid near the nasal canthus due to the boundary conditions that mimic punctal drainage from this region. This also shows that both the thickness

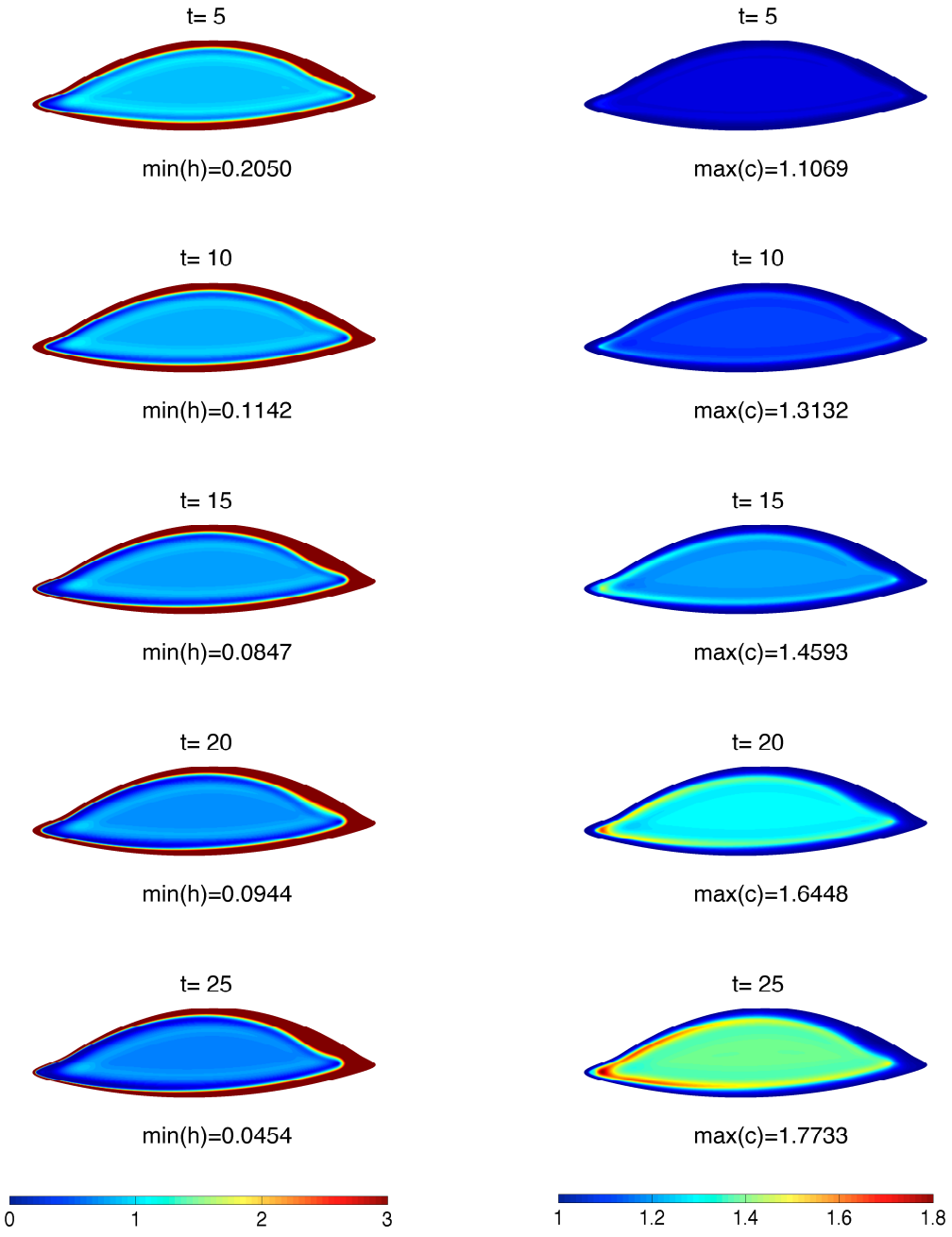

Figure 5.2: Contours of tear film thickness (left column) and osmolarity (right column) with constant permeability of $P_c = 0.013$ all over the exposed ocular surface and with Dirichlet boundary condition (3.48) on the osmolarity. The thinning rate is 4μm/min.

and osmolarity vary significantly away from the vertical line through the center of the cornea. Note 1D models formulated along this line do not account for this variation. The redistribution of fluid due to surface tension also causes a small ridge to form on the interior side of the black line. This is seen as a light band (turquoise online) in the left column of Figure 5.2. This light band is a ridge that has been seen in a number of other studies [72, 73, 67]. The tear film thickness in the interior decreases steadily throughout the computation because of evaporation; this is visualized by the continual darkening of the interior in the contour plots.

The corresponding osmolarity contours are plotted in the right column of Figure 5.2. Generally, the osmolarity increases more where the tear film is thinner, such as in the black line and canthi regions. This is in qualitative agreement with the results of [127]; we return to a direct comparison with their 1D results for $P_c = 0$ in the next section. The global maximum of osmolarity is in the nasal canthus that corresponds to the location of thinnest tear film. In the osmolarity plots, we observe a bright band indicating that a region of elevated osmolarity is forming near the developing black line. Osmolarity in the interior continues to increase as a result of evaporation, and the interior of the eye-shaped domain becomes brighter in the plots. In the region where tear film forms a small ridge, a corresponding darker band is also present on the interior side of the brighter band in the osmolarity plots.

The vertical cross-sectional plots ($x = 0$), shown in Figure 5.3, illustrate more directly the correlation between the tear film thickness and osmolarity: the osmolarity is roughly the reciprocal of the tear film thickness except in the black line and meniscus regions. Furthermore, comparison between Figure 5.3 and Figure 5.5 for the zero permeability case in the next section also reveals the effects of osmosis: the tear film is slightly thicker while the osmolarity is obviously smaller for the constant nonzero permeability case.

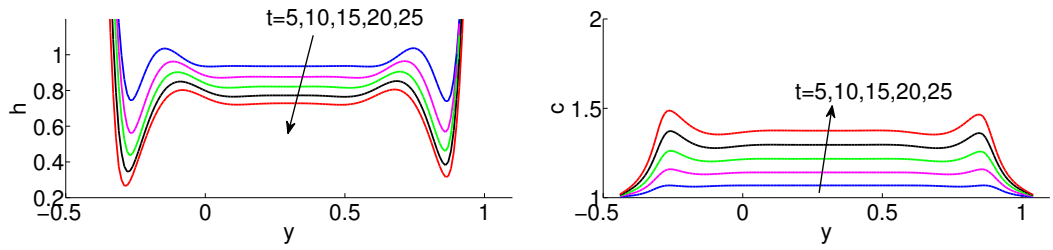

(a) Tear film thickness (b) Osmolarity

Figure 5.3: Cross-sectional plots through the vertical line $x = 0$ with $P_c = 0.013$ and Dirichlet boundary condition (3.48). The thinning rate is 4μm/min and the upper eyelid is located on the positive side of the y-axis.

5.3.2 Zero Permeability

Now we consider our model on an impermeable ocular surface, i.e. $Pc = 0$, so as to reveal the effect of osmosis by comparing with the previous results in §5.3.1, and we make comparisons with existing studies on 1D domains to show that our model provides consistent predictions. In this case, no water is supplied in response to the increased osmolarity that occurs when water evaporates from the tear film. Figure 5.4 shows the contours of both tear film thickness and osmolarity on the eye-shaped domain at $t = 25$. It shows that both the thickness and osmolarity vary significantly away from the vertical line through the center of the cornea. For example, the global minimum of tear film thickness is located in the nasal canthus and is much smaller than that in the cross-sectional plot. Furthermore, there is a spike in the osmolarity contour with a global maximum as large as $\max(c) = 4.8031$ in the nasal canthus. These global extrema and their locations cannot be found via 1D models, and to our knowledge are not available from clinical measurements either. From Figure 5.4, we also see more elevated osmolarity at the black line region, and the lowest concentration is located near the lacrimal gland as a result of the fresh tear supply. The tear film dynamics predicted by this model are in agreement with previous results [67].

The effect of osmosis can readily be seen by comparing the extreme values of different permeability cases. The extreme values of both h and c for several cases we

considered in this chapter are listed in Table 5.1. For the constant nonzero permeability case ($P_c = 0.013$), the minimum thickness ($\min(h) = 0.0454$) is slightly larger than that with zero permeability ($\min(h) = 0.0343$) at $t = 25$. However, the peak of osmolarity is significantly reduced by osmotic flows: $\max(c) = 1.7733$ with constant permeability and $\max(c) = 4.8031$ with zero permeability at $t = 25$. Therefore, according to our computation, we conclude that the presence of osmotic flux across the corneal surface may protect the tear film from excessive hyperosmolarity which could cause damage to the ocular surface and/or denaturation of tear film mucins and proteins [38].

Thinning rate:	4 μm/min			10 μm/min	20 μm/min
	$P_c = 0$	$P_c = 0.013$	$P_c(x,y)$	$P_c(x,y)$	$P_c(x,y)$
$\min(h(x,y,5))$	0.2043	0.2050	0.2070	0.1880	0.1557
$\min(h(x,y,10))$	0.1072	0.1142	0.1294	0.1102	0.0931
$\min(h(x,y,15))$	0.0819	0.0847	0.0899	0.0722	0.0506
$\min(h(x,y,20))$	0.0716	0.0944	0.1118	0.0906	0.0471
$\min(h(x,y,25))$	0.0343	0.0454	0.0492	0.0382	0.0268
$\max(c(x,y,5))$	1.1135	1.1069	1.0873	1.2392	1.5629
$\max(c(x,y,10))$	1.3925	1.3132	1.1722	1.5091	2.7505
$\max(c(x,y,15))$	1.6975	1.4593	1.2673	1.9892	5.3456
$\max(c(x,y,20))$	2.4841	1.6448	1.3852	2.6045	5.9684
$\max(c(x,y,25))$	4.8031	1.7733	1.5124	3.1486	6.0538

Table 5.1: Extreme values for various cases. $P_c(x,y)$ denotes the variable permeability case and is given by Equation (3.40).

Zubkov *et al.* [127] studied a system that included both tear film and osmolarity dynamics on a 1D domain with a moving end that mimicked blinks; their model assumes that the ocular surface is impermeable. To compare with their model, we set $P_c = 0$ and show the cross-sectional plots through the vertical line $x = 0$; the results are in Figure 5.5. The cross-sectional curves of our results on the 2D eye-shaped domain are comparable to the 1D results of [127] during the interblink phase for both the tear film thickness (Figure 5.5a) and the osmolarity distribution (Figure 5.5b), except that the development of black line is slower and the maximum osmolarity is higher in our results. The slower development of the black line in our results is due to the stationary

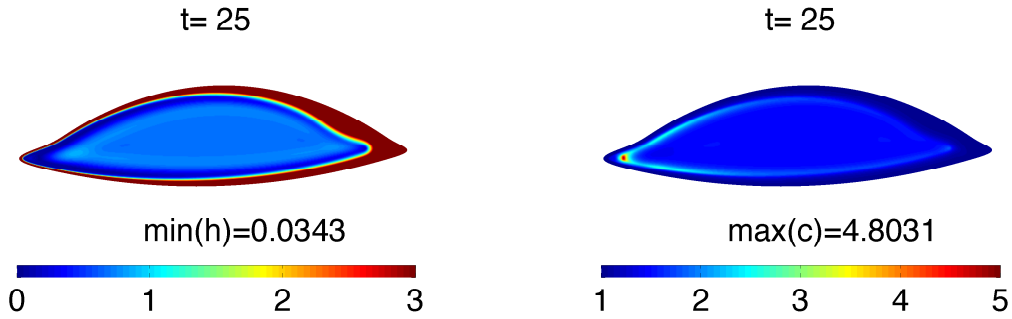

Figure 5.4: Contours of tear film thickness (left) and osmolarity (right) with $P_c = 0$ and Dirichlet boundary condition (3.48). The thinning rate is 4μm/min.

domain, because the formation of black line begins during the opening phase according to previous results on 1D blinking domains [49, 43, 14, 71, 127]. Nevertheless, the behavior of the tear film thickness in our model is in line with many previous results of 1D models with stationary ends [12, 124, 66]. The difference between the values of osmolarity stemmed from the different assumptions of the thinning rate and our longer time for computing the solution. The thinning rate in the model of [127] is assumed to be 0.24μm/min, which is much smaller than most of the observations of [92] and our choice of 4μm/min. Zubkov *et al.* have considered various evaporation rates to deduce that evaporation increases osmolarity, and they computed results for only 5 seconds, which explains the larger values of osmolarity we obtain as shown in Figure 5.5b.

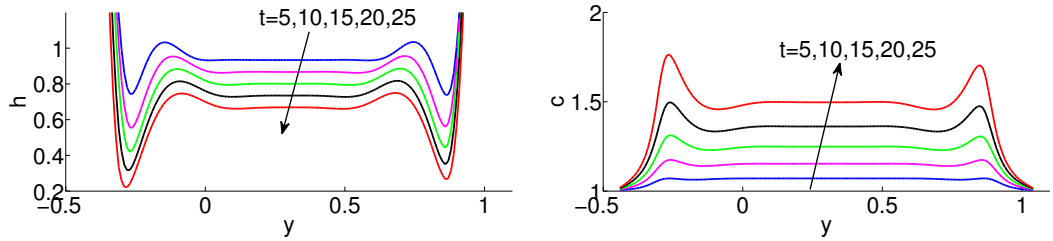

(a) Tear film thickness (b) Osmolarity

Figure 5.5: Cross-sectional plots through the vertical line $x = 0$ with $P_c = 0$ and Dirichlet boundary condition (3.48). The thinning rate is 4μm/min and the upper eyelid is on the positive side of y-axis.

5.3.3 Variable Permeability

In this section, we present simulated results by specifying the variable permeability $P_c(x, y)$ as defined in Equation (3.40). Figure 5.6 shows time sequences of the contours for both tear film thickness (left column) and osmolarity distribution (right column). Most of the dynamics of tear film thickness are similar to previous cases, such as the development of black line and the continuously thinning in the interior as a result of evaporation. However, due to the variable permeability of the ocular surface, we observe different patterns of tear film thickness over the conjunctival region and the corneal region in the left column of Figure 5.6. Since the cornea is less permeable, we see in the thickness plots that the tear film is thinner in the corneal region; it appears as a darker (blue) island in the center of the eye-shaped domain.

For the osmolarity distribution shown in the right column of Figure 5.6, several new patterns are observed beyond the elevated osmolarity in the black line region and the increasing of osmolarity due to evaporation. Because the cornea is less permeable than the conjunctiva, less osmotic flow is expected through the cornea, and this expectation is clearly captured by the model. In the osmolarity contours in Figure 5.6, we can clearly see a brighter disk in the region of cornea indicating higher osmolarity there. Combining the effect of surface tension and evaporation, the osmolarity is even larger in the black line region over the cornea, and the global maximum of osmolarity is attained there. Comparing with the constant permeability case, both $\min(h)$ and $\max(c)$ are slightly changed since, in the variable permeability case, we have a more permeable conjunctiva.

In order to better observe the transition from conjunctiva to cornea, we plot the horizontal cross-sectional plots (through the line $y = 0.3$ which is roughly across the geometric center of the cornea (GCC)) in Figure 5.7. Because of the puncta drainage and lacrimal gland supply specified by the time dependent fluid flux boundary condition (3.42), the tear film thickness is much smaller for $x < 0$ in Figure 5.7a. A local minimum of the tear film thickness, or black line, is still observed in the canthus regions due to the curvature of the menisci. The abrupt change of permeability from conjunctiva

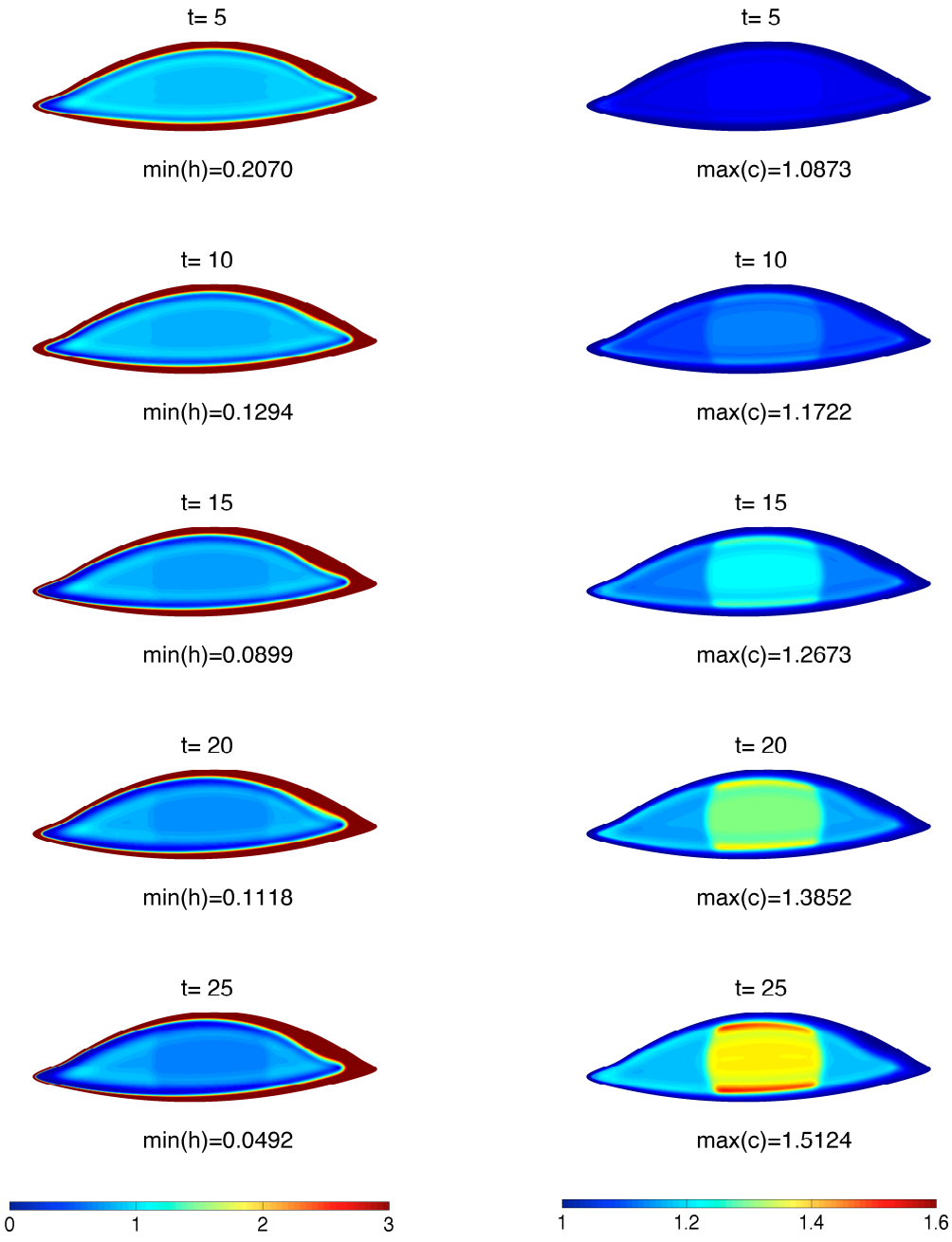

Figure 5.6: Contours of tear film thickness (left column) and osmolarity (right column) with variable permeability (3.40) and Dirichlet boundary condition (3.48). The thinning rate is 4μm/min.

to cornea is reflected by the tear film thickness. In Figure 5.7a, we see a rapid drop of tear film thickness around $x = \pm 1$ near the boundary of cornea. The transition of permeability influences the osmolarity distribution even more dramatically. After $t = 10$, the osmolarity in the cornea surpasses the osmolarity in the nasal canthus (the location of global peak of osmolarity for the zero and constant permeability cases).

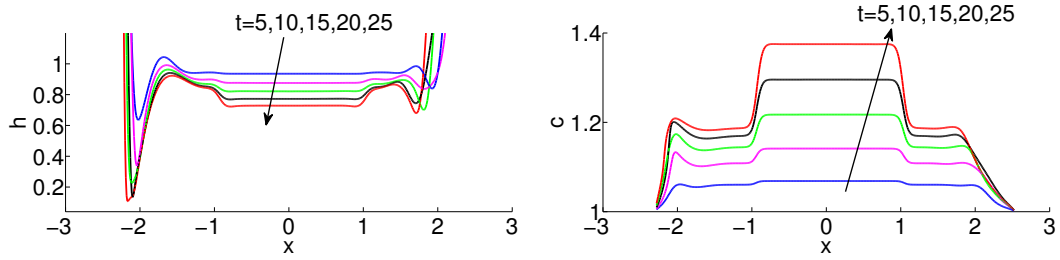

(a) Tear film thickness (b) Osmolarity

Figure 5.7: Cross-sectional plots through the horizontal line $y = 0.3$ with variable permeability (3.40) and Dirichlet boundary condition (3.48). Thinning rate is 4μm/min and the temporal canthus is located at the positive side of x-axis.

5.3.3.1 Diffusion

Diffusion also plays a role in the osmolarity dynamics. In Figure 5.8, we plot the diffusive term, $-[\nabla \cdot (h\nabla c)]/(h\mathrm{Pe}_c)$, in the c equation over the eye-shaped geometry to investigate its influence on the whole model system. From Figure 5.8, we see that the diffusion is non-negligible (indicated by the lighter colors for which the magnitude is greater than 10^{-2}) inside the black line regions; diffusion is actually of the same size as advection in the black line regions at $t = 20$. Our direct plots of the diffusion term on the eye-shaped domain confirm the results on a 1D domain of [127], who studied diffusion by comparing computed results for models with and without diffusivity. Even though the Pèclet number is large in the model system, diffusion helps to ameliorate the high osmolarity level in the black line regions. Diffusion could affect the osmolarity distribution similarly in local spots of break-up [96].

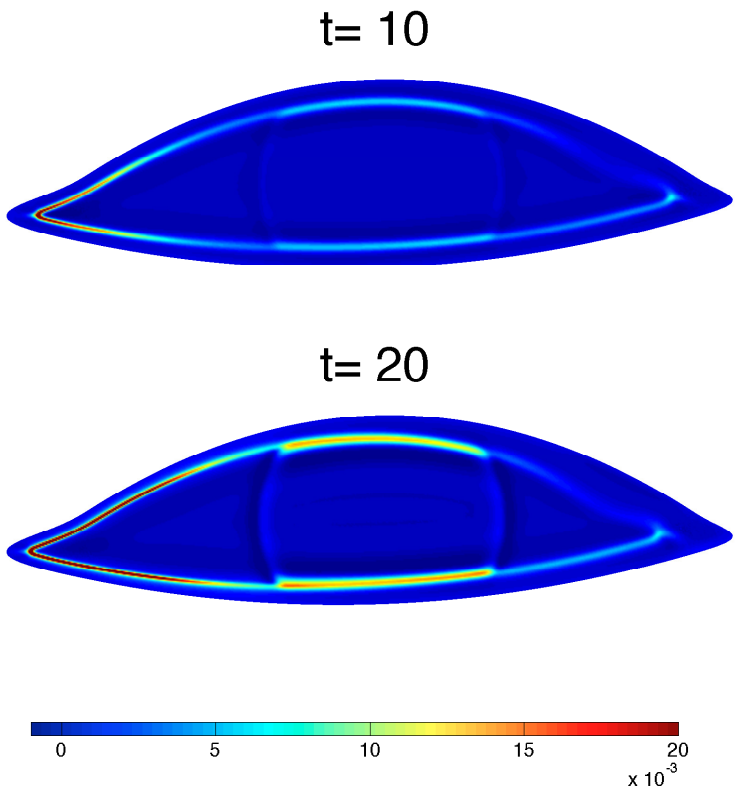

Figure 5.8: The contribution of diffusion to osmolarity dynamics. Diffusion is larger (magnitude greater than 10^{-2}) in the lighter areas.

5.3.3.2 Movement of Fluid and Solutes

Figure 5.9 shows quiver plots of the fluid flux $\mathbf{Q}$ at time $t = 1$ and $t = 20$. The normalized arrows in the plots show the directions only, and we use the shading to indicate the magnitude of the flux vector: the darker the background, the smaller the flux. In particular white indicates a flux greater than 10^{-2}; dark gray is less than 10^{-3}. At $t = 1$, the formation of black line dominates the movement of tear fluid. We see from the first plot of Figure 5.9 that relatively fast flow ($||\mathbf{Q}|| \geq 10^{-2}$) is observed near the menisci, and all the arrows point toward the eye lids. This is because the lower pressure created by the menisci attracts the nearby fluid, forming a locally thin region. This thin region is the black line and corresponds to the dark blue band as

we pointed out in the thickness contour plots previously. In the second plot of Figure 5.9, relatively fast fluid motion ($||\mathbf{Q}|| \geq 10^{-2}$) still occurs in the menisci; however, the arrows in the menisci show that the flow splits near the lacrimal gland and moves towards the nasal canthus along the eye lids. This hydraulic connectivity is thought to be caused by the pressure difference created by the time dependent influx and efflux on the boundary. The pressure gradient in the menisci drives the fluid flows towards the nasal side.

Li *et al.* [67] have studied tear flow over the eye-shaped geometry specifying the same time dependent flux BC (3.42). They discovered that, after the development of the black line, relatively fast fluid flow occurs in the menisci corresponding to the experimentally observed hydraulic connectivity, while on the inner side of the black line region, fluid flow is small. The model in this paper couples the fluid dynamics in the tear film with the osmolarity and still captures hydraulic connectivity.

The model equations (3.35) and (3.36) can be combined as a single PDE [96]:

$$\partial_t (ch) + \nabla \cdot \left(c\mathbf{Q} - \frac{h}{\mathrm{Pe}_c} \nabla c \right) = 0. \tag{5.1}$$

Here ch represents the mass per unit area of the solute. From this equation, we see that the solute would move with fluid flow, $\nabla \cdot (c\mathbf{Q})$, and would diffuse from higher concentration to lower concentration $\nabla \cdot (-h\nabla c)/\mathrm{Pe}_c$. However, since we have a very large Péclet number for the osmolarity, we expect the solute to move primarily with the fluid flow. Figure 5.10 shows the contours of the change of the mass per area as opposed to its initial condition: $c(x, y, t)h(x, y, t) - c(x, y, 0)h(x, y, 0)$. Blue indicates a decrease of mass, while red represents an increase at that location. The left plot of Figure 5.10 shows the redistribution of the solute at $t = 1$. We see a decrease of mass in the black line region and increase of mass in the menisci corresponding to the formation of black line; it matches with fluid movement as shown in Figure 5.9. At $t = 20$, the redistribution of mass (right plot of Figure 5.10) also matches the fluid motion; the increase of solute mass corresponds to the influx from the lacrimal gland, and subsequent flow around the meniscus. The decreases can be explained by the

drainage that occurred at the puncta. Another interesting point we note from Figure 5.10 is that variable permeability does not have an effect on ch, because Equation (5.1) does not depend on permeability at all. In general, solutes in the tear fluid move mostly with the fluid flow. Throughout the time considered, the change of $c(x, y, t)h(x, y, t)$ is rather small in the interior, and thus the reciprocal relation between c and h generally holds in the interior eye.

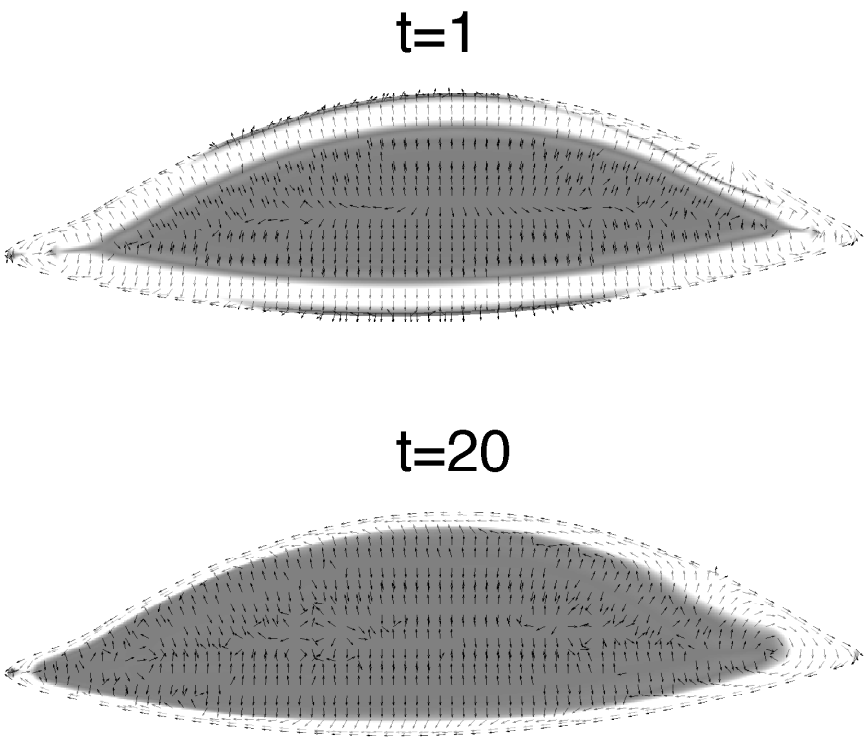

Figure 5.9: Fluid flux ($\mathbf{Q}$) over contours of its magnitude with variable permeability and thinning rate 4μm/min. (Far fewer arrows than the computational grid points are shown for clarity. All the arrows in this plot start at different locations.)

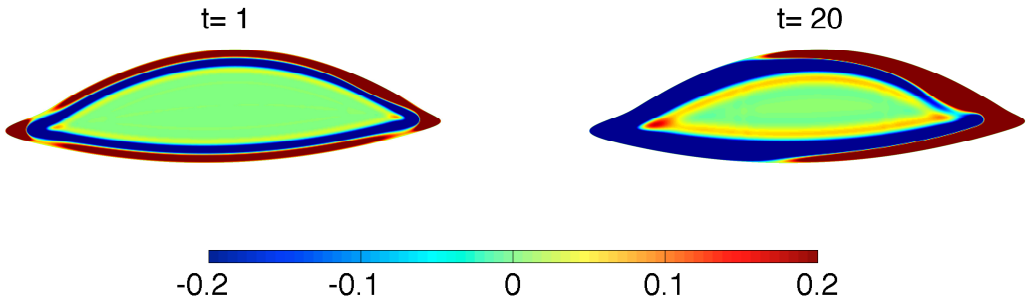

Figure 5.10: Contour for $c(x,y,t)h(x,y,t) - c(x,y,0)h(x,y,0)$ with variable permeability and thinning rate 4μm/min.

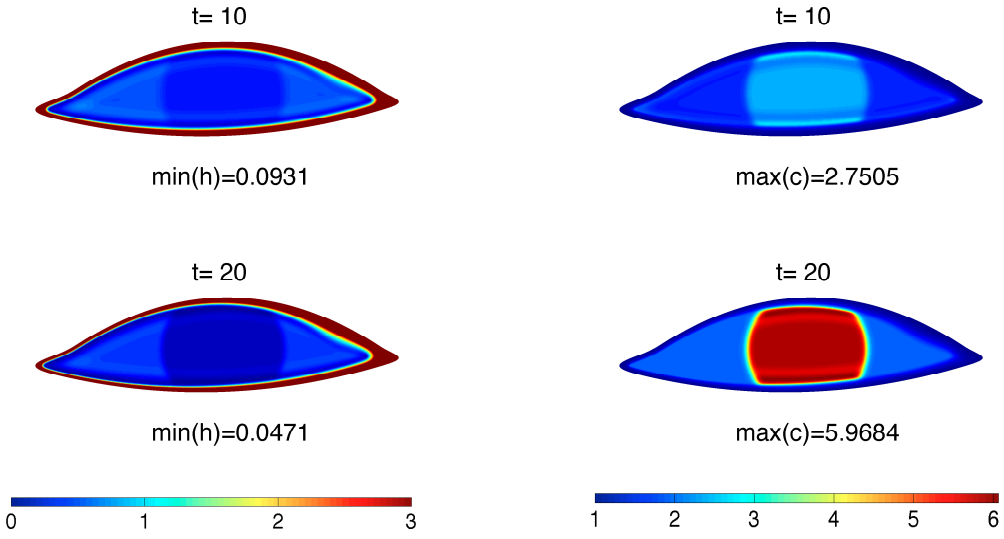

Figure 5.11: Contours of tear film thickness (left column) and osmolarity (right column) with variable permeability (3.40) and Dirichlet boundary condition (3.48). The thinning rate is 20μm/min.

5.3.4 Increased Evaporation Rate

The average thinning rate for the precorneal tear film (PCTF) measured by [92] is $3.79 \pm 4.20\mu$m/min, with the fastest observed PCTF thinning rate being 20μ/min. We attempt to investigate how evaporation influences tear film and osmolarity dynamics by adjusting the parameters that correspond to an increased thinning rate: 20μm/min.

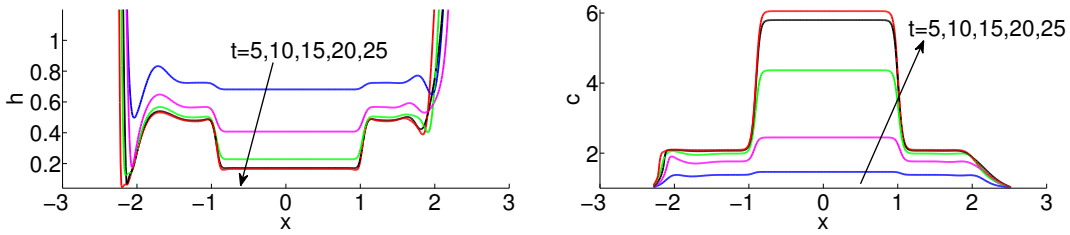

(a) Tear film thickness (b) Osmolarity

Figure 5.12: Cross-sectional plots through the horizontal line $y = 0.3$ with variable permeability (3.40) and Dirichlet boundary condition (3.48). Thinning rate is 20μm/min and the temporal canthus locates at the positive side of x-axis.

Figure 5.11 shows the contours of both $h(x, y, t)$ and $c(x, y, t)$ with parameters specified such that the thinning rate for a flat film is 20μm/min and with variable permeability. Compared with the previous results for the normal thinning rate (4μm/min), we observe the following effects deduced by elevated evaporation. In the thickness contour plots, we observe that the black line forms more rapidly, the interior tear film thickness decreases faster to a thinner level, the global minimum is smaller, and the transition from conjunctiva to cornea is more obvious. The associated osmolarity contours indicate that the osmolarity is more elevated with a larger global maximum value than the previous 4μm/min case. Moreover, the osmolarity difference between cornea and conjunctiva is more pronounced. In addition, we can see that tear film thins faster with higher evaporation by comparing the extreme values listed in Table 5.1. We deduce that evaporation increases osmolarity, confirming the 1D results of [127].

The horizontal cross-sectional plots shown in Figure 5.12 give another view of the tear film thickness and osmolarity, as well as their correlation. Clearly, the tear film becomes much thinner and osmolarity is much more elevated, especially over the corneal region (roughly $-1 \leq x \leq 1$) than with the normal thinning rate (4μm/min) case (Figure 5.7). The jump from cornea to conjunctiva is more obvious in both h and c. Higher osmolarity induces a larger osmotic flux from the ocular surface. Even though

the thinning rate is 5 times larger, the change in the film thickness and osmolarity are less than a factor of 5 different than those in Figure 5.7 and Table 5.1.

5.3.5 Osmotic Flux

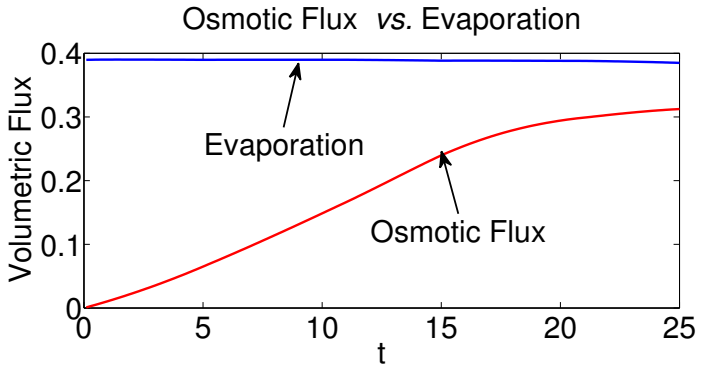

(a) Thinning rate is 20μm/min

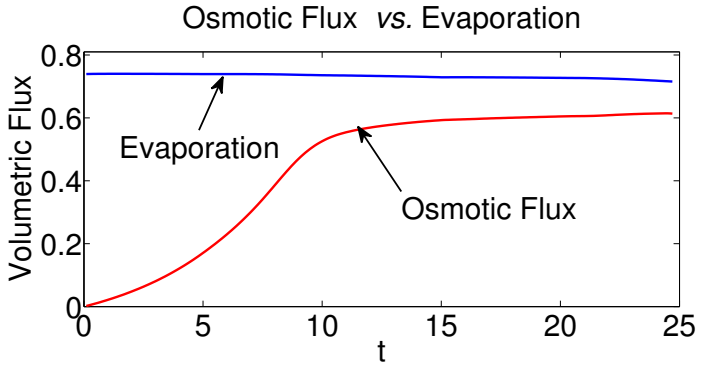

(b) Thinning rate is 38μm/min

Figure 5.13: Competition between evaporative loss and osmotic flux (volume/time)

A healthy eye is able to maintain a balance between tear loss and supply in a blink cycle. In our model system, we impose time-dependent tear fluid supply and drainage on the boundary that are balanced over a flux cycle ($\Delta t_{bc} = 10$). Over the ocular surface, water leaves the system by evaporation and is supplied by osmotic flux. We now study how the osmotic flux responds to evaporation, and whether the evaporative loss and osmotic flux reach a dynamic equilibrium over the entire eye.

To evaluate the volumetric flux of evaporation and osmosis, we integrate the PDE (3.35) over the eye-shaped domain Ω and find:

$$\text{volumetric flux of evaporation: } F_e(t) = \iint_\Omega EJ\, dA,$$

$$\text{volumetric flux of osmosis: } F_o(t) = \iint_\Omega P_c(c-1)\, dA.$$

We plot $F_e(t)$ and $F_o(t)$ together in Figure 5.13 to investigate the competition between evaporation and osmosis over the eye-shaped domain. Both plots in Figure 5.13 are simulation results with variable permeability, but with different thinning rates. Note that 38μm/min is the thinning rate of the bare water interface [96]. As is seen in the plots, osmotic flux is induced immediately in the simulations. The osmotic flux increases much faster with the higher thinning rate (38μm/min), and is seen to reach an equilibrium after $t = 15$. The volumetric flux of evaporation stays almost constant for the 20μm/min case, while a slight decrease is observed for the 38μm/min case. Faster evaporation makes the tear film thin faster, and reach the equilibrium thickness at more locations on the eye. The presence of van der Waals forces prevents the tear film from completely dewetting the ocular surface, and evaporation is shut off when and where a very thin equilibrium h is reached. This results in a decrease of volumetric flux of evaporation over the entire eye. We believe that ultimately the evaporation and osmosis would balance each other and the system would achieve a dynamic equilibrium. However, we cannot verify this because the pressure gradient inside the tear film, between the meniscus and the interior, becomes too steep for our current numerical methods to accurately resolve after $t = 25$. Similar issues limited the amount of time that could be computed in previous models as well [72, 73, 67]. We also doubt that the equilibrium between evaporation and osmosis can be observed in experiments because, before the equilibrium is reached, reflex tearing and/or blinks are more likely induced when the osmolarity level is high enough.

5.3.6 Neumann Boundary Condition for the Osmolarity

We also consider the homogenous Neumann boundary condition (3.49) for our system. It specifies no flux for osmolarity on the boundary; that is, solute cannot pass through the boundary. The computed results with this Neumann boundary condition (3.49) is rather similar to previous results using the Dirichlet boundary condition (3.48). This is because there is a large amount of fluid in the menisci and the fluid interaction between the menisci and interior is small due to the presence of black line separating them. Our numerical simulations using the Neumann boundary condition (3.49) also confirm that there is negligible difference from the results of using the Dirichlet boundary condition (3.48). Therefore, we do not include the results of the Neumann condition in this paper. However, results of the Neumann boundary condition are used to check the conservation of solute mass in our model system as an indication of numerical accuracy.

Integration of Equation (5.1) over the domain Ω gives the rate of change of the overall solute mass:

$$\partial_t M(t) + \iint_\Omega \nabla \cdot \left(c\mathbf{Q} - \frac{h}{\mathrm{Pe}_c} \nabla c \right) \, dA = 0.$$

Using the divergence theorem we obtain

$$\partial_t M(t) + \oint_{\partial\Omega} \left(c\mathbf{Q} - \frac{h}{\mathrm{Pe}_c} \nabla c \right) \cdot \mathbf{n}_b \, dS = 0, \tag{5.2}$$

where $M(t) = \iint_\Omega ch \, dA$ is the total mass of solute over the eye at time t. If we specify zero flux boundary condition for the fluid,

$$\mathbf{Q} \cdot \mathbf{n}_b \Big|_{\partial\Omega} = 0 \tag{5.3}$$

and homogenous Neumann boundary condition (3.49) for the osmolarity, then we conclude from Equation (5.2) that

$$M(t) = M(0),$$

that is, the solute mass is conserved over time. If our numerical simulation is reliable, the difference of mass defined as $\Delta M(t) = |M(t) - M(0)|$, where $M(t)$ is computed

Time	$\Delta M(t)$	Percentage of $M(0)$
5	0.0345	0.2452%
10	0.0542	0.3756%
15	0.0689	0.4774%
20	0.0812	0.5625%
30	0.1012	0.7015%

Table 5.2: Conservation of mass with boundary conditions (5.3) & (3.49)

numerically, should remain small throughout the simulation, and the magnitude of $\Delta M(t)$ can be regarded as an indication of the performance of the underlying numerical method as described in Section 5.2.

Table 5.2 lists both the absolute and relative changes of solute mass at various time for the computation with zero fluid flux BC and homogeneous Neumann BC for the osmolarity. The mass is not exactly conserved because numerical errors are introduced at every time step, and they accumulate slowly with time. From Table 5.2, we see that $\Delta M(t)$ increases with time, but the growth is not exponential, which can be regarded as a numerical evidence that the method is stable. Moreover, the numerical method we use is able to keep $\Delta M(t)$ very small throughout the computation; the relative change of mass is below 1%.

5.4 Conclusion

The mathematical model in this Chapter combines tear film flow, evaporation, osmolarity and osmosis on an eye-shaped domain representing the exposed ocular surface. To our knowledge, this is the first such model that includes the osmolarity in a two-dimensional tear film model. The results give information that we believe is not available from human subjects or animal models of the tear film. We believe that these results help give context to osmolarity measurements *in vivo* [9, 63]. The results show that the location and value of the minimum tear film thickness and maximum osmolarity are found to be sensitive to the permeability at the tear/eye surface.

Measurements of tear film osmolarity in human subjects are made from the inferior meniscus, or more commonly, the temporal canthus. These measurements have been calibrated with respect to DES so that diagnosis of DES is possible with better single-measurement specificity and sensitivity than other single signs or symptoms of DES [35, 63, 108]. But how do those measurements relate to what is going on in the dynamics of the rest of the tear film? For low evaporation rates of 1 micron/min or less, our results are similar to those of Zubkov *et al.* [127], with modest increases of osmolarity away from meniscus and particularly in the black line. For larger evaporation rates and longer interblink times, such as those that may be encountered in clinical experiments, our results indicate higher osmolarities. With variable permeability as suggested by experimental measurement [59], we find that for 4μm/min thinning rates, the peak value of the osmolarity increases 51% over the isotonic value, or about 457 Osm/m^3. This is just at the edge of sensory detection according to the results of Liu *et al.* [69], assuming that there is no neuropathy present that would reduce sensory perception at the ocular surface. For 10 and 20 μm/min thinning rates, we obtain maximum values of 951 and 1828 Osm/m^3, respectively; these values are quite high compared to what is mentioned for measurements reported in the literature, and would certainly be felt by subjects with normal neural function [69]. For all of these cases, the maximum occurs in the black line over the cornea. For the current model, there is very little change in the osmolarity in the outer canthus, which would make it difficult to use that location to deduce the different maxima in the osmolarity.

There are some limitations to the current study for linking the osmolarity measured *in vivo* with the computed results: (i) In our model, there is no lid motion to mix the tear fluid as occurs *in vivo*. This may be a significant component to the variability observed *in vivo*. (ii) Once the black line is formed in the computed results, there is little exchange between the tear film in the interior with the meniscus. The supply and drainage of tear fluid occurs in and affects primarily the meniscus, and this tends to hold the meniscal values of the osmolarity close to the isotonic value. (iii) The volume of tear fluid is probably large compared to DES subjects, and could affect the values of

osmolarity obtained. (iv) The model does not include break up per se, and there have been results that suggest that the osmolarity could be quite high in these localized regions (e.g. [69, 59, 15, 11, 96]). These points suggest possible fruitful directions for future research. Additional directions would include an dynamic lipid layer that affects the evaporation rate in a sensible way on the eye-shaped domain; possible models are those of of Bruna and Breward [20] and Peng *et al.* [96].

Chapter 6

NUMERICAL METHODS FOR COMPUTING TEAR FILM AND OSMOLARITY DYNAMICS ON AN EYE-SHAPED DOMAIN

6.1 Introduction

In this chapter, we discuss in detail the numerical methods that are used to compute the model system (3.37)–(3.39) on the eye-shaped domain (Figure 3.1). We discretize the eye-shaped domain using composite overlapping grids (Figure 4.2 & Figure 5.1), which consist of four boundary fitting grids that approximate solutions near the eye-shaped boundary and a background Cartesian grid covering the rest of the domain. The spatial derivatives in the equations are approximated with a curvilinear finite difference method. After discretization of the spatial variables, the model PDEs become a system of differential algebraic equations (DAE) with respect to time, which are then integrated using a hybrid time-stepping scheme that is developed based on the idea of fractional-step (splitting) methods [64]. We developed this hybrid time-stepping scheme with consideration of the stiffness of the DAE system. The DAEs resulted from the discretization of Equations (3.37) & (3.38) are very stiff (by definition, DAEs are infinitely stiff), so we want to use an implicit method to maintain stability of the numerical solutions while keeping relatively larger time steps for computational efficiency. The ODE system that is obtained from discretizing Equation (3.39) is of mild stiffness. Therefore, it can be solved using a special explicit method that has a large stability region. Additionally, we observed that the whole model system (3.37)–(3.39) is only weakly coupled by osmosis (terms involving P_c). Thus, we are able to solve the coupled system separately using an explicit Runge-Kuttta-Chebyshev (RKC) for the mildly stiff equations and a Backward Differentiation Formula (BDF) method for the extremely stiff equations. All the numerical simulations on 2D domains are conducted

using Overture computational framework (http://www.overtureframework.org. Primary developer and contact: W. D. Henshaw, henshw@rpi.edu), which is a collection of C++ libraries for solving PDEs on complex domains [23, 42].

We introduce the basic concepts of composite overlapping grid in Section 6.2, the BDF method in Section 6.3, and the RKC method in Section 6.4, with an emphasis on the RKC method. In Section 6.5, we focus on the implementation of the hybrid method. A preliminary test problem is solved to demonstrate the numerical accuracy in Section 6.6. Finally, we conclude our numerical study in Section 6.7.

6.2 Composite Overlapping Grid

The concept of composite overlapping grids and algorithms for generating them were discussed by Chesshire and Henshaw [23]. We only give a brief introduction here as background information for our numerical methods.

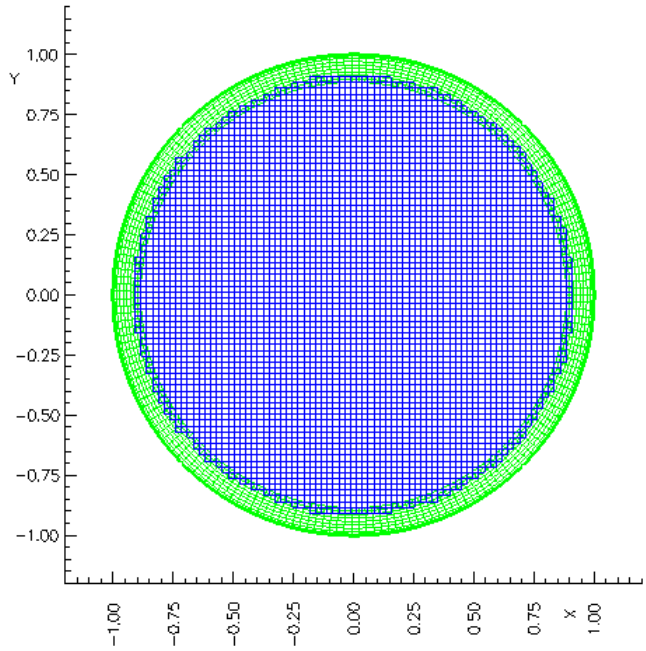

Figure 6.1: Composite overlapping grids on a unit disk.

A composite overlapping grid consists of a set of logically rectangular curvilinear component grids. The union of the component grids covers the computational domain, and the component grids overlap where they meet. Grid functions defined on different component grids are coupled by interpolation. One major advantage of composite overlapping grids is its capability of generating computational grids on domains of complicated geometry (e.g., the eye-shaped domain used in our models). We use Ogen [42], the overlapping grid generator of Overture, to generate our computational grids. For example, the grids shown in Figure 6.1 are created using Ogen. This is a composite overlapping grid on a unit disk consisting of one component grid near the boundary and one Cartesian component grid covering the rest of the disk. The two component grids overlap where they meet; algorithms implemented in Ogen determine the overlapping regions and interpolation procedures automatically. We use this grid, together with its refinements, to solve test problems discussed in Section 6.6.

6.2.1 Discretization on Composite Overlapping Grids

To numerically solve PDEs on a composite overlapping grid, we discretize the spatial derivatives first. Since each component grid is logically a rectangle (i.e., there exists a smooth mapping of a rectangle onto the component grid), it is suitable to approximate derivatives using finite difference methods on the rectangle with the given mapping. To be specific, consider a PDE of $u(x, y, t)$ on domain $\Omega \subset \mathbb{R}^2$:

$$F\Big(\partial_t u(x,y,t), \partial_x u(x,y,t), \partial_y u(x,y,t), u(x,y,t)\Big) = 0, \ \ (x,y) \in \Omega. \tag{6.1}$$

The domain Ω is discretized by a composite overlapping grid:

$$G = \bigcup_{k=1}^{n} G_k,$$

where G_k is a component grid. Each G_k discretizes a subdomain Ω_k of Ω, together with a mapping $\mathbf{f}_k$ that maps a unit square $[0,1] \times [0,1]$ onto Ω_k. On the subdomain Ω_k, we transform the PDE (6.1) into a PDE on the unit square:

$$F\Big(\partial_t u_k(r,s,t), \partial_x u_k(r,s,t), \partial_y u_k(r,s,t), u_k(r,s,t)\Big) = 0 \ \ \text{for} \ \ (r,s) \in [0,1] \times [0,1]\,,$$

where $(x, y) = \mathbf{f}_k(r, s)$ and $u_k(r, s, t) = u(\mathbf{f}_k(r, s), t)$. From the chain rule, we know that

$$\partial_x u_k(r, s, t) = \partial_r u_k(r, s, t)\partial_x r + \partial_s u_k(r, s, t)\partial_x s,$$
$$\partial_y u_k(r, s, t) = \partial_r u_k(r, s, t)\partial_y r + \partial_s u_k(r, s, t)\partial_y s.$$

The derivatives $\partial_x r, \partial_y r, \partial_x s$, and $\partial_y s$ are calculated from the inverse of the given mapping $\mathbf{f}_k$. At a grid point (x_i, y_j), we denote the approximation of $u(x_i, y_j, t) = u_k(r_i, s_j, t)$ by $U_{i,j}(t)$. Thus, we can approximate the spatial derivatives using standard finite difference methods for rectangular grids. For example, the approximation of $\partial_r u_k(r_i, s_j, t)$ following the second order centered finite difference scheme is given by

$$\partial_r u_k(r_i, s_j, t) \approx \frac{U_{i+1,j}(t) - U_{i-1,j}(t)}{2\Delta r}.$$

Overture provides the derivatives ($\partial_x r, \partial_y r, \partial_x s$, and $\partial_y s$) of the transformation at grid points, and offers a wide range of methods to discretize the other derivatives on the unit square domain $[0, 1] \times [0, 1]$. Moreover, Overture uses interpolation to obtain grid function values at points where component grids overlap. In this dissertation, we use the second order centered finite difference scheme and second order interpolation for all our calculations.

After discretizing the spatial derivatives, the PDE (6.1) becomes a system of ODEs/DAEs for $U_{i,j}(t)$. Therefore, we are also interested in time-stepping methods to solve the system of equations for $U_{i,j}(t)$.

6.3 BDF Method

In this section, we introduce the variable step size BDF method with fixed leading coefficient; it is an implicit time-stepping method that is suitable for stiff systems. This method is introduced in Chapter 5 of the book by Brenan *et al.* [17], and is used by us to solve tear film model on the 2D eye-shaped domain in Chapter 4. Maki *et al.* [72, 73] utilized this method for their simulations as well.

The BDF method discussed here is for solving DAE system of index zero or one of the following form:

$$\begin{aligned}
&\mathbf{F}\big(t, \mathbf{u}(t), \mathbf{u}'(t)\big) = 0,\\
&\mathbf{u}(0) = \mathbf{u}_0,\\
&\mathbf{u}'(0) = \mathbf{u}'_0.
\end{aligned}$$

Here $\mathbf{F}, \mathbf{u}(t), \mathbf{u}_0, \mathbf{u}'_0$ are all vectors of dimension N. The idea of the BDF method is to replace $\mathbf{u}'$ at current time t_{n+1} with a backward differentiation formula and to solve the resulting nonlinear equations for $\mathbf{U}_{n+1}$, where $\mathbf{U}_{n+1}$ is the numerical approximation of $\mathbf{u}(t_{n+1})$. To be specific, suppose we know $\mathbf{U}_{n-i}$ for $i = 0, 1, \ldots, k$, where k is the order of BDF method we plan to use, namely, we know the numerical approximations of $\mathbf{u}(t)$ for the previous $k+1$ times. An initial guess of the solution and its derivative at t_{n+1} is obtained from the predictor polynomial $\omega^P_{n+1}(t)$, which is the polynomial determined by interpolating the previous $k+1$ solutions $\mathbf{U}_{n-i}$ for $i = 0, 1, \ldots, k$, i.e.,

$$\omega^P_{n+1}(t_{n-i}) = \mathbf{U}_{n-i}, \quad \text{for } i = 0, 1, \ldots, k.$$

We then obtain the predicted values U^0_{n+1} and U'^0_{n+1} for $\mathbf{u}(t_{n+1})$ and $\mathbf{u}'(t_{n+1})$ by evaluating $\omega^P_{n+1}(t)$ and $\omega'^P_{n+1}(t)$ at t_{n+1}. Thus, we have

$$U^0_{n+1} = \omega^P_{n+1}(t_{n+1}), \quad U'^0_{n+1} = \omega'^P_{n+1}(t_{n+1}).$$

To get the accepted approximation $\mathbf{U}_{n+1}$, we solve a corrector formula. We define a corrector polynomial $\omega^C_{n+1}(t)$ such that it interpolates the predictor polynomial at k equal time steps behind t_{n+1} and $\mathbf{U}_{n+1}$ is the solution of the corrector polynomial at t_{n+1}, that is,

$$\omega^C_{n+1}(t_{n+1} - i\Delta t_{n+1}) = \omega^P_{n+1}(t_{n+1} - i\Delta t_{n+1}) \quad \text{for } i = 1, \ldots, k, \tag{6.2}$$

$$\omega^C_{n+1}(t_{n+1}) = \mathbf{U}_{n+1}. \tag{6.3}$$

In addition, since $\mathbf{U}_{n+1}$ must satisfy the DAE at t_{n+1}, we then have

$$\mathbf{F}\big(t_{n+1}, \mathbf{U}_{n+1}, \mathbf{U}'_{n+1}\big) = \mathbf{0}. \tag{6.4}$$

Differentiating Equation (6.2) at t_{n+1} yields

$$\alpha_s(\mathbf{U}_{n+1} - \mathbf{U}^0_{n+1}) + \Delta t_{n+1}(\mathbf{U}'_{n+1} - \mathbf{U}'^0_{n+1}) = 0,$$

where

$$\alpha_s = -\sum_{j=1}^{k} \frac{1}{j}.$$

We then solve for $\mathbf{U}'_{n+1}$ and substitute it into Equation (6.4) to obtain a nonlinear equation of $\mathbf{U}_{n+1}$

$$\mathbf{F}\big(t_{n+1}, \mathbf{U}_{n+1}, \mathbf{U}'^0_{n+1} - \frac{\alpha_s}{\Delta t_{n+1}}(\mathbf{U}_{n+1} - \mathbf{U}^0_{n+1})\big) = \mathbf{0}. \tag{6.5}$$

The nonlinear equation (6.5) is solved using Newton's iteration method. More details about the implementation, step size selection, and error analysis for the BDF method alone can be found in Chapter 5 of Brenan *et al.* [17] and Chapter 6 of Maki's dissertation [70].

6.4 RKC Method

In this section, we introduce an explicit time-stepping method, Runge-Kutta-Chebyshev (RKC) method. The RKC scheme we use was designed by van der Houwen & Sommerijier [116] based on the three-term Chebyshev recursion,

$$T_0(x) = 1, \quad T_1(x) = x, \quad T_j(x) = 2xT_{j-1}(x) - T_{j-2}(x), \tag{6.6}$$

where $T_j(x)$ is the Chebyshev polynomial of the first kind. The RKC method is an s-stage Runge-Kutta (RK) method designed for the explicit integration of nonoscillatory stiff systems of ODEs originating from spatial discretization of a parabolic PDE (method of lines) [119]:

$$\mathbf{U}'(t) = \mathbf{F}(t, \mathbf{U}(t)), \quad \mathbf{U}(0) = \mathbf{U}_0 \in \mathbb{R}^m. \tag{6.7}$$

There are many attractive features of the RKC method. The method possesses an extended stability region: the length of the real stability interval β is proportional to s^2. Importantly, this method can be easily applied with arbitrary number of stages.

Considering that the stability interval length β is proportional to the square of number of stages, the RKC method is well-suited to solve some nonoscillatory stiff systems. However, it is advised to use alternative methods (e.g., BDF method) if the system is so stiff that it requires the number of stages far beyond 100 for the RKC method [107].

The designing principle of the RKC method is to construct formulas with regions of absolute stability that are as large as possible, instead of constructing RK formulas to achieve the highest order possible. A low order formula is appropriate since the spatial discretization is only of modest accuracy (second order centered finite difference in our applications). Because of this, RKC formulas are designed to be of order two [118, 107].

6.4.1 RKC Formulas

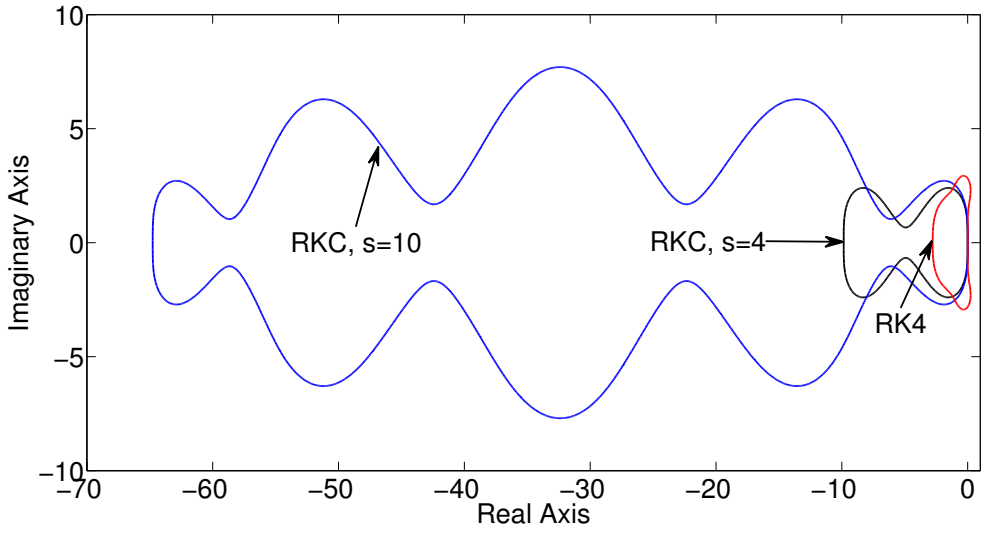

Figure 6.2: Stability regions of various RK methods (the regions enclosed by the curves).

The RKC formula are derived from a desired stability polynomial $R_s(z)$, where s is the number of stages. In the case of van der Houwen & Sommeijer [116], the stability polynomial of the RKC method is set to be

$$R_s(z) = a_s + b_s T_s(w_0 + w_1 z), \tag{6.8}$$

where

$$w_0 = 1 + \frac{\epsilon}{s^2},\ \epsilon \approx 0.15,\ w_1 = \frac{T_s'(w_0)}{T_s''(w_0)},\ b_s = \frac{T_s''(w_0)}{(T_s'(w_0))^2},\ a_s = 1 - b_s T_s(w_0).$$

Figure 6.2 displays the stability regions of the RKC methods with stages $s = 4$ and $s = 10$, as well as the stability region of RK4 method for comparison. The stability region of the RKC method is a strip extended along the negative real axis. The length of the stability strip $\beta(s)$ is estimated as $\beta(s) \approx 0.65(s^2 - 1)$ [120]. Details about the selection of stability polynomial can be found in Chapter IV of the book by Hairer & Wanner [40] and the review paper by Verwer [118].

van der Houwen & Sommerijier [116] constructed the RKC method in such a way that all polynomials $R_j(z)$ of the intermediate stages are defined by the three-term Chebyshev recursion (6.6), and the selected stability polynomial $R_s(z)$ (6.8) results at the final stage s. Thus, van der Houwen & Sommerijier [116, 118] used

$$R_j(z) = a_j + b_j T_j(w_0 + w_1 z) \text{ for } 0 \le j < s. \tag{6.9}$$

Implementing the Chebyshev recursion (6.6) together with $R_j(0) = 1$ (the second order condition), the following relations for $R_j(z)$ are obtained,

$$\begin{aligned} &R_0(z) = 1,\ R_1(z) = 1 + \tilde{\mu}_1 z, \\ &R_j(z) = (1 - \mu_j - \nu_j) + \mu_j R_{j-1}(z) + \nu_j R_{j-2}(z) + \tilde{\mu}_j R_{j-1}(z) z + \tilde{\gamma}_j z, \end{aligned}$$

where

$$\tilde{\mu}_1 = b_1 w_1,\ \mu_j = \frac{2 b_j w_0}{b_{j-1}},\ \nu_j = \frac{-b_j}{b_{j-2}},\ \tilde{\mu}_j = \frac{2 b_j w_1}{b_{j-1}},\ \tilde{\gamma}_j = a_{j-1}\tilde{\mu}_j,\ j = 2, \ldots, s.$$

From the relations of $R_j(z)$, one can readily deduce the explicit RKC method for the general nonlinear problem (6.7). Let $\mathbf{Y}_j$ denote the intermediate RK approximation.

Then the scheme to integrate the ODE system (6.7) from t_n to t_{n+1} reads,

$$\begin{aligned}
&\mathbf{Y}_0 = \mathbf{U}_n, \\
&\mathbf{Y}_1 = \mathbf{Y}_0 + \tilde{\mu}_1 \tau \mathbf{F}_0, \\
&\mathbf{Y}_j = (1-\mu_j-\nu_j)\mathbf{Y}_0 + \mu_j \mathbf{Y}_{j-1} + \nu_j Y_{j-2} + \tilde{\mu}_j \tau \mathbf{F}_{j-1} + \tilde{\gamma}_j \tau \mathbf{F}_0, \ j = 2, \ldots, s, \\
&\mathbf{U}_{n+1} = \mathbf{Y}_s.
\end{aligned} \tag{6.10}$$

Here $\tau = t_{n+1} - t_n$ and $\mathbf{F}_j = \mathbf{F}(t_n + c_j\tau, \mathbf{Y}_j)$, where c_j is the increment parameter. According to Verwer *et al.* [119], c_j is given by

$$c_0 = 0, \ c_1 = \tilde{\mu}_1, \text{ and } c_j = \mu_j c_{j-1} + \nu_j c_{j-2} + \tilde{\mu}_j + \tilde{\gamma}_j \text{ for } 2 \le j \le s.$$

6.4.2 Implementation of RKC Method

We implement the RKC formulas (6.10) dynamically following the procedures discussed by Sommeijer *et al.* [107]. We estimate the stiffness of the current system by evaluating the spectral radius of the Jacobian matrix of the system. Then we determine the number of stages for the RKC integration based on the current time step and the estimated spectral radius. We also adjust time steps according to the error estimations and time step prediction strategy discussed below.

6.4.2.1 Local Error Estimation

Extensive testing for both linear and nonlinear problems confirms that the local error of RKC methods can be regarded as independent of the number of stages ($s \ge 2$) for practical purposes [107, 119]. A good approximation of the leading term of the local error expansion is

$$e_l(t) = \frac{1}{15}\tau^3 \frac{d^3\mathbf{u}(t_n)}{dt^3}. \tag{6.11}$$

The approximation $e_l(t)$ comes from replacing the stage-dependent constants by their limiting values. Thanks to the simple form given in Equation (6.11), one can make an asymptotically correct estimation [107]:

$$Est_{n+1} = \frac{1}{15}\left[12(\mathbf{U}_n - \mathbf{U}_{n+1}) + 6\tau\left(\mathbf{F}(\mathbf{U}_n) + \mathbf{F}(\mathbf{U}_{n+1})\right)\right].$$

At each step, the estimated local error is controlled by specified tolerance,

$$\text{Tol} = atol + rtol\mathbf{U}_{n+1}.$$

Tol is a vector of the dimension m (the same as $\mathbf{U}_{n+1}$), $atol$ and $rtol$ are two specified numbers for absolute and relative tolerances. Since all the numerical methods involved are of order two, it is not advised to specify stringent tolerances. In our simulations, $atol = 10^{-4}$ and $rtol = 10^{-5}$. For convenience, we use a single scalar absolute error tolerance to decide whether a step is accepted or not. The scalar tolerance we use is the weighted root mean square (RMS) norm:

$$||Est_{n+1}||_{\text{RMS}} = ||w^{-1}Est_{n+1}||_2,$$

where

$$w = \frac{1}{\sqrt{m}}\text{diag}(\text{Tol}).$$

We accept the current step if $||Est_{n+1}||_{\text{RMS}} \leq 1$. Otherwise, we reject the solution and redo the computation with adjusted step size.

6.4.2.2 Time Step Prediction

Following the studies in [122, 39, 107], we use the formula below to predict the new step size,

$$\tau_{new} = \min(10, \max(0.1, \text{fac}))\tau, \tag{6.12}$$

where τ is the current step size in use and the factor is defined by

$$\text{fac} = 0.8\left(\frac{||Est_n||^{1/(p+1)}}{||Est_{n+1}||^{1/(p+1)}}\frac{\tau_n}{\tau_{n-1}}\right)\frac{1}{||Est_{n+1}||^{1/(p+1)}}.$$

Here p is the order of consistency ($p = 2$ in our case). New step size is predicted after a successful step, and is resized after a rejection using the formula (6.12).

6.4.2.3 Number of RKC Stages

At each time step, we have a prediction of step size τ_{new} from Equation (6.12), and then we want to determine the number of stages to use for the RKC method such

that the step size τ_{new} is absolutely stable. We already knew from Section 6.4.1 that the stability of an s-stage RKC methods is a strip extended in the negative real axis with length estimated as $\beta(s) \approx 0.65(s^2 - 1)$. To obtain absolute stability, we require

$$\tau_{new}\sigma(J_{\mathbf{F}}(\mathbf{U}_n)) \leq 0.65(s^2 - 1),$$

where $J_{\mathbf{F}}(\mathbf{U}_n)$ is the Jacobian matrix of $\mathbf{F}(\mathbf{u})$ at t_n and $\sigma(J_{\mathbf{F}}(\mathbf{U}_n))$ represents the spectral radius of the matrix. Therefore, we choose

$$s = 1 + \lfloor \sqrt{1.54\tau_{new}\sigma(J_{\mathbf{F}}(\mathbf{U}_n)) + 1} \rfloor, \tag{6.13}$$

where $\lfloor \cdot \rfloor$ is the floor function. In order to get an estimation of the stage number s using Equation (6.13), we need to find the spectral radius ($\sigma(J_{\mathbf{F}}(\mathbf{U}_n))$ first. To do so, we implement a nonlinear power method in our code to estimate the spectral radius automatically at each successful step.

6.5 A Hybrid Time-Stepping Method

Data: Solution of the system at t_n: $\mathbf{h}_n$, $\mathbf{p}_n$, $\mathbf{c}_n$
Result: Solution of the system at t_{n+1}: $\mathbf{h}_{n+1}$, $\mathbf{p}_{n+1}$, $\mathbf{c}_{n+1}$
BDF solver predicts a step size: dt;
while *Not Accepted* **do**
  $t_{n+1} = t_n + dt$;
  RKC solver integrates $\mathbf{c}$ equation from t_n to t_{n+1} to get $\mathbf{c}_{n+1}$ (RKC solver predicts its own step size τ to integrate from t_n to t_{n+1});
  Pass $\mathbf{c}_{n+1}$ into BDF solver and solve for $\mathbf{h}_{n+1}, \mathbf{p}_{n+1}$;
  if *Not Accepted* **then**
    resize dt;
  else
    Accepted;
  end
end

Algorithm 1: Integration from t_n to t_{n+1} using the hybrid time-stepping method

In this section, we develop an hybrid time-stepping method based on the idea of fractional-step method. This hybrid time-stepping method is suitable for a system

consisting of weakly coupled systems of stiff and mildly stiff equations. This method is specifically designed to efficiently solve the tear film and osmolarity system (3.37)–(3.39).

The idea of our hybrid method is straightforward. We first solve the mildly stiff equations using RKC method, and then we update the stiff equations and solve them with BDF method. Suppose we have successfully solved the discretized system of (3.37)–(3.39) at t_n, we then want to solve it for the next time step. We describe the detailed procedure of this hybrid method in Algorithm 1.

6.6 Test Problems

In this section, we formulate a test problem to investigate the numerical properties of our methods. We solve a test problem on composite overlapping grids using the RKC method to study its performance. The test problem is formulated such that it is similar to the osmolarity Equation (3.39) with the exact solution given by

$$C(x,y,t) = (1 + x + x^2 + x^3 + y + y^2 + y^3)(1 + t + t^2). \tag{6.14}$$

To be specific, the test problem is formulated as follows,

$$\partial_t c = -\frac{1}{h}\nabla c \cdot \left(-\frac{h^3}{12}\nabla p\right) + \frac{1}{\mathrm{Pe}_c h}\nabla \cdot (h\nabla c) + f(x,y,t), \tag{6.15}$$

where

$$h = 1 + 2\exp\left(10(x^2 + y^2 - 1)\right),\ p = -S\Delta h, \tag{6.16}$$

and the forcing term $f(x,y,t)$ is obtained by substituting the exact solution (6.14) into the test problem (6.15). The specification of h (6.16) mimics the bowl shape geometry of the tear film. Also noting that h is time independent and becomes a variable coefficient in Equation (6.15). We solve the test problem on both the simplified circular domain as shown Figure 6.1 and the eye-shaped domain. On the simplified circular domain, we solve the test problem using the RKC method with several mesh refinements. For each refinement, we double the resolution, i.e., the grid sizes Δx and

	Refinement 0	Refinement 1	Refinement 2	Refinement 3	Refinement 4
Error	e_0=1.17e-5	e_1= 1.64e-6	e_2= 3.31e-7	e_3= 5.70e-8	e_4= 1.43e-8
Ratio	$e_0/e_1 = 7.13$	$e_1/e_2 = 4.95$	$e_2/e_3 = 5.80$	$e_3/e_4 = 3.98$	

Table 6.1: Errors of the test problem on the circular domain at $t = 2$.

Δy are reduced by half. We list the errors of the test problem solved on the composite overlapping grid (Figure 6.1) and its refined grids in Table 6.1. The error in the table is defined by

$$e(t) = ||c(x, y, t) - C(x, y, t)||_2. \tag{6.17}$$

From Table 6.1, we can see that the error ratios roughly converge to 4 as expected since we use the second order finite difference method to discretize the spatial derivatives.

We also solve the test problem (6.15) on the eye-shaped domain using the composite overlapping grid shown in Figure 5.1. Since this grid is not evenly spaced and is more computationally intensive, we do not test refinements as we did for the simplified circular domain. We only solve the test problem once and present the absolute error to indicate numerical accuracy on the eye-shaped domain. Figure 6.3a and Figure 6.3b show the numerical solution and error distribution on the eye-shaped domain, respectively. The largest errors are located in the two canthi, the absolute error defined by Equation (6.17) is 1.84e-5 at $t = 2$.

In short, the implementation of RKC method on composite overlapping grids is very accurate. Moreover, we are also very confident about the accuracy of the numerical solutions on the eye-shaped domain according to our test results.

6.7 Conclusion

In this chapter, we give a complete discrpition of the numerical methods we implemented to compute the solutions of our models on the 2D eye-shaped domain. We developed a hybrid time-stepping method based on the idea of fractional-step method. This hybrid time-stepping method is specifically for solving the tear film-osmolarity coupled system. The development of this method considers the numerical features of

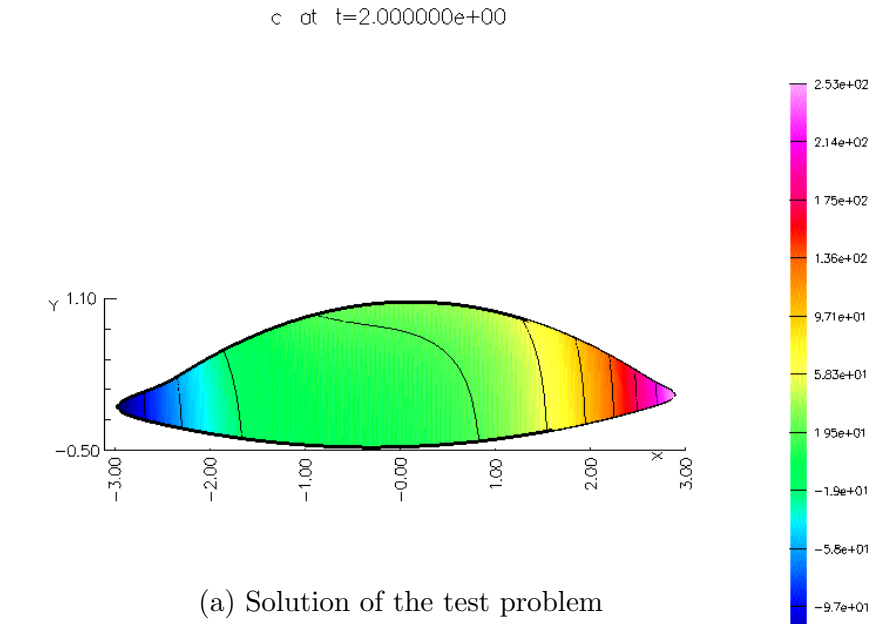

(a) Solution of the test problem

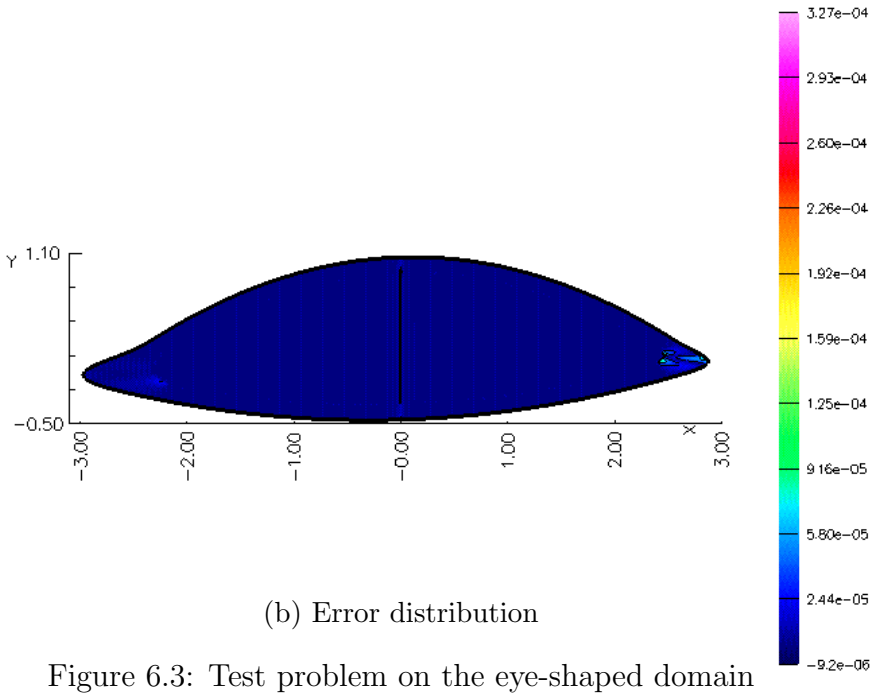

(b) Error distribution

Figure 6.3: Test problem on the eye-shaped domain

our model system, which consists of a mildly stiff system of ODEs that arise from the discretization of the osmolarity equation and a very stiff system of DAEs that arise

from the discretization of the film thickness and pressure PDEs. The hybrid time-stepping method is a combination of RKC and BDF methods. The RKC method is an efficient explicit method suitable for mildly stiff system of ODEs such as the discretized osmolarity equations, while the BDF is a fully implicit method that efficiently solves a very stiff system such as that from the tear film and pressure equations. We conducted a preliminary numerical study by solving a test problem on a simple circular domain, as well as the eye-shaped domain. Solution to the test problem provides numerical evidence for the accuracy and stability of our methods.

There are limits of our current test problem in Section 6.6. In stead of solving the h equation using BDF method, we specify h with a bowl-shaped function that mimics the tear film geometry, and then we solve the mildly stiff convection-diffusion-reaction equation 6.15 using RKC method. In the future, we want to formulate a test problem that characterizes the numerical features of the film-osmolarity system (3.37)–(3.39) and solve it using the hybrid time-stepping method discussed in Section 6.5 directly. In addition, we are also interested in conducting numerical analysis to get some theoretical understandings of the hybrid time-stepping method.

Chapter 7

CONCLUSION

In this dissertation, we have presented three mathematical models that focuses on various aspects of human tear film dynamics and developed numerical methods to compute the solutions of the model equations. Our results provide many new insights about the human tear film dynamics, as well as the associated thermal and osmolarity dynamics. The hybrid time-stepping method is worth further study as well.

In Chaper 2, we presented a mathematical model that incorporates the heat transfer from within the cornea and part of the aqueous humor. To our knowledge, this is the first model that couples heat transfer into the tear film dynamics model. We considered three model domains for heat transfer underneath the tear film. The model domains are simplified geometries that represent the anterior eye and that may include the cornea and some aqueous humor; one model domain is asymptotically thin (thin substrate) and the other has finite thickness (thick substrate). The thick substrate case captures temperature decreases that are observed *in vivo*, while the thin substrate and fixed temperature models do not. Also, this model captures the experimentally measured thinning rate of tear film thickness. This modeling approach of incorporating heat transfer into tear film has led to two more publications by Deng *et al.* on a domain with moving end mimicking blinks [27, 26].

We then restricted our attention on modeling and computing tear film models on a 2D eye-shaped domain. In Chapter 3, we formulated a model that couples the tear film and osmolarity dynamics for the first time on a 2D eye-shaped domain. This is the first such model that couples osmolarity dynamics with a 2D tear film model. In addition, with the specification of a time-dependent flux boundary condition that models the lacrimal gland supply and puncta drainage of the tear fluid, we were able

to recover some effects of blinking on a stationary 2D eye-shaped domain. In the two subsequent chapters, we conducted extensive analysis for our model predicted results and made careful comparison with experimental and other theoretical studies.

In Chapter 4, we focused on the fluid dynamics part of the 2D model by neglecting osmolarity dynamics. We found that the time-dependent flux boundary condition captures some effects of blinks on a stationary domain and helps to establish the hydraulic connectivity as observed by many *in vivo* experiments. Our model also captures new details about tear flows in the meniscus, beyond the reach of one-dimensional models. We also described experiments using fluorescein that visualized tear film thickness changes, and indirectly, the supply of fresh tear fluid and where the more diluted fluid moves. Moreover, this model captures the evaporation rate very well for comparison with well-controlled laboratory experiments. The result yielded by the model is comparable to the measurements conducted with the ventilated-chamber method or in the free air.

In Chapter 5, we solve the complete model derived in Chapter 3 to explore the osmolarity dynamics and the interaction between tear film and osmolarity. The results give information that we believe is not available from human subjects or animal models of the tear film. We believe that these results help give context to osmolarity measurements *in vivo* [9, 63]. The results show that the location and value of the minimum tear film thickness and maximum osmolarity are found to be sensitive to the permeability at the tear/eye surface, and provide a global view of the osmolarity distribution on the entire exposed eye for the first time; to our knowledge, neither experimental nor theoretical studies have information about the osmolarity distribution on the entire exposed eye prior to our study.

In Chapter 6, we showed in detail the numerical methods we used and developed a hybrid time-stepping methods specifically for the discretized tear film-osmolarity coupled system. This hybrid time-stepping method is a fractional-step (splitting) method [64] that applies an implicit BDF method and an explicit RKC method alternatively. It is suitable for a system that is weakly coupled by stiff and mildly stiff equations, like

the tear film model we derived in Chapter 3. In this chapter, we have also investigated some numerical properties of our method by solving a preliminary test problem on a disk, as well as on the the eye-shaped domain. Solutions to the test problem provide numerical evidence that confirms the accuracy of our methods. This method is worth further study. We plan to conduct a more thorough numerical analysis for this hybrid method in the future.

7.1 Future Work

To conduct *in vivo* experiment, eye doctors often instill a solution with a certain concentration of fluorescein into the subject's eyes for the purpose of visualization. We would like to model the dynamics of fluorescein concentration by incorporating it as another solute into our tear film and osmolarity dynamics model. We have some preliminary results that predict the fluorescent intensity profile comparable to *in vivo* experiments for the interior of the eye. However, in order to capture the fluorescent intensity dynamics in the meniscus of the tear film, we need to improve the boundary condition imposed for the fluorescein concentration, and some other unrealistic model assumptions. For example, the volume of tear fluid is probably large in our current model compared to DES subjects, and could affect the dynamics of fluorescein concentration, especially in the meniscus.

There are some limitations to the current study for linking the osmolarity measured *in vivo* with the computed results. In our model, there is no lid motion to mix the tear fluid as occurs *in vivo*. This may be a significant component to the variability observed. The ultimate goal of our efforts is to model and simulate tear film dynamics (including osmolarity and surfactant) on a blinking eye-shaped domain for complete blinking cycles. To achieve this goal, we need to model the movement of the upper eye lid and generate adaptive composite overlapping grids for an eye-shaped domain with moving boundary. Moreover, we need to develop appropriate numerical methods that would be able to accurately resolve even steeper menisci that occur when the eye is not fully open.

BIBLIOGRAPHY

[1] V. S. Ajaev. Evolution of dry patches in evaporating liquid films. *Phys. Rev. E*, 72:031605, 2005.

[2] V. S. Ajaev. Spreading of thin volatile liquid droplets on uniformly heated surfaces. *J. Fluid Mech.*, 528:279–296, 2005.

[3] V. S. Ajaev and G.M. Homsy. Steady vapor bubbles in rectangular microchannels. *J. Colloid Interface Sci.*, 240:259–271, 2001.

[4] J. Aliò and M. Padron. Influence of age on the temperature of the anterior segment of the eye. *Ophthalmic Res.*, 14:153–159, 1982.

[5] F. Amparo, P. Hamrah, D. A. Schaumberg, and R. Dana. The value of tear osmolarity as a metric in evaluating the response to dry eye therapy in the clinic and in clinical trials. *Am. J. Ophthalmol.*, 157:915–916, 2014.

[6] F. Amparo, Y. Jin, P. Hamrah, D. A. Schaumberg, and R. Dana. What is the value of incorporating tear osmolarity measurement in assessing patient response to therapy in dry eye disease? *Am. J. Ophthalmol.*, 157:69–77.e2, 2013.

[7] Anonymous. Report of the International Dry Eye WorkShop (DEWS). *Ocul. Surf.*, 5:65–204, 2007.

[8] C. Baudouin, P. Aragona, E. M. Messmer, A. Tomlinson, M. Calonge, K. G. Boboridis, Y. A. Akova, G. Geerling, M. Labetoulle, and M. Rolando. Role of hyperosmolarity in the pathogenesis and management of dry eye disease: Proceedings of the ocean group meeting. *Ocul. Surf.*, 11:246–258, 2013.

[9] U. Benelli, M. Nardi, C. Posarelli, and T. G. Albert. Tear osmolarity measurement using the TearLab^{TM} osmolarity system in the assessment of dry eye treatment effectiveness. *Contact Lens Anterior Eye*, 33:61–67, 2010.

[10] R. E. Berger and S. Corrsin. A surface tension gradient mechanism for driving the pre-corneal tear film after a blink. *J. Biomech.*, 7:225–228, 1974.

[11] R. J. Braun. Dynamics of the tear film. *Annu. Rev. Fluid Mech.*, 44:267–297, 2012.

[12] R. J. Braun and A. D. Fitt. Modeling the drainage of the precorneal tear film after a blink. *Math. Med. Biol.*, 20:1–28, 2003.

[13] R. J. Braun, N. Gewecke, C. G. Begley, P. E. King-Smith, and J. I. Siddique. A model for tear film thinning with osmolarity and fluorescein. *Invest. Ophthalmol. Vis. Sci.*, 55:1133–1142, 2014.

[14] R. J. Braun and P. E. King-Smith. Model problems for the tear film in a blink cycle: Single equation models. *J. Fluid Mech.*, 586:465–490, 2007.

[15] R. J. Braun, P. E. King-Smith, J. J. Nichols, and P. Ramamoorthy. On computational models for tear film and osmolarity dynamics. *6th International Conference on the Tear Film and Ocular Surface: Basic Science and Clinical Relevance*, Poster 46:(abstract), 2010.

[16] R. J. Braun, R. Usha, G. B. McFadden, T. A. Driscoll, L. P. Cook, and P. E. King-Smith. Thin film dynamics on a prolate spheroid with application to the cornea. *J. Eng. Math.*, 73:121–138, 2012.

[17] K. E. Brenan, S. L. Campbell, and L. R. Petzold. *Numerical Solution of Initial-Value Problems in Differential-Algebraic Equations*. SIAM, Philadelphia, 1996.

[18] A.J. Bron, J.M. Tiffany, S.M. Gouveia, N. Yokoi, and L.W. Voon. Functional aspects of the tear film lipid layer. *Exp. Eye Res.*, 78:347–360, 2004.

[19] J. L. Bruhns, R. J. Braun, R. M. Evans, D. B. Freeman, P. E. King-Smith, P. Ramamoorthy, and J. J. Nichols. Models for interaction of the tear film with the corneal and conjunctival epithelia. *(in preparation)*, 2014.

[20] M. Bruna and C. J. W. Breward. The influence of nonpolar lipids on tear film dynamics. *J. Fluid Mech.*, 746:565–605, 2014.

[21] C. R. Canning, M. J. Greaney, J. N. Dewynne, and A. D. Fitt. Fluid flow in the anterior chamber of the eye. *IMA J. Math. Appl. Med. Biol.*, 19:31–60, 2002.

[22] C. Canuto, Y. F. Hussaini, A. Quarteroni, and T. A. Zang. *Spectral Methods in Fluid Dynamics*. Springer, Berlin, 1991.

[23] G. Chesshire and W. D. Henshaw. Composite overlapping meshes for the solution of partial differential equations. *J. Comput. Phys.*, 90:1–64, 1990.

[24] J. P. Craig, I. Singh, A. Tomlinson, P. B. Morgan, and N. Efron. The role of tear physiology in ocular surface temperature. *Eye*, 14:635–641, 2000.

[25] D. A. Dartt. Regulation of mucin and fluid secretion by conjunctival epithelial cells. *Prog. Ret. Eyt Res.*, 21:555–576, 2002.

[26] Q. Deng, R. J. Braun, and T. A. Driscoll. Heat transfer and tear film dynamics over multiple blink cycles. *Phys. Fluids*, 26:071901, 2014.

[27] Q. Deng, T. A. Driscoll, R. J. Braun, and P. E. King-Smith. A model for the tear film and ocular surface temperature for partial blinks. *Interfacial Phen. Ht. Trans.*, 1:357–381, 2013.

[28] M. G. Doane. Blinking and the mechanics of the lacrimal drainage system. *Ophthalmology*, 88:844–851, 1981.

[29] M.G. Doane. An instrument for in vivo tear film interferometry. *Optom. Vis. Sci.*, 66:383–388, 1989.

[30] N. Efron, G. Young, and N. A. Brennan. Ocular surface temperature. *Curr. Eye. Res.*, 8:901–906, 1989.

[31] I. Fatt and J. F. Forester. Errors in eye tissue measurements when using a metallic probe. *Exp. Eye Res.*, 14:270–276, 1972.

[32] I. Fatt and B. Weissman. *Physiology of the Eye: An Introduction to the Vegetative Functions*. Butterworth-Heineman, Boston, 2nd edition, 1992.

[33] A. D. Fitt and G. Gonzalez. Fluid mechanics of the human eye: Aqueous humour flow in the anterior chamber. *Bull. Math. Biol.*, 68:53–71, 2006.

[34] H. Fujishima, I. Toda, M. Yamada, N. Sato, and K. Tsubota. Corneal temperature in patients with dry eye evaluated by infrared radiation thermometry. *Br. J. Ophthalmol.*, 80:29–32, 1996.

[35] J. P. Gilbard, R. L. Farris, and J. 2nd. Santamaria. Osmolarity of tear microvolumes in keratoconjunctivitis sicca. *Arch. Ophthalmol.*, 96:677–681, 1978.

[36] I. K. Gipson. Distribution of mucins at the ocular surface. *Exp. Eye Res.*, 78:379–388, 2004.

[37] T. R. Golding, A. S. Bruce, and J. C. Mainstone. Relationship between tear-meniscus parameters and tear-film breakup. *Cornea*, 16:649–661, 1997.

[38] B. Govindarajan and I.K. Gipson. Membrane-tethered mucins have multiple functions on the ocular surface. *Exp. Eye Res.*, 90:655–693, 2010.

[39] K. Gustafsson, M. Lundh, and G. Söderlind. A pi stepsize control for the numerical solution of ordinary differential equations. *BIT*, 28:270–287, 1988.

[40] E. Hairer and G. Wanner. *Solving Ordinary Differential Equations II Stiff and Differential-Algebraic Problems*. Springer-Verlag, 2nd edition, 1996.

[41] W. W. Harrison, C. G. Begley, H. Liu, M. Chen, M. Garcia, and J. A. Smith. Menisci and fullness of the blink in dry eye. *Optom. Vis. Sci.*, 85:706–714, 2008.

[42] W. D. Henshaw. Ogen: the overture overlapping grid generator. Technical Report UCRL-MA-132237, Lawrence Livermore National Laboratory, 2002.

[43] A. Heryudono, R. J. Braun, T. A. Driscoll, L. P. Cook, K. L. Maki, and P. E. King-Smith. Single-equation models for the tear film in a blink cycle: Realistic lid motion. *Math. Med. Biol.*, 24:347–377, 2007.

[44] J. J. Heys and V. H. Barocas. A boussinesq model of natural convection in the human eye and the formation of krukenberg's spindle. *Ann. Biomed. Eng.*, 30:392–401, 2002.

[45] F. J. Holly and M. A. Lemp. Tear physiology and dry eyes. *Rev. Surv. Ophthalmol.*, 22:69–87, 1977.

[46] F.J. Holly. Formation and rupture of the tear film. *Exp. Eye Res.*, 15:515–525, 1973.

[47] M. E. Johnson and P. J. Murphy. Changes in the tear film and ocular surface from dry eye syndrome. *Prog. Ret. Eye Res.*, 23:449–474, 2004.

[48] M. B. Jones, D. L. S. McElwain, G. R. Fulford, M. J. Collins, and A. P. Roberts. The effect of the lipid layer on tear film behavior. *Bull. Math. Biol.*, 68:1355–1381, 2006.

[49] M. B. Jones, C. P. Please, D. L. S. McElwain, G. R. Fulford, A. P. Roberts, and M. J. Collins. Dynamics of tear film deposition and drainage. *Math. Med. Bio.*, 22:265–288, 2005.

[50] T. Kamao, M. Yamaguchi, S. Kawasaki, S. Mizoue, A. Shiraishi, and Y. Ohashi. Screening for dry eye with newly developed ocular surface thermographer. *Am. J. Ophthalmol.*, 151:782–791.e1, 2011.

[51] A. Karampatzakis and T. Samaras. Numerical model of heat transfer in the human eye with consideration of fluid dynamics of the aqueous humour. *Phys. Med. Biol.*, 55:5653–5665, 2010.

[52] S. H. Kimball, P. E. King-Smith, and J. J. Nichols. Evidence for the major contribution of evaporation to tear film thinning between blinks. *Invest. Opthalmol. Vis. Sci.*, 51:6294–6297, 2010.

[53] P. E. King-Smith, B. A. Fink, R. M. Hill, K. W. Koelling, and J. M. Tiffany. The thickness of the tear film. *Curr. Eye. Res.*, 29:357–368, 2004.

[54] P. E. King-Smith, B. A. Fink, J. J. Nichols, K. K. Nichols, R. J. Braun, and G. B. McFadden. The contribution of lipid layer movement to tear film thinning and breakup. *Invest. Ophthalmol. Visual Sci.*, 50:2747–2756, 2009.

[55] P. E. King-Smith, J. J. Nichols, K. K. Nichols, and R. J. Braun. A high resolution microscope for imaging the lipid layer of the tear film. *Ocular Surf.*, 9(4):197–211, 2011.

[56] P. E. King-Smith, J. J. Nichols, K. K. Nichols, B. A. Fink, and R. J. Braun. Contributions of evaporation and other mechanisms to tear film thinning and breakup. *Optom. Vis. Sci.*, 85:623–630, 2008.

[57] P. E. King-Smith, J. J. Nichols, K. K. Nichols, B. A. Fink, K. B. Green-Church, and R. J. Braun. Does the water permeability of the corneal surface help prevent excessive evaporative thinning of the tear film? In *5th International Conference on the Tear Film and Ocular Surface: Basic Science and Clinical Relevance*, Taormina, Italy, 2007.

[58] P. E. King-Smith, P. Ramamoorthy, R. J. Braun, and J. J. Nichols. Tear film images and breakup analyzed using fluorescent quenching. *Invest. Ophthalmol. Vis. Sci.*, 54:6003–6011, 2013.

[59] P. E. King-Smith, P. Ramamoorthy, K. K. Nichols, R. J. Braun, and J. J. Nichols. If tear evaporation is so high, why is tear osmolarity so low? *6th International Conference on the Tear Film and Ocular Surface: Basic Science and Clinical Relevance*, Poster 43:(abstract), 2010.

[60] P.E. King-Smith, B.A. Fink, N. Fogt, K. K. Nichols, R.M. Hill, and G. S. Wilson. The thickness of the human precorneal tear film: Evidence from reflection spectra. *Invest. Ophthalmol. Vis. Sci.*, 41:3348–3359, 2000.

[61] J. R. Lakowicz. *Principal of Fluorescence Spectroscopy*. Springer, New York, 3rd edition, 2006.

[62] M. A. Lemp. The definition and classification of dry eye disease: report of the definition and classification subcommittee of the international dry eye workshop. *Ocul. Surf.*, 5:75–92, 2007.

[63] M. A. Lemp, A. J. Bron, C. Baudoin, J. M. Benitez Del Castillo, D. Geffen, G. N. Foulks J. Tauber, J. S. Pepose, and B. D. Sullivan. Tear osmolarity in the diagnosis and management of dry eye disease. *Am. J. Ophthalmol.*, 151:792–798, 2011.

[64] Randall J. LeVeque. *Finite Volume Methods for Hyperbolic Problems*. Cambridge University Press, 2002.

[65] M. H. Levin and A. S. Verkman. Aquaporin-dependent water permeation at the mouse ocular surface: In vivo microfluorometric measurements in cornea and conjunctiva. *Invest. Ophthalmol. Vis. Sci.*, 45:4423–4432, 2004.

[66] L. Li and R. J. Braun. A model for the human tear film with heating from within the eye. *Phys. Fluids*, 24:062103, 2012.

[67] L. Li, R. J. Braun, K. L. Maki, W. D. Henshaw, and P. E. King-Smith. Tear film dynamics with evaporation, wetting and time-dependent flux boundary condition on an eye-shaped domain. *Phys. Fluids*, 26:052101, 2014.

[68] D. T. Liu, M. A. Di Pascuale, J. Sawai, Y. Y. Gao, and S. C. Tseng. Tear film dynamics in floppy eyelid syndrome. *Invest. Ophthalmol. Visual Sci.*, 46:1188–1194, 2005.

[69] H. Liu, C. Begley, M. Chen, A. Bradley, J. Bonanno, N. A. McNamara, J. D. Nelson, and T. Simpson. A link between tear instability and hyperosmolarity in dry eye. *Invest. Ophthalmol. Vis. Sci.*, 50:3671–3679, 2009.

[70] K. L. Maki. *Computational solutions of linear systems and models of the human tear film.* PhD thesis, University of Delaware, 2009.

[71] K. L. Maki, R. J. Braun, T. A. Driscoll, and P. E. King-Smith. An overset grid method for the study of reflex tearing. *Math. Med. Biol.*, 25:187–214, 2008.

[72] K. L. Maki, R. J. Braun, W. D. Henshaw, and P. E. King-Smith. Tear film dynamics on an eye-shaped domain I: pressure boundary conditions. *Math. Med. Biol.*, 27:227–254, 2010.

[73] K. L. Maki, R. J. Braun, P. Ucciferro, W. D. Henshaw, and P. E. King-Smith. Tear film dynamics on an eye-shaped domain. Part 2. Flux boundary conditions. *J. Fluid Mech.*, 647:361–390, 2010.

[74] R. Mapstone. Determinants of corneal temperature. *Br. J. Ophthalmol.*, 52:729–741, 1968.

[75] R. Mapstone. Measurement of corneal temperature. *Exp. Eye Res.*, 7:237–242, 1968.

[76] R. Mapstone. Normal thermal patterns in cornea and periorbital skin. *Br. J. Ophthalmol.*, 52:818–827, 1968.

[77] W. D. Mathers. Ocular evaporation in meibomian gland dysfunction and dry eye. *Ophthalmology*, 100:347–351, 1993.

[78] W. D. Mathers. Evaporation from the ocular surface. *Exp. Eye Res.*, 78:389–394, 2004.

[79] W. D. Mathers, G. Binarao, and M. Petroll. Ocular water evaporation and the dry eye: A new measuring device. *Cornea*, 12:335–340, 1993.

[80] W.D. Mathers and T.E. Daley. Tear flow and evaporation in patients with and without dry eye. *Ophthalmol.*, 103:664–669, 1996.

[81] D. M. Maurice. The dynamics and drainage of tears. *Int. Ophthalmol. Clin.*, 13:103–116, 1973.

[82] J. E. McDonald and S. Brubaker. Meniscus-induced thinning of tear films. *Am. J. Ophthalmol.*, 72:139–146, 1971.

[83] K. L. Miller, K. A. Polse, and C. J. Radke. Black line formation and the "perched" human tear film. *Curr. Eye Res.*, 25:155–162, 2002.

[84] S. Mishima, A. Gasset, S. D. Klyce, and J. L. Baum. Determination of tear volume and tear flow. *Ophthalmol. Vis. Sci.*, 5:264–276, 1966.

[85] S. Mishima, Z. Kubota, and R. L. Farris. The tear flow dynamics in normal and in keratoconjunctivitis sicca cases. In M. P. Solanes, editor, *Proceedings of the XXI International Congress, Mexico, DF, 8-14 March, 1970*, volume Part 2, pages 1801–1805, 1971.

[86] S. Mishima and D.M. Maurice. The oily layer of the tear film and evaporation from the corneal surface. *Exp. Eye Res.*, 1:39–45, 1961.

[87] A. Mori, Y. Oguchi, Y. Okusawa, M. Onon, H. Fujishima, and K. Tsubota. Use of high-speed, high-resolution thermography to evaluate the tear film layer. *Am. J. Ophthalmol.*, 124:729–735, 1997.

[88] B. Nagyová and J. M. Tiffany. Components of tears responsible for surface tension. *Curr. Eye Res.*, 19:4–11, 1999.

[89] E. Y. K. Ng and E. H. Ooi. FEM simulation of the eye structure with bioheat analysis. *Comput. Methods Programs Biomed.*, 82:268–276, 2006.

[90] E. Y. K. Ng and E. H. Ooi. Ocular surface temperature: A 3D FEM prediction using bioheat equation. *Comput. Biol. Med.*, 37:829–835, 2007.

[91] J. J. Nichols, P. E. King-Smith, E. A. Hinel, M. Thangavelu, and K. K. Nichols. The use of fluorescent quenching in studying the contribution of evaporation to tear thinning. *Invest. Ophthalmol. Visual Sci.*, 53:5426–5432, 2012.

[92] J. J. Nichols, G. L. Mitchell, and P. E. King-Smith. Thinning rate of the precorneal and prelens tear films. *Invest. Ophthalmol. Visual Sci.*, 46:2353–2361, 2005.

[93] M. S. Norn. Semiquantitative interference study of the fatty layer of precorneal film. *Acta Ophthalmol.*, 57:766–774, 1979.

[94] E. H. Ooi and E. Y. K. Ng. Simulation of aqueous humor hydrodynamics in human eye heat transfer. *Comp. Biol. Med.*, 38:252–262, 2008.

[95] H. Owens and J. Phillips. Spreading of the tears after a blink: Velocity and stabilization time in healthy eyes. *Cornea*, 20:484–487, 2001.

[96] C.-C. Peng, C. Cerretani, R. J. Braun, and C. J. Radke. Evaporation-driven instability of the precorneal tear film. *Adv. Coll. Interface Sci.*, 206:250–264, 2014.

[97] J S. Pepose, B. D. Sullivan, G. N. Foulks, and M. A. Lemp. The value of tear osmolarity as a metric in evaluating the response to dry eye therapy in the clinic and in clinical trials. *Am. J. Ophthalmol.*, 157:4–6.e1, 2014.

[98] C. Purslow and J. S. Wolffsohn. Ocular surface temperature: A review. *Eye Contact Lens*, 31:117–123, 2005.

[99] C. Purslow, J. S. Wolffsohn, and J. Santodomingo-Rubido. The effect of contact lens wear on dynamic ocular surface temperature. *Contact Lens Anterior Eye*, 28:29–36, 2005.

[100] M. Rolando and M. F. Refojo. Tear evaporimeter for measuring water evaporation rate from the tear film under controlled conditions in humans. *Exp. Eye Res.*, 36:25–33, 1983.

[101] R. F. Rosenbluth and I. Fatt. Temperature measurements in the eye. *Exp. Eye Res.*, 25:325–341, 1977.

[102] J. A. Scott. The computation of temperature rises in the human eye induced by infrared radiation. *Phys. Med. Biol.*, 33:243–257, 1988.

[103] J. A. Scott. A finite element model of heat transport in the human eye. *Phys. Med. Biol.*, 33:227–241, 1988.

[104] A. Sharma, S. Tiwari, R. Khanna, and J. M. Tiffany. Hydrodynamics of meniscus-induced thinning of the tear film. In D. A. Sullivan, D. A. Dartt, and M. A. Meneray, editors, *Advances in Experimental Medicine and Biology*, volume 438 of *Lacrimal Gland, Tear Film, and Dry Eye Syndromes 2*, pages 425–431, Berlin, 1998. Springer.

[105] J. H. Siggers and C. R. Ethier. Fluid mechanics of the eye. *Annu. Rev. Fluid Mech.*, 44:347–372, 2012.

[106] C. Sodtke, V. S. Ajaev, and P. Stephan. Dynamics of volatile liquid droplets on heated surfaces: Theory versus experiment. *J. Fluid Mech.*, 610:343–362, 2008.

[107] B. P. Sommeijer, L. F. Shampine, and J. G. Verwer. RKC: An explicit solver for parabolic pdes. *J. Comput. Appl. Math.*, 88:315–326, 1997.

[108] B. D. Sullivan. Challenges in using signs and symptoms to evaluate new biomarkers of dry eye disease. *Ocul. Surf.*, 12:2–9, 2014.

[109] B. D. Sullivan, D. Whitmer, K. K. Nichols, A. Tomlinson, G. N. Foulks, G. Geerling, J. S. Pepose, V. Kosheleff, A. Porreco, and M. A. Lemp. An objective approach to dry eye disease severity. *Invest. Ophthalmol. Vis. Sci.*, 51:6125–6130, 2010.

[110] TearLab. website. *http://www.tearlab.com*, 2013.

[111] N. W. Tietz. *Clinical Guide to Laboratory Tests*. W. B. Saunders, 3rd edition, 1995.

[112] J. M. Tiffany. The viscosity of human tears. *Int. Ophthalmol.*, 15:371–376, 1991.

[113] A. Tomlinson, M. G. Doane, and A. McFadyen. Inputs and outputs of the lacrimal system: review of production and evaporative loss. *Ocul. Surf.*, 7:186–198, 2009.

[114] A. Tomlinson, S. Khanal, K. Ramesh, and et al. Tear film osmolarity as a referent for dry eye diagnosis. *Invest. Ophthalmol. Vis. Sci.*, 47:4309–4315, 2006.

[115] L. N. Trefethen. *Spectral Methods in MATLAB*. SIAM, Philadelphia, 2000.

[116] P. J. van der Houwen and B. P. Sommeijer. On the internal stability of explicit, m-stage runge-kutta methods for large m-values. *Z. Angew. Math. Mech.*, 60:479–485, 1980.

[117] P. Versura, V. Profazio, and E. C. Campos. Performance of tear osmolarity compared to previous diagnostic tests for dry eye diseases. *Curr. Eye Res.*, 35:553–564, 2010.

[118] J. G. Verwer. Explicit runge-kutta methods for parabolic partial differential equations. *Appl. Numer. Math.*, 22:359–379, 1996.

[119] J. G. Verwer, W. H. Hundsdorfer, and B. P. Sommeijer. Convergence properties of the runge-kutta-chebyshev method. *Numer. Math.*, 57:157–178, 1990.

[120] J. G. Verwer, B. P. Sommeijer, and W. Hundsdorfer. RKC time-stepping for advection–diffusion–reaction problems. *J. Comput. Phys.*, 201:61–79, 2004.

[121] J. Wang, D. Fonn, T. L. Simpson, and L. Jones. Precorneal and pre- and postlens tear film thickness measured indirectly with optical coherence tomography. *Invest. Ophthalmol. Vis. Sci.*, 44:2524–2528, 2003.

[122] H. A. Watts. Step size control in ordinary differential equation solvers. *Trans. Soc. Comput. Simulation*, 1:15–25, 1984.

[123] W. R. S. Webber and D. P. Jones. Continuous fluorophotometric method measuring tear turnover rate in humans and analysis of factors affecting accuracy. *Med. Biol. Eng. Comput.*, 24:386–392, 1986.

[124] K. N. Winter, D. M. Anderson, and R. J. Braun. A model for wetting and evaporation of a post-blink precorneal tear film. *Math. Med. Biol.*, 27:211–225, 2010.

[125] H. Wong, I. Fatt, and C. J. Radke. Deposition and thinning of the human tear film. *J. Colloid Interface Sci.*, 184:44–51, 1996.

[126] H. Zhu and A. Chauhan. A mathematical model for tear drainage through the canaliculi. *Curr. Eye. Res.*, 30:621–630, 2005.

[127] V. S. Zubkov, C. J. Breward, and E. A. Gaffney. Coupling fluid and solute dynamics within the ocular surface tear film: a modelling study of black line osmolarity. *Bull. Math. Biol.*, 74:2062–2093, 2012.

Appendix A

PARAMETERS

In the table, we use specific heat of lens instead of water for $\kappa_c = k_c/(\rho c_p)$. K and $\bar{K}$ are chosen to satisfy the experimentally measured thinning rate (4 μm/min [92]) of the tear film thickness due to King-Smith *et al.* α and A^* are recovered from the nondimensional parameters in Winter *et al*[124]. Ajaev and Homsy[3] discuss α and K.

Parameter	Expression	Value
ϵ	$\dfrac{d'}{L'}$	1×10^{-3}
E	$\dfrac{k(T'_B - T'_s)}{d'\mathcal{L}_m \epsilon \rho U_0}$	118.3
S	$\dfrac{\sigma \epsilon^3}{\mu U_0}$	6.92×10^{-6}
$\bar{K}$	$\dfrac{kK}{d'\mathcal{L}_m}$	8.9×10^{3}
G	$\dfrac{\rho g (d')^2}{\mu U_0}$	0.05
δ	$\dfrac{\alpha \mu U_0}{\epsilon^2 L'(T'_B - T'_s)}$	4.66
A	$\dfrac{A^*}{L' d \mu U_0}$	2.14×10^{-6}
Pe_c	$\dfrac{U_0 L'}{D_c}$	9.62×10^{3}
P_{corn}	$\dfrac{P^{\mathrm{tiss}}_{\mathrm{corn}} v_w c_0}{\epsilon U_0}$	0.013
P_{conj}	$\dfrac{P^{\mathrm{tiss}}_{\mathrm{conj}} v_w c_0}{\epsilon U_0}$	0.06

Table A.1: Dimensionless Parameters. Values and descriptions of the dimensional parameters appeared are given in Table A.2.

Parameter	Description	Value	Reference
μ	Viscosity	1.3×10^{-3}Pa·s	[112]
σ	Surface tension	0.045N·m^{-1}	[88]
k	Tear film thermal conductivity	0.68W·m^{-1}·K^{-1}	Water
ρ	Density	10^3kg·m^{-3}	Water
$\mathcal{L}_m$	Latent heat of vaporization	2.3×10^6J·kg^{-1}	Water
T'_s	Saturation temperature	27°C	Estimated
T'_B	Body temperature	37°C	Estimated
g	Gravitational acceleration	9.81m·s^{-2}	Estimated
A^*	Hamaker constant	3.5×10^{-19}Pa·m^3	[124]
α	Pressure coefficient for evaporation	3.6×10^{-2}K·Pa^{-1}	[124]
K	Non-equilibrium coefficient	1.5×10^5K·m^2·s·kg^{-1}	Estimated
d'	Characteristic thickness	5×10^{-6}m	[53]
L'	Half-width of palpebral fissure	5×10^{-3}m	Estimated
U_0	Characteristic speed	5×10^{-3}m/s	[54]
$P^{\text{tiss}}_{\text{corn}}$	Tissue permeability of cornea	12.0μm/s	[59]
$P^{\text{tiss}}_{\text{conj}}$	Tissue permeability of conjunctiva	55.4μm/s	[59]
v_w	Molar volume of water	1.8×10^{-5}m^3·mol^{-1}	Water
D_c	Diffusivity of osmolarity in water	2.6×10^{-9}m^2/s	[127]

Table A.2: Dimensional Parameters.

Appendix B

COPYRIGHT PERMISSIONS

AIP PUBLISHING LLC LICENSE TERMS AND CONDITIONS

Aug 08, 2014

All payments must be made in full to CCC. For payment instructions, please see information listed at the bottom of this form.

License Number	3443951020939
Order Date	Aug 07, 2014
Publisher	AIP Publishing LLC
Publication	Physics of Fluids
Article Title	A model for the human tear film with heating from within the eye
Author	Longfei Li,R. J. Braun
Online Publication Date	Jun 19, 2012
Volume number	24
Issue number	6
Type of Use	Thesis/Dissertation
Requestor type	Author (original article)
Format	Print and electronic
Portion	Excerpt (> 800 words)
Will you be translating?	No
Title of your thesis / dissertation	MATHEMATICAL MODELS AND NUMERICAL METHODS FOR HUMAN TEAR FILM DYNAMICS
Expected completion date	Aug 2014
Estimated size (number of pages)	120
Total	**0.00 USD**

Terms and Conditions

AIP Publishing LLC -- Terms and Conditions: Permissions Uses

AIP Publishing LLC ("AIPP"") hereby grants to you the non-exclusive right and license to use and/or distribute the Material according to the use specified in your order, on a one-time basis, for the specified term, with a maximum distribution equal to the number that you have ordered. Any links or other content accompanying the Material are not the subject of this license.

1. You agree to include the following copyright and permission notice with the reproduction of the Material:"Reprinted with permission from [FULL CITATION]. Copyright [PUBLICATION YEAR], AIP Publishing LLC." For an article, the copyright and permission notice must be printed on the first page of the article or book chapter. For photographs, covers, or tables, the copyright and permission notice may appear with the Material, in a footnote, or in the reference list.
2. If you have licensed reuse of a figure, photograph, cover, or table, it is your responsibility to ensure that the material is original to AIPP and does not contain the copyright of another entity, and that the copyright notice of the figure, photograph, cover, or table does not indicate that it was reprinted by AIPP, with permission, from another source. Under no circumstances does AIPP, purport or intend to grant permission to reuse material to which it does not hold copyright.
3. You may not alter or modify the Material in any manner. You may translate the Material into another language only if you have licensed translation rights. You may not use the Material for promotional purposes. AIPP reserves all rights not specifically granted herein.
4. The foregoing license shall not take effect unless and until AIPP or its agent, Copyright Clearance Center, receives the Payment in accordance with Copyright Clearance Center Billing and Payment Terms and Conditions, which are incorporated herein by reference.

5. AIPP or the Copyright Clearance Center may, within two business days of granting this license, revoke the license for any reason whatsoever, with a full refund payable to you. Should you violate the terms of this license at any time, AIPP, AIP Publishing LLC, or Copyright Clearance Center may revoke the license with no refund to you. Notice of such revocation will be made using the contact information provided by you. Failure to receive such notice will not nullify the revocation.
6. AIPP makes no representations or warranties with respect to the Material. You agree to indemnify and hold harmless AIPP, AIP Publishing LLC, and their officers, directors, employees or agents from and against any and all claims arising out of your use of the Material other than as specifically authorized herein.
7. The permission granted herein is personal to you and is not transferable or assignable without the prior written permission of AIPP. This license may not be amended except in a writing signed by the party to be charged.
8. If purchase orders, acknowledgments or check endorsements are issued on any forms containing terms and conditions which are inconsistent with these provisions, such inconsistent terms and conditions shall be of no force and effect. This document, including the CCC Billing and Payment Terms and Conditions, shall be the entire agreement between the parties relating to the subject matter hereof.

This Agreement shall be governed by and construed in accordance with the laws of the State of New York. Both parties hereby submit to the jurisdiction of the courts of New York County for purposes of resolving any disputes that may arise hereunder.

If you would like to pay for this license now, please remit this license along with your payment made payable to "COPYRIGHT CLEARANCE CENTER" otherwise you will be invoiced within 48 hours of the license date. Payment should be in the form of a check or money order referencing your account number and this invoice number RLNK501372426. Once you receive your invoice for this order, you may pay your invoice by credit card. Please follow instructions provided at that time.

Make Payment To:
Copyright Clearance Center
Dept 001
P.O. Box 843006
Boston, MA 02284-3006

For suggestions or comments regarding this order, contact RightsLink Customer Support: customercare@copyright.com or +1-877-622-5543 (toll free in the US) or +1-978-646-2777.

Gratis licenses (referencing $0 in the Total field) are free. Please retain this printable license for your reference. No payment is required.

AIP PUBLISHING LLC LICENSE TERMS AND CONDITIONS

Aug 08, 2014

All payments must be made in full to CCC. For payment instructions, please see information listed at the bottom of this form.

License Number	3444500675935
Order Date	Aug 08, 2014
Publisher	AIP Publishing LLC
Publication	Physics of Fluids
Article Title	Tear film dynamics with evaporation, wetting, and time-dependent flux boundary condition on an eye-shaped domain
Author	Longfei Li,R. J. Braun,K. L. Maki, et al.
Online Publication Date	May 6, 2014
Volume number	26
Issue number	5
Type of Use	Thesis/Dissertation
Requestor type	Author (original article)
Format	Print and electronic
Portion	Excerpt (> 800 words)
Will you be translating?	No
Title of your thesis / dissertation	MATHEMATICAL MODELS AND NUMERICAL METHODS FOR HUMAN TEAR FILM DYNAMICS
Expected completion date	Aug 2014
Estimated size (number of pages)	120
Total	**0.00 USD**

Terms and Conditions

AIP Publishing LLC -- Terms and Conditions: Permissions Uses

AIP Publishing LLC ("AIPP"") hereby grants to you the non-exclusive right and license to use and/or distribute the Material according to the use specified in your order, on a one-time basis, for the specified term, with a maximum distribution equal to the number that you have ordered. Any links or other content accompanying the Material are not the subject of this license.

1. You agree to include the following copyright and permission notice with the reproduction of the Material:"Reprinted with permission from [FULL CITATION]. Copyright [PUBLICATION YEAR], AIP Publishing LLC." For an article, the copyright and permission notice must be printed on the first page of the article or book chapter. For photographs, covers, or tables, the copyright and permission notice may appear with the Material, in a footnote, or in the reference list.
2. If you have licensed reuse of a figure, photograph, cover, or table, it is your responsibility to ensure that the material is original to AIPP and does not contain the copyright of another entity, and that the copyright notice of the figure, photograph, cover, or table does not indicate that it was reprinted by AIPP, with permission, from another source. Under no circumstances does AIPP, purport or intend to grant permission to reuse material to which it does not hold copyright.
3. You may not alter or modify the Material in any manner. You may translate the Material into another language only if you have licensed translation rights. You may not use the Material for promotional purposes. AIPP reserves all rights not specifically granted herein.
4. The foregoing license shall not take effect unless and until AIPP or its agent, Copyright Clearance Center, receives the Payment in accordance with Copyright Clearance Center Billing and Payment Terms and Conditions, which are

incorporated herein by reference.

5. AIPP or the Copyright Clearance Center may, within two business days of granting this license, revoke the license for any reason whatsoever, with a full refund payable to you. Should you violate the terms of this license at any time, AIPP, AIP Publishing LLC, or Copyright Clearance Center may revoke the license with no refund to you. Notice of such revocation will be made using the contact information provided by you. Failure to receive such notice will not nullify the revocation.
6. AIPP makes no representations or warranties with respect to the Material. You agree to indemnify and hold harmless AIPP, AIP Publishing LLC, and their officers, directors, employees or agents from and against any and all claims arising out of your use of the Material other than as specifically authorized herein.
7. The permission granted herein is personal to you and is not transferable or assignable without the prior written permission of AIPP. This license may not be amended except in a writing signed by the party to be charged.
8. If purchase orders, acknowledgments or check endorsements are issued on any forms containing terms and conditions which are inconsistent with these provisions, such inconsistent terms and conditions shall be of no force and effect. This document, including the CCC Billing and Payment Terms and Conditions, shall be the entire agreement between the parties relating to the subject matter hereof.

This Agreement shall be governed by and construed in accordance with the laws of the State of New York. Both parties hereby submit to the jurisdiction of the courts of New York County for purposes of resolving any disputes that may arise hereunder.

If you would like to pay for this license now, please remit this license along with your payment made payable to "COPYRIGHT CLEARANCE CENTER" otherwise you will be invoiced within 48 hours of the license date. Payment should be in the form of a check or money order referencing your account number and this invoice number RLNK501373335. Once you receive your invoice for this order, you may pay your invoice by credit card. Please follow instructions provided at that time.

Make Payment To:
Copyright Clearance Center
Dept 001
P.O. Box 843006
Boston, MA 02284-3006

For suggestions or comments regarding this order, contact RightsLink Customer Support: customercare@copyright.com or +1-877-622-5543 (toll free in the US) or +1-978-646-2777.

Gratis licenses (referencing $0 in the Total field) are free. Please retain this printable license for your reference. No payment is required.